X-ray Studies of Unidentified Very High Energy Gamma-ray Sources

Michito Sakai

Division of Particle and Astrophysical Science,
Graduate School of Science, Nagoya University

February 21, 2013

Abstract

The H.E.S.S. Cherenkov telescope has revealed the presence of about 100 very high energy (VHE; $E > 100$ GeV) γ-ray sources. Most of the objects are located on the Galactic plane and spatially extended, and therefore may be Galactic objects, such as pulsar wind nebulae (PWNe) and supernova remnants (SNRs). Surprisingly, many of them have no known counterpart in other wavelengths. They are referred to as "Unidentified VHE γ-ray Sources". VHE γ-ray emission shows the presence of high-energy particles. If these particles are high-energy protons, it may lead to the origin of cosmic-ray protons, which has been a mystery since its discovery. Therefore, it is important to clarify the nature of unidentified VHE γ-ray sources. Since the interstellar medium is almost transparent to X-ray photons above 2 keV throughout the Galaxy, it is effective to use X-ray wavelengths for identifying these unidentified VHE γ-ray sources.

In order to study the nature of unidentified VHE γ-ray sources, we mainly analyzed the two unidentified VHE γ-ray sources (HESS J1614−518 and HESS J1646−458). HESS J1614−518 is one of the brightest VHE γ-ray sources. We observed the whole region of HESS J1614−518 with Suzaku. As a result, we revealed that the source is bright in the VHE γ-ray band, but very dim in the X-ray band. The high value of $f_{\rm TeV}/f_{\rm X} \sim 34$ may suggest a proton accelerator. We also detected the soft X-ray source, XMMU J161406.0−515225, at the middle of HESS J1614−518. This source might be an anomalous X-ray pulsar (AXP) and may be physically related to HESS J1614−518. If that so, HESS J1614−518 may be an SNR associated with an AXP. On the other hand, HESS J1646−458 is a degree-scale extended VHE γ-ray source and contains the pulsar PSR J1648−4611. We observed this pulsar with Suzaku and discovered the diffuse hard X-ray emission, Suzaku J1648−4610, around the pulsar. The spatial distribution and the photon index of the diffuse emission suggest a PWN. However, the luminosity of the diffuse emission is much larger than that expected from the spin-down luminosity of the pulsar. Parts of the VHE γ-ray emission of HESS J1646−458 may be powered by this peculiar PWN driven by PSR J1648−4611.

Also, several other sources, we mainly investigated the presence or absence of the possible counterpart in the X-ray band. Although there are some X-ray sources in the fields of view, most of them do not show the obvious physical connection to VHE γ-ray emission. However, a few of the unidentified VHE γ-ray sources have possible X-ray counterparts and could be linked to a relatively old PWN still visible at VHE γ-rays.

Some of unidentified VHE γ-ray sources may be peculiar SNRs or PWNe like HESS J1614−518 and HESS J1646−458.

Contents

List of Figures

List of Tables

Chapter 1

Introduction

The H.E.S.S. Cherenkov telescope, a high-sensitivity TeV γ-ray telescope, has revealed the presence of many very high energy (VHE; $E > 100$ GeV) γ-ray objects along the Galactic plane (Aharonian et al., 2005a, 2006a). Most of the objects are spatially extended and therefore may be Galactic objects, such as pulsar wind nebulae (PWNe) (e.g., Renaud et al., 2008b) and supernova remnants (SNRs) (e.g., Aharonian et al., 2008a). Surprisingly, many of them have no clear counterpart at other wavelengths so that they are called "Unidentified VHE γ-ray Sources". VHE γ-ray emission shows the presence of high-energy particles. If these particles are high-energy protons, it may lead to the origin of cosmic-ray protons, which has been a mystery since its discovery. Therefore, it is important to clarify the nature of unidentified VHE γ-ray sources.

Since the interstellar medium is almost transparent to X-ray photons above 2 keV throughout the Galaxy, it is effective to use X-ray wavelengths for identifying these unidentified VHE γ-ray sources. On the other hand, if the VHE γ rays result from inverse Compton (IC) upscattering of seed photons (cosmic microwave background or other low-energy photons) by highly energized electrons, they should also radiate X-rays in the synchrotron process. In fact, synchrotron X-rays are detected from many of the identified VHE γ-ray sources. These detections help to identify the sources. Additionally, if we find X-ray counterparts of unidentified VHE γ-ray sources, we are able to estimate a distance to the object from an X-ray absorption column density. Thus, X-ray observations are important and useful tools for identifying unidentified VHE γ-ray sources, and a lot of follow-up observations are going on using various X-ray satellites such as Suzaku, XMM-Newton and Chandra. As a result, several unidentified VHE γ-ray sources have been identified such as PWNe and SNRs (e.g., Uchiyama et al., 2009a; Nakamura et al., 2009). However, the nature of a large number of unidentified VHE γ-ray sources ($\sim 30\%$ of the Galactic VHE γ-ray sources) is still unclear. Thus, it is important to have access to more X-ray data for understanding the nature of unidentified VHE γ-ray sources.

In this thesis, we make analysis of 10 unidentified VHE γ-ray sources in order to study the nature of unidentified VHE γ-ray sources. In Chapter 2, we review the properties of VHE γ-ray sources and the related phenomena in the universe with the underlying physics. We describe X-ray instruments used in this thesis in Chapter 3. The analyses and results of the X-ray observations of the unidentified VHE γ-ray sources with the discussion are

summarized in Chapter 4 and 5. Chapter 6 lists the conclusions of the current studies.

Chapter 2

Review

In this chapter, we summarize the properties of the VHE γ-ray sources, and the related phenomena in the universe together with the underlying physics. Because the VHE γ-ray emission is closely related to cosmic rays, we start our review with the brief description of them in §2.1. After this preliminary, we describe the recent progress of the VHE γ-ray observation in §2.2. Then, we describe their emission mechanisms in §2.3. Finally, we describe the unique sources of VHE γ rays in §2.4.

2.1 Cosmic Rays

Excluding neutrinos, cosmic rays mainly consist of charged particles, such as protons ($\sim 90\%$), helium nuclei ($< 10\%$), ionized heavier elements ($< 1\%$), and electrons ($< 1\%$), while only 0.1%–1% of the total radiation consists of photons with energy > 1 MeV.

The energy of cosmic rays covers more than 10 orders of magnitude, from tens of MeV up to 10^{20} eV and higher. The dependence of the flux on the energy E of the particle can be approximated by a power law

$$dN/dE \propto E^{-\alpha}, \tag{2.1}$$

where the spectral index α has typical values between 2.5 and 3. The energy dependence can be explained in first approximation due to shock acceleration mechanisms (Fermi, 1949).

Figure 2.1 shows the energy spectrum for cosmic rays (Cronin et al., 1997). The region around $10^{15.5}$ eV is referred as the "knee", for its spectral steepening (from a spectral index of about 2.7 to about 3), while the region around $10^{18.5}$ eV, where a spectral flattening occurs, is called the "ankle" of the spectrum. It is generally believed that cosmic rays below the knee have a galactic origin and that they have been confined inside our Galaxy for at least 10^7 years (this can be expected from the value of the magnetic field in the galaxy, which is of the order of 1 μG) (Zwiebel & Heiles, 1997). The particles above 10^{17} eV are believed to be mostly of extragalactic origin, since the Galactic magnetic field is not able to trap them in our Galaxy.

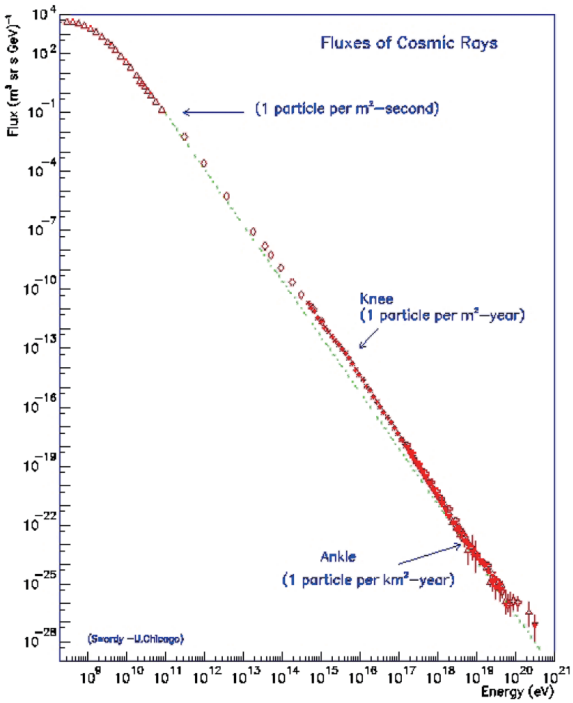

Figure 2.1: Energy spectrum of cosmic rays. (Cronin et al., 1997)

2.2 VHE γ-ray Sky

Thanks mostly to Cherenkov telescopes, a large amount of VHE γ-ray sources, which may operate as cosmic particle accelerators, has been detected (see figure 2.2). When this thesis has been written (December 2012), > 100 VHE γ-ray sources have been detected. Some of them are identified as pulsar wind nebulae (PWNe), supernova remnants (SNRs), binaries, and so on. However, a large number of the VHE γ-ray sources have no clear counterpart at other wavelengths. These sources are thus called "Unidentified VHE γ-ray Sources". Today, there are ~ 30 such unidentified VHE γ-ray sources on the Galactic plane.

Specifically, the recent dramatic growth (by a factor of ~ 10) in the number of known Galactic VHE γ-ray sources is largely a consequence of the survey of the Galactic plane conducted with the southern-located H.E.S.S. between 2004 and 2007 (Aharonian et al., 2006a). Figure 2.3 shows the extent of this scan, which covers essentially the whole inner Galaxy: $-85° < l < 60°$, $-2.5° < b < 2.5°$ (Hoppe et al., 2008).

Pulsar Wind Nebulae (PWN) The majority of the identified VHE γ-ray sources are PWN. In these objects a rapidly spinning neutron star produces a relativistic wind of electrons that produce X-ray synchrotron radiation. Inverse Compton (IC) upscattering

[1]See ⟨http://tevcat.uchicago.edu/⟩.

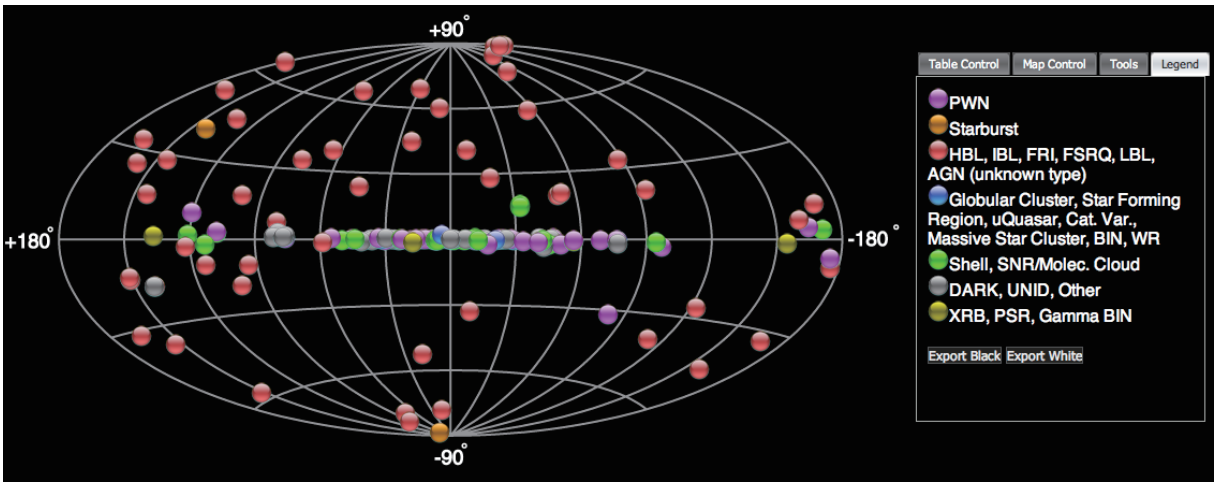

Figure 2.2: Known sources in the VHE γ-ray sky in 2012[1].

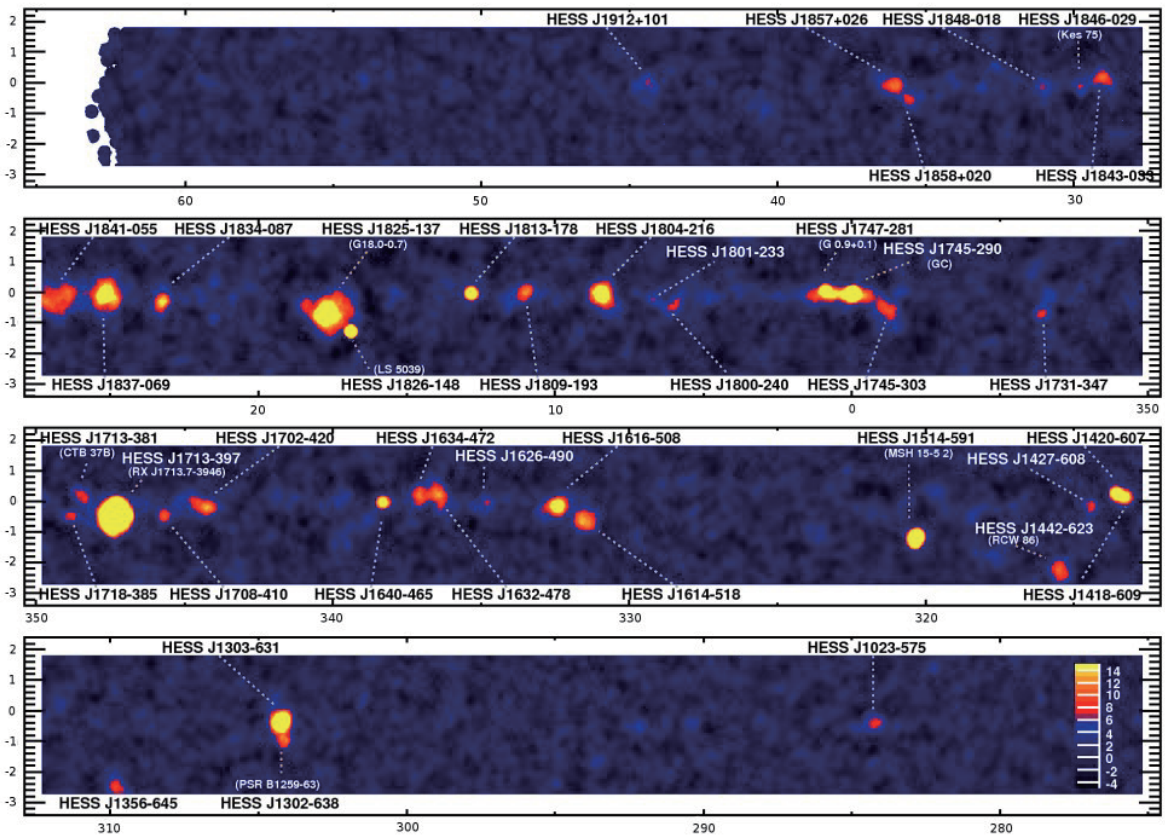

Figure 2.3: Known galactic VHE γ-ray sources from the survey of the galactic plane by the H.E.S.S. telescope between 2004 and 2007 (Hoppe et al., 2008).

of ambient photons, either cosmic microwave background (CMB) or from nearby stars, produces the observed VHE γ-ray emission. A good example of an extended VHE γ-ray PWN closely matching its X-ray emission is that of MSH 15−52 (Aharonian et al., 2005e). On the other hand, the PWN HESS J1825−137 has been the first VHE γ-ray source to display an energy-dependent morphology, in the sense of a softening of the spectrum with increasing distance from the pulsar. This favors a leptonic scenario where there is cooling of the electrons in the nebula. Interestingly, the data is not compatible with a constant spin-down power, and a higher injection power in the past is required (Aharonian et al., 2006b).

Supernova Remnants (SNR) SNR are thought to be the sites of cosmic-ray acceleration up to the knee, and TeV photons, which are not deflected by galactic magnetic fields, can provide valuable information in this respect. Good examples of SNRs displaying a shell at TeV energies are RX J1713.7−3946 and RX J0852−4622 (Aharonian et al., 2004, 2005f, respectively). Interestingly the TeV shells follow nicely the synchrotron keV emission seen by X-ray satellites. This suggests that a leptonic scenario could be at work, where relativistic electrons produce the synchrotron X-ray emission and IC up-scatter ambient photons to produce TeV emission. However, detailed TeV spectra appear to be more compatible with a hadronic origin, where VHE γ rays are produced by inelastic *pp* interactions and π^0 decay (Aharonian et al., 2006c, 2007b,c).

TeV emission has also been found in SNR near molecular clouds such as HESS J1834−087/W41 (Aharonian et al., 2006a; Albert et al., 2006a) and MAGIC J0616+225/IC 443 (Albert et al., 2007a). More precisely the TeV emission appears to originate, specially in the second case, in the interaction between the SNR and the molecular cloud, clearly suggesting a hadronic scenario.

Binaries In both PWNe and SNRs particle acceleration proceeds on the parsec distance scales in the shocks formed in interactions of either the ejecta of pulsar winds or supernovae with the interstellar medium. A different population of much more compact particle accelerators is formed by the TeV binaries. These systems contain a compact object — either a neutron star or a black hole — that accretes, or interacts with, matter outflowing from a companion star: hence they are VHE-loud X-ray binaries. Four TeV binaries have been detected so far: PSR B1259−63 (Aharonian et al., 2005b), LS 5039 (Aharonian et al., 2005g, 2006d), LSI +61 303 (Albert et al., 2006b), and Cyg X−1 (Albert et al., 2007b).

2.3 Radiation from Accelerated Particles

There are two possible mechanisms to radiate VHE γ rays efficiently: (1) electronic origin and (2) hadronic origin of γ rays. In the former, VHE γ rays result from inverse Compton (IC) upscattering of seed photons (cosmic microwave background or other low-energy photons) by highly energized electrons. These electrons radiate X-rays in the synchrotron

process. In the latter, VHE γ rays are explained by the decay of neutral pions that originate in collisions between high-energy protons and dense interstellar matter.

Here we overview these emission process from synchrotron radiation.

2.3.1 Synchrotron Radiation

Particles accelerate by a magnetic field B will radiate. This radiation is known as synchrotron radiation.

The power per unit frequency emitted by each electron (mass m and charge q) is

$$P(\omega) = \frac{\sqrt{3}}{2\pi}\frac{q^3 B \sin\alpha}{mc^2} F\left(\frac{\omega}{\omega_c}\right), \tag{2.2}$$

and

$$\omega_c = \frac{3\gamma^2 qB\sin\alpha}{2mc}, \tag{2.3}$$

where $\gamma^{-1} = \sqrt{1-(v/c)^2}$, α is the pitch angle between field and velocity, and $F(x)$ is a dimensionless function given by equation (6.31c) of Rybicki & Lightman (2004) from which has a peak at $x \sim 0.29$.

Integrating the power per unit frequency described in equation (2.2) over ω, we can obtain the total power as

$$P = \frac{4}{3}\sigma_T c\beta^2\gamma^2 U_B. \tag{2.4}$$

Here $\sigma_T = 8\pi r_0^2/3$ is the Thomson cross section, r_0 is the classical electron radius, and U_B is the magnetic energy density, $U_B = B^2/8\pi$.

An analogous result sometimes holds for the particle distribution law of relativistic electrons. Often the number density of particles with energies between E and $E + dE$ (or $\gamma + d\gamma$) can be approximately expressed in the form

$$N(E)dE = CE^{-p}dE, E_1 < E < E_2, \tag{2.5}$$

or

$$N(\gamma)d\gamma = C\gamma^{-p}d\gamma, \gamma_1 < \gamma < \gamma_2. \tag{2.6}$$

The total power radiated per unit volume per unit frequency by such a distribution is given by the integral of $N(\gamma)d\gamma$ times the single particle radiation formula over all energies or γ. Thus, we have

$$P_{\rm tot}(\omega) = C\int_{\gamma_1}^{\gamma_2} P(\omega)\gamma^{-p}d\gamma \propto \int_{\gamma_1}^{\gamma_2} F\left(\frac{\omega}{\omega_c}\right)\gamma^{-p}d\gamma. \tag{2.7}$$

Let us change variables of integration to $x \equiv \omega/\omega_c$, noting $\omega_c \propto \gamma^2$;

$$P_{\rm tot}(\omega) \propto \omega^{-(p-1)/2} \int_{x_1}^{x_2} F(x) x^{(p-3)/2} dx. \tag{2.8}$$

The limits x_1 and x_2 correspond to the limits γ_1 and γ_2 and depend on ω. However, if the energy limits are sufficiently wide, the integral is approximately constant. In that case, we have

$$P_{\rm tot}(\omega) \propto \omega^{-(p-1)/2}, \tag{2.9}$$

so that the spectral index s is related to the particle distribution index p by

$$s = \frac{p-1}{2}. \tag{2.10}$$

Above X-ray energies, the emission is often described as a power-law distribution of photons, such that $N_E \propto E^{-\Gamma}$, where N_E is the number of photons emitted between energies E and $E + dE$, and $\Gamma \equiv 1 + s = (1+p)/2$ is the photon index. When $p \sim 2$, Γ becomes ~ 1.5.

2.3.2 Inverse Compton Scattering

Now we want to derive average formulas for the case of a given isotropic distribution of photons scattering off a given isotropic distribution of electrons.

The power per unit frequency emitted by each electron is

$$P = \frac{4}{3} \sigma_T c \beta^2 \gamma^2 U_{\rm ph}, \tag{2.11}$$

where $U_{\rm ph}$ is the initial photon energy density. Using equation (2.4), we have the general result:

$$\frac{P_{\rm synch}}{P_{\rm compt}} = \frac{U_B}{U_{\rm ph}}, \tag{2.12}$$

that is, the radiation losses due to synchrotron emission and to inverse Compton effect are in the same ratio as the magnetic field energy density and photon energy density. Note that this result is valid only for the Thomson regime ($\gamma\epsilon_0 \ll m_e c^2$). In the constant $U_{\rm ph}$ case, such as the upscattered photons being cosmic microwave background (CMB), we can determine the strength of magnetic field directly comparing $P_{\rm synch}$ and $P_{\rm compt}$.

Suppose that the isotropic incident photon field is monoenergetic:

$$I(\epsilon) = F_0 \delta(\epsilon - \epsilon_0), \tag{2.13}$$

where F_0 is the number of photons per unit area, per unit time per steradian. For values of β near unity ($\gamma \gg 1$) it is convenient to rescale the energy variable and write

$$x \equiv \frac{\epsilon_1}{4\gamma^2 \epsilon_0}, \tag{2.14}$$

where ϵ_1 is the photon energy after scattering, and the emission function, in our isotropic approximation, can be written as

$$j(\epsilon_1) = \frac{3N\sigma_T F_0}{4\gamma^2\epsilon_0} f_{\rm iso}(x), \tag{2.15}$$

where

$$f_{\rm iso}(x) \equiv \frac{2}{3}(1-x), 0 < x < 1, \tag{2.16}$$

and zero otherwise.

Let us use $v(\epsilon)$, the initial photon number density, related to the isotropic intensity by $v(\epsilon) = 4\pi c^{-1} I(\epsilon)$. Then the total scattered power per volume per energy is

$$\frac{dE}{dV dt d\epsilon_1} = 4\pi\epsilon_1 j(\epsilon_1) = 3\sigma_T c C 2^{p-2}\epsilon_1^{-(p-1)/2} \int d\epsilon \epsilon^{(p-1)/2} v(\epsilon) \int_{x_1}^{x_2} dx x^{(p-1)/2} f(x), \tag{2.17}$$

where $x_1 \equiv \epsilon_1/(4\gamma_1^2\epsilon)$ and $x_2 \equiv \epsilon_1/(4\gamma_2^2\epsilon)$. Integrating over all ϵ_1, we obtain the spectral index s,

$$s = \frac{p-1}{2}, \tag{2.18}$$

which is identical to the case of synchrotron emission (cf. equation (2.10)).

The general problem of scattering of an isotropic photon field from an isotropic electron distribution, including the Compton effect and Klein-Nishina cross section, has been solved by Jones (1968).

2.3.3 π^0-Decay Emission

As mentioned in §2.1, the main component of cosmic rays is proton. Accelerated high energy protons produce π^0 mesons when they collide with other protons in interstellar matter such as molecular clouds. γ rays are emitted by decay of these π^0 mesons. The decay is summarized as

$$p + p \longrightarrow p + p + \pi^0 \longrightarrow p + p + \gamma + \gamma. \tag{2.19}$$

To produce π^0 mesons, the kinetic energy of protons should exceed $E_{kin} = 2m_\pi c^2(1 + m_\pi/4m_p) \sim 280$ MeV. The π^0 mesons decay to two γ rays with the mean lifetime of $t_{\pi^0} = 8.4 \times 10^{-17}$ s, which is significantly shorter than the lifetime of charged π mesons.

The emissivity of π^0 decay γ rays for an arbitrary spectrum is calculated as (Aharonian & Atoyan, 1996)

$$q_\gamma(E_\gamma) = 2\int_{E_{\rm min}}^{\infty} \frac{q_\pi(E_\pi)}{\sqrt{(E_\pi^2 - m_\pi^2 c^4)}} dE_\pi, \tag{2.20}$$

where

$$q_\pi(E_\pi) = \frac{cn_{\rm H}}{\kappa_\pi} \cdot \sigma_{pp}\left(m_p c^2 + \frac{E_\pi}{\kappa_\pi}\right) \cdot N_p\left(m_p c^2 + \frac{E_\pi}{\kappa_\pi}\right), \tag{2.21}$$

where $E_{\rm min} = E_\gamma + m_\pi^2 c^4/4E_\gamma$, $n_{\rm H}$ is the number density of hydrogen, $\sigma_{pp}(E_p)$ is the total cross section of inelastic pp collisions, κ_π is the mean fraction of the kinetic energy of the protons transferred to π^0 mesons per collision, and $N_p(E_p)$ is the energy distribution of the protons. The cross section $\sigma_{pp}(E_p)$ can be approximated by

$$\sigma_{pp}(E_p) \approx 30[0.95 + 0.06\ln((E_p - m_p c^2)/1\ {\rm GeV})]\ {\rm mb}. \tag{2.22}$$

The cooling timescale of protons due to this process is

$$t_{pp} = \frac{1}{n_{\rm H}\sigma_{pp} f_C}, \tag{2.23}$$

where f is the coefficient of inelasticity. Since $\sigma_{pp}(E_p)$ shows small energy dependency above 1 GeV (see equation (2.22)), t_{pp} is almost constant at $\simeq 5.3 \times 10^7 (n_{\rm H}/1\,{\rm cm}^{-3})^{-1}$ yr in the high energy region. Therefore, the initial spectrum of accelerated protons remains unchanged.

We note that the secondary electron, which is produced by the decay of π^- mesons, also emit synchrotron radiation, non-thermal bremsstrahlung, or inverse Compton scattering. The decay is summarized as

$$p + n \longrightarrow p + p + \pi^- \longrightarrow p + p + \mu^- + \overline{\nu}_\mu \longrightarrow p + p + e^- + \overline{\nu}_e + \nu_\mu. \tag{2.24}$$

2.3.4 Energy Scales and Lifetimes of Electrons

Here we estimate the energy scales and lifetimes of the X-ray synchrotron and VHE γ-ray IC emitting electrons.

Electron Energy Scale

The characteristic energy of synchrotron photons is $\epsilon_{\rm syn} \simeq \hbar\omega_c/3$, where ω_c is a frequency defined in equation (2.3). In the case of the isotropical pitch angle ψ, the photon energy is

$$\epsilon_{\rm syn} \simeq 0.2\left(\frac{B}{10\ \mu{\rm G}}\right)\left(\frac{E_e}{1\ {\rm TeV}}\right)^2\ {\rm eV}. \tag{2.25}$$

For IC scattering in the Thomson limit, the characteristic energy of IC photons is $\epsilon \simeq (4/3)h\nu_0(E_e/m_e c^2)^2$, where $h\nu_0$ is the energy of the target photons. Thus

$$\epsilon_{\rm IC} \simeq 5\left(\frac{h\nu_0}{10^{-3}\ {\rm eV}}\right)\left(\frac{E_e}{1\ {\rm TeV}}\right)^2\ {\rm GeV}. \tag{2.26}$$

Solving equation (2.25) and (2.26) for the energy of the electron, we obtain

$$E_e^{\rm syn} = 70 \times \left(\frac{B}{10\ \mu{\rm G}}\right)^{-\frac{1}{2}} \left(\frac{\epsilon_{\rm syn}}{1\ {\rm keV}}\right)^{\frac{1}{2}}\ {\rm TeV}, \tag{2.27}$$

$$E_e^{\rm IC} = 0.5 \times \left(\frac{h\nu_0}{1\ {\rm eV}}\right)^{-\frac{1}{2}} \left(\frac{\epsilon_{\rm IC}}{1\ {\rm TeV}}\right)^{\frac{1}{2}}\ {\rm TeV} \tag{2.28}$$

$$\simeq 20 \times \left(\frac{\epsilon_{\rm IC}}{1\ {\rm TeV}}\right)^{\frac{1}{2}}\ {\rm TeV}. \tag{2.29}$$

For the cosmic microwave background radiation (CMBR) seed photons, the mean energy of the target photons is $h\bar{\nu_0} = kT \sim 6 \times 10^{-4}$ eV, thus the production of the IC γ-ray photon with $\epsilon_{\rm IC} \sim 1$ TeV required the electron energy of $E_e^{\rm IC} \sim 20$ TeV, while is typically lower than that required energy of $E_e^{\rm syn} \sim 70$ TeV to produce the synchrotron photon of $\epsilon_{\rm syn} \sim 1$ keV.

Electron Lifetime

If we define the lifetime of electrons in a magnetic field B and a photon energy density $U_{\rm ph}$ to be $\tau = E_e/P$, it can be shown from equation (2.4) and (2.11) that the lifetime of electrons is

$$\tau(E_e) \simeq \left(\frac{4}{3}\sigma_T c U_0 E_e/m_e^2 c^4\right)^{-1} \tag{2.30}$$

$$= 3.1 \times 10^5 \times \left(\frac{E_e}{1\ {\rm TeV}}\right)^{-1} \left(\frac{U_0}{1\ {\rm eVcm^{-3}}}\right)^{-1} {\rm yr}, \tag{2.31}$$

where $U_0 = U_B + U_{\rm ph}$ and the magnetic energy density $U_B = B^2/8\pi$. If we assume the target photon as CMBR, the photon energy density is $U_{\rm ph} \sim 0.25$ eVcm^{-3}. In the case of low magnetic fields comparable with the interstellar medium magnetic filed, $B_{\rm ISM} \sim 3\ \mu$G, the magnetic energy density is $U_B \sim 0.25$ eVcm^{-3}. Thus, $U_0 \sim 0.5$ eVcm^{-3} equally contribute to the total energy losses for both synchrotron and IC processes. Typically, the lifetimes $\tau \sim 5$ kyr for the electrons with the energy of $E_e^{\rm sync} \sim 130$ TeV, and $\tau \sim 30$ kyr for the electrons with the energy of $E_e^{\rm IC} \sim 20$ TeV are obtained. On the other hand, in the case of magnetic fields comparable with the typical magnetic field of PWNe, $B_{\rm PWN} \sim 10\ \mu$G, the magnetic energy density is $U_B \sim 2.5$ eVcm^{-3}. Thus, $U_0 \sim 2.8$ eVcm^{-3} equally contribute to the total energy losses for both synchrotron and IC processes. Typically, the lifetimes $\tau \sim 2$ kyr for the electrons with the energy of $E_e^{\rm sync} \sim 70$ TeV, and $\tau \sim 6$ kyr for the electrons with the energy of $E_e^{\rm IC} \sim 20$ TeV are obtained.

2.3.5 Interstellar Photoelectric Absorption

At photon energies well below $m_e c^2$, the dominant process by which photons lose their energy is photoelectric absorption. As a matter of fact, the spectra of most astrophysical

X-ray sources display the signature of photoelectric absorption at energies below $\simeq 1$ keV. This cause mainly by photoelectric absorption of photons by heavy elements such as C, N, O, Ne, Mg, and Fe, and the interstellar absorption is usually described by the equivalent hydrogen column density ($N_{\rm H}$ cm^{-2}) assuming solar abundances (Morrison & McCammon, 1983).

Here the typical total density of the interstellar medium is $< n_{\rm H} > \sim 1$ atoms cm^{-3}, then the column density in midplane of our Galaxy can be written as

$$N_{\rm H} \approx 3 \times 10^{21}\ {\rm cm}^{-2} \left(\frac{< n_{\rm H} >}{1\ {\rm cm}^{-3}}\right) \left(\frac{D}{1\ {\rm kpc}}\right), \tag{2.32}$$

where D is a distance to the source in unit of kpc.

On the other hand, the $N_{\rm H}$ value can be derived from the HI map by Dickey & Lockman (1990). If we compared the $N_{\rm H}$ obtained from the X-ray spectral fit, we are able to estimate a distance to the source.

2.4 VHE γ-ray Sources

Here we review the VHE γ-ray sources. Since pulsar wind nebulae (PWNe) are the majority of Galactic VHE γ-ray sources, we start our review with the properties of pulsars and PWNe.

2.4.1 Pulsars and Pulsar Wind Nebulae

Neutron stars are formed through the supernova explosion of a massive star (≥ 8 M$_\odot$). They are highly compact (radius of ~ 10 km), yet having a mass comparable to the Sun (mass of ~ 1.4 M$_\odot$). Pulsars are highly magnetized, rapidly rotating neutron stars, which emit beams of radiation in the energy range from radio to γ ray. Because the emission can be observed only when the beam points to us, the signals detected are pulsed, which is responsible for the name of "pulsar". Since the discovery of the first pulsar, the number of known pulsars has now grown to more than 1500.

A neutron star rotating in the strong magnetic field induces large electric field. Accelerated by the electric field, charged particles move close to the speed of light. They move along the curved magnetic field lines, and emit γ rays through curvature radiation. These γ rays interact with surrounding magnetic field or photons and produce electron-positron pairs. The produced electron-positron pairs are accelerated, move along the magnetic field, and emit γ rays. Thus electron-positron pairs are produced in sequence and flow out as a very high energy plasma. This flow is called a "pulsar wind".

The rapid spin of the pulsar steadily slows down converting its rotational energy into the kinetic energy of the pulsar winds. The pulsar winds collide with their surrounding medium to form a shock, called a termination shock where particles are accelerated. At the shock, particles are thermalized and reaccelerated, producing synchrotron emission in the magnetic field and inverse Compton radiation in the ambient radiation field.

Here the rotational kinetic energy of the pulsar is

$$E_{\rm rot} = \frac{1}{2}I\omega^2 = \frac{1}{2}I\left(\frac{2\pi}{P}\right)^2, \tag{2.33}$$

where I is the neutron star's moment of inertia and is usually assumed to have the value 10^{45} g cm^2, $\omega = 2\pi/P$, and P is a spin period, so that the spin down luminosity of the pulsar, $\dot{E} = -dE_{\rm rot}/dt$, is the rate of the rotational kinetic energy loss:

$$\dot{E} = -I\omega\dot{\omega} = 4\pi^2 I\dot{P}P^{-3}, \tag{2.34}$$

where $\dot{P}$ is a period derivative with respect to time, $\dot{P} \equiv dP/dt$. Values of $\dot{E}$ for the observed pulsar population range between $\approx 5\times10^{38}$ erg s^{-1} for the Crab pulsar, down to 3×10^{28} erg s^{-1} for the slowest known pulsar, PSR J2144−3933 (Manchester et al., 2005). Relatively young and energetic pulsars with $\dot{E} \geq 4\times10^{33}$ erg s^{-1} produce prominent PWNe (Kargaltsev et al., 2009).

If a pulsar spins down from an initial spin period P_0 such that $\dot{\Omega} = -k\Omega^n$ (where $\Omega = 2\pi/P$ and n is the "braking index"), then the age of the system is (Manchester & Taylor, 1977):

$$\tau = \frac{P}{(n-1)\dot{P}}\left[1-\left(\frac{P_0}{P}\right)^{n-1}\right], \tag{2.35}$$

where we have assumed k to be a constant and $n \neq 1$. If for the rest of the population we assume $n = 3$, which correspond to spin down via magnetic dipole radiation, and $P_0 \ll P$, equation (2.35) reduces to the expression for the "characteristic age" of a pulsar,

$$\tau_c \equiv \frac{P}{2\dot{P}}. \tag{2.36}$$

One of the criteria considering the association of a VHE γ-ray source with the PWN of a known pulsar is the apparent efficiency for VHE γ-ray emission, relative to the pulsar's spin down luminosity $\dot{E}$. The apparent efficiency ϵ_γ is then defined as $\epsilon_\gamma = L_\gamma/\dot{E}$. Hessels et al. (2008) show that the efficiencies of VHE γ-ray sources possibly associated with PWNe range from $\sim 0.01 - 5\%$.

In addition, some other kinds of neutron stars, such as the Central Compact Objects (CCOs) in supernova remnants and the Anomalous X-ray Pulsars (AXPs), may be associated with VHE γ-ray sources (e.g., Halpern & Gotthelf, 2010)

2.4.2 Supernova Remnants

Supernova remnants (SNRs) are the most plausible candidates of the particle accelerators. An SNR is the structure produced by the shocks of the supernova explosion. Its explosion energy is typically 10^{53} ergs. Roughly 99% of this energy is radiated away by neutrinos, while about 1% of which is converted into the kinetic energy. The stellar ejecta carrying of order 10^{51} ergs of kinetic energy interact with surrounding circumstellar or interstellar medium. Initial speed of the ejecta reaches up to 10^{3-4} km s^{-1}, which form strong shock

waves, gradually decelerating over tens of thousands of years. The acceleration of ~ 100 TeV electrons in SNRs was first suggested by the discovery of synchrotron X-ray emission from shock fronts of an SNR SN 1006 (Koyama et al., 1995). In its shock front, electrons are accelerated by the first-order Fermi acceleration (Bell, 1978), sometimes referred to as the diffusive shock acceleration (DSA). RX J1713.7−3946 is the first SNR detected in VHE γ ray, whose shell was resolved in γ rays (Aharonian et al., 2004).

Here most of the shell-like SNRs have thermal X-ray, from a plasma heated by a shock wave. Some shell-like SNRs emit non-thermal synchrotron emission from radio to X-ray from shock-accelerated electrons.

One of the key objects considering the association of a VHE γ-ray source with the SNR is molecular clouds. A molecular cloud (MC) is low temperature (~ 10 K) and high density ($n[\mathrm{H}_2] \leq 10^2 - 10^3$ cm^{-3}) interstellar cloud. Hence, MC is good target for cosmic-ray protons to emit VHE γ ray by decay of π^0 mesons, as discussed in §2.3.3.

2.4.3 Other identified VHE γ-ray sources

Other identified VHE γ-ray sources include such as X-ray binaries and massive star clusters. In the case of X-ray binaries, VHE photons are believed to be produced by leptonic and hadronic interactions of high-energy charged particles accelerated in the shocks generated by the collision of a pulsar wind with the wind of the massive star or, alternatively, in shocks associated with an accretion-powered jet. On the other hand, in the case of massive star clusters, strong shocks created through the colliding winds of massive stars are believed to be able to accelerate particles up to TeV energies and their collective effects can in principle provide sufficient energy for the observed emission. However, the number of those with established multi-wavelength counterparts is still small.

Chapter 3

Instruments

In this study, we use observational data obtained with three X-ray satellites; Suzaku, XMM-Newton and Chandra. Illustrations of these satellites are shown in figure 3.1. In the following sections, we introduce the equipped instruments and their properties.

Figure 3.1: Illustrations of the Suzaku (top-left), XMM-Newton (top-right) and Chandra (bottom) spacecrafts.

3.1 Suzaku

The X-ray observatory Suzaku (Mitsuda et al., 2007), the fifth in a series of Japanese X-ray astronomy satellites, was launched on 2005 July 10. The orbit apogee is 568 km and the orbital period is 96 minutes. The scientific payload of Suzaku initially consisted of three distinct co-aligned scientific instruments. There are four X-ray sensitive imaging CCD cameras (X-ray Imaging Spectrometer, XIS, Koyama et al., 2007), three front-illuminated (FI: energy range 0.4–12 keV) and one back-illuminated (BI: energy range 0.2–12 keV), capable of moderate energy resolution. Each XIS is located in the focal plane of a dedicated X-Ray telescope (XRT, Serlemitsos et al., 2007). The second instrument is a non-imaging, collimated Hard X-ray Detector (HXD, Takahashi et al., 2007), which extends the bandpass of the observatory to much higher energies with its 10–600 keV bandpass (Kokubun et al., 2007). The last instrument, X-Ray Spectrometer (XRS), is no longer operational and will not be discussed further.

Table 3.1: Overview of Suzaku capabilities.

XRT	Focal length	4.75 m
	Field of View	$17'$ at 1.5 keV
		$13'$ at 8 keV
	Plate scale	0.724 arcmin/mm
	Effective Area	440 cm^2 at 1.5 keV
		250 cm^2 at 8 keV
	Angular Resolution	$2'$ (Half Power-Diameter)
XIS	Field of View	$17'.8 \times 17'.8$
	Bandpass	0.2–12 keV
	Pixel grid	1024×1024
	Pixel size	24 μm $\times$ 24 μm
	Energy Resolution	$\sim$ 130 eV at 6 keV (FWHM)
	Effective Area	330 cm^2 (FI), 370 cm^2 (BI) at 1.5 keV
	(incl XRT-I)	160 cm^2 (FI), 110 cm^2 (BI) at 8 keV
	Time Resolution	8 s (Normal mode), 7.8 ms (P-Sum mode)
HXD	Field of View	$4^\circ.5 \times 4^\circ.5$ ($\geq$ 100 keV)
	Field of View	$34' \times 34'$ ($\leq$ 100 keV)
	Bandpass	10–600 keV
	–PIN	10–70 keV
	–GSO	40–600 keV
	Energy Resolution (PIN)	$\sim$ 3.0 keV (FWHM)
	Energy Resolution (GSO)	$7.6/\sqrt{E_{\rm MeV}}\%$ (FWHM)
	Effective area	$\sim$ 160 cm^2 at 20 keV, $\sim$ 260 cm^2 at 100 keV
	Time Resolution	61 μs

3.1.1 X-Ray Telescope (XRT)

Suzaku has five sets of the X-Ray Telescope (XRT). These are grazing-incidence reflective optics consisting of tightly nasted, thin-foil conical mirror shells. Because of the reflectors' small thickness, they permit high-density nesting, and thus provide a large aperture efficiency with a moderate imaging capability in the energy of 0.2–12 keV, all accomplished in telescope units under 20 kg each, including pre-collimators for the rejection of stray light. Four sets of XRT onboard Suzaku (XRT-I0 to XRT-I3) are used for the XIS.

The angular resolutions of the XRTs range from $1'.8$ to $2'.3$, expressed in terms of the half-power diameter, which is the diameter within which half of the focused X-ray in enclosed. The angular resolution does not significantly depend on the energy of the incident X-rays in the energy range of Suzaku, 0.2–12 keV. The effective areas are typically 440 cm^2 at 1.5 keV and 250 cm^2 at 8 keV per telescope. The focal lengths are 4.75 m for the XRT-Is. Individual XRT quadrants have their own focal lengths deviated from the design values by a few centimeters. The optical axes of the quadrants of each XRT are aligned within $2'$ from each other. The field of view for XRT-Is is about $17'$ at 1.5 keV and $13'$ at 8 keV (see also table 3.1).

3.1.2 X-ray Imaging Spectrometer (XIS)

The X-ray Imaging Spectrometer (XIS) employs X-ray sensitive silicon charge-coupled devices (CCD), which are operated in a photon-counting mode, similar to that used in the ASCA SIS (Burke et al., 1994; Yamashita et al., 1997), Chandra ACIS (Garmire et al., 1992; Bautz et al., 1998), and XMM-Newton EPIC (Strüder et al., 2001; Turner et al., 2001). In general, an X-ray CCD converts an incident X-ray photon into a charge cloud, with the magnitude of charge proportional to the energy of the absorbed X-ray. This charge is then shifted out onto the gate of an output transistor via an application of a time-varying electrical potential. This results in a voltage level (often referred to as "pulse height") proportional to the energy of the X-ray photon.

The four sets of Suzaku XIS are designated XIS 0, XIS 1, XIS 2, and XIS 3, each located in the focal plane of an X-ray Telescope; XRT-I0, XRT-I1, XRT-I2, and XRT-I3. Each CCD camera has a single CCD chip with an array of 1024×1024 picture elements ("pixel"), and covers an $17'.8 \times 17'.8$ region on the sky. Each pixel is 24 μm square, and the size of the CCD is 25 mm $\times$ 25 mm. Effective area is shown in figure 3.2. One set of the XIS, XIS 1, uses a back-illuminated CCD, while the other three use front-illuminated CCDs.

3.1.3 Hard X-ray Detector (HXD)

The Hard X-ray Detector (HXD) is a non-imaging, collimated hard X-ray scintillating instrument sensitive in the $\sim$ 10 keV to $\sim$ 600 keV band. Its main purpose is to extend the bandpass of the Suzaku observatory to the highest feasible energies, thus allowing broad-band studies of celestial objects.

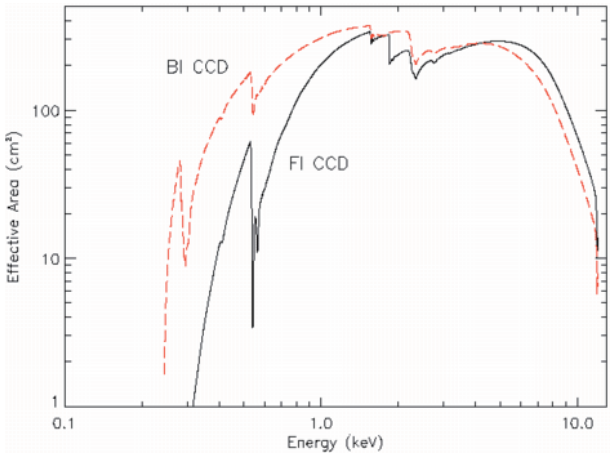

Figure 3.2: Effective area of on XRT+XIS system, for both the FI (XIS 0,2,3) and BI (XIS 1) CCDs.

The HXD sensor (HXD-S) is a compound-eye detector instrument, consisting of 16 main detectors (arranged as a 4×4 array) and the surrounding 20 crystal scintillators for active shielding. Each unit actually consists of two types of detectors: a GSO/BGO phoswich counter, and 2 mm-thick PIN silicon diodes located inside the well, but in front of the GSO scintillator. The PIN diodes are mainly sensitive below ~ 60 keV, while the GSO/BGO phoswich counter (scintillator) is sensitive above ~ 30 keV. The scintillator signals are read out by photomultiplier tubes. The HXD features an effective area of ~ 160 cm^2 at 20 keV, and ~ 260 cm^2 at 100 keV (see figure 3.3). The energy resolution is ~ 3.0 keV (FWHM) for the PIN diodes, and $7.6/\sqrt{E}\%$ (FWHM) for the scintillators, where E is energy in MeV. The HXD time resolution is 61 μs.

The outer anti-coincidence scintillators can be used as a wide-field hard X-ray detector, which is referred as the Wide-band All-sky Monitor (WAM). This can be used to detect bright X-ray transients, γ-ray bursts, and solar flares.

3.2 XMM-Newton

The XMM-Newton space observatory (Jansen et al., 2001) was launched on 1999 December 10. The orbit of the satellite is highly eccentric, with a ~ 48 hour period. The perigee is 7000 km and apogee of 114000 km. The 4 tonne, 10 m long XMM-Newton spacecraft is the largest scientific satellite ever to be launched by the European Space Agency. It comprises two large payload modules connected by a long carbon fiber tube which forms the telescope optical bench. On the Focal Plane Assembly are located the two Reflection Grating Spectrometer (Den Herder et al., 2001) readout cameras, an EPIC PN (Strüder et al., 2001) and two EPIC MOS imaging detectors (Turner et al., 2001). The spacecraft Service Module contains most of the spacecraft sub-systems, as well as the Optical Monitor instrument (Mason et al., 2001), star trackers and the three X-ray

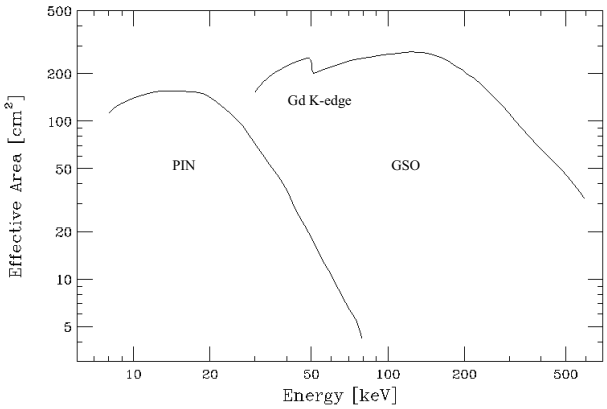

Figure 3.3: Total effective area of the HXD detectors, PIN and GSO, as a function of energy.

Mirror Modules.

3.2.1 X-ray Telescopes

Each of the three X-ray telescopes on board XMM-Newton consists of 58 Wolter I mirrors which are nested in a coaxial and confocal configuration (Aschenbach et al., 1987). This design provides a large collecting area over a wide energy band. The mirror grazing incidence angles range between 17 and 42 arcmin. Their focal length is 7.5 m and the diameter of the largest mirrors is 70 cm, to be compatible with the shroud of the launcher.

Mirrors were replicated from superpolished gold coated mandrels using a nickel electroforming technique (Gondoin et al., 1994). The 58 mirrors of each telescope are bonded on their entrance aperture to the 16 spokes of a single spider. An electron deflector is located in the exit aperture. It produces a circumferential magnetic field which prevents low energy electrons reflected by the mirrors reaching the focal plane detectors. X-ray baffles consisting of two sieve plates each with 58 annular apertures are located in front of the mirror systems. They act as collimators and considerably reduce the amount of straylight in the field of view of the focal plane cameras.

The point spread functions (PSFs) and effective areas of the telescopes were first characterized on-ground during an extensive calibration campaign (Gondoin et al., 1998a,b). A comprehensive numerical model of the mirror system (Gondoin et al., 1996) was then used to generate an initial calibration database by extrapolating on-ground tests to in-orbit operation conditions and by interpolating between the finite number of measurement points. During the in-orbit calibration program, appropriate celestial targets were observed to validate this initial database (Gondoin et al., 2000). Analysis results indicate that the telescopes ' point responses measured in-orbit are identical to on-ground calibration measurements. In particular, extended sources in the center of the telescope field of view can be studied with a ~ 5 arcsec spatial resolution. Fitting residuals of the spectra of astrophysical plasmas broadly confirm the on-ground calibration of the relative

effective area close to the Au M edges. No evidence for contamination is detected close to the C K and O K edges. Measurements of the in-orbit vignetting function match simulation results extrapolated from on-ground calibration. Pointings in the vicinity of the Crab nebula verify the high straylight rejection efficiency of the telescope baffles.

3.2.2 European Photon Imaging Camera (EPIC)

The XMM-Newton spacecraft is carrying a set of three X-ray CCD cameras, comprising the European Photon Imaging Camera (EPIC). Two of the cameras are MOS (Metal Oxide Semi-conductor) CCD arrays (Turner et al., 2001). They are installed behind the X-ray telescopes that are equipped with the gratings of the Reflection Grating Spectrometers (RGS). The gratings divert about half of the telescope incident flux towards the RGS detectors such that (taking structural obscuration into account) about 44% of the original incoming flux reaches the MOS cameras. The third X-ray telescope has an unobstructed beam; the EPIC instrument at the focus of this telescope uses pn CCDs and is referred to as the pn camera.

The EPIC cameras offer the possibility to perform extremely sensitive imaging observations over the telescope's field of view (FOV) of 30 arcmin and in the energy range from 0.15 to 15 keV with moderate spectral ($E/\Delta E \sim$ 20–50) and angular resolution (PSF, 6 arcsec FWHM). These and other important EPIC characteristics are listed in table 3.2.

All EPIC CCDs operate in photon counting mode with a fixed, mode dependent frame read-out frequency, producing event lists, i.e. tables with one entry line per received event, listing (among others) attributes of the events such as the position at which they were registered, their arrival time and their energies. The two types of EPIC, however, differ in some major aspects. This does not only hold for the geometry of the CCD arrays and the instrument design but also for other properties, like e.g., their readout times.

Another experiment on board of XMM-Newton is the EPIC Radiation Monitor (ERM). The main function of the ERM is the detection of the radiative belts and solar flares in order to supply particle environment information for the correct operation of the EPIC camera. In addition, the ERM provides detailed monitoring of the space radiative environment constituting a reference for the development of detectors to be used in futures missions.

Table 3.2: XMM-Newton EPIC Characteristics.

	EPIC MOS	EPIC pn
Focal length	7.5 m	
Field of View	$30'$	
Effective Area	1500 cm^2 at 1 keV	
PSF (FWHM/HEW)	$5''/14''$	$6''/15''$
Pixel size	40 μm ($1''.1$)	150 μm ($4''.1$)
Time Resolution	2.6 s (Full frame)	73.4 ms (Full frame)

3.3 Chandra

The Chandra X-Ray Observatory (Weisskopf et al., 2002) was launched on 1999 July 23. The orbit of the satellite is highly eccentric, with a ~ 64 hour period. The perigee is 10000 km and apogee of 140000 km. Chandra's X-ray subsystems are the High-Resolution Mirror Assembly (HRMA) and the focal-plane science instruments. For the focal-plane instrument, we can choose one of two kinds of X-ray detectors: the Advanced CCD Imaging Spectrometer (ACIS) and the High Resolution Camera (HRC). HRC is a multiple-channel plate type detector optimized for imaging and is without ability of spectroscopy. Since we used only ACIS in this thesis, HRMA and ACIS are described further below.

3.3.1 High-Resolution Mirror Assembly (HRMA)

The Chandra X-ray telescope consists of 4 pairs of concentric thin-walled, grazing-incidence Wolter Type-I mirrors called the High Resolution Mirror Assembly (HRMA). The front mirror of each pair is a paraboloid (Pn) and the back a hyperboloid (Hn). The eight mirrors were fabricated from Zerodur glass, polished, and coated with iridium on a binding layer of chromium.

The HRMA, shown schematically in figure 3.4, contains the nested mirrors, center, forward and aft aperture plates, baffles, inner and outer cylinders, mounts, pre- and post-collimators, fiducial light transfer components, mirror support sleeves, forward and aft contamination covers, flux contamination monitors, and thermal control hardware. The outer mirror pair is number 1, and, progressing inwards, 3, 4, and 6. The original design had six mirror pairs; numbers 2 and 5 were eliminated. The pair diameters range from about 0.65 to 1.23 m. The distance from the center of the Central Aperture Plate (CAP) separating the paraboloid and hyperboloid mirrors to the HRMA focus is 10.0548 m, with each mirror pair varying slightly about this value. Note that this distance is close to, but not exactly, the focal length. An annular on-axis beam enters each mirror pair, is reflected from paraboloids and hyperboloids and exits to converge to a focus. The angle θ between the direction of the reflected ray and the optical axis lies between two cone angles $\theta_{\rm c}$ and $\theta_{\rm d}$. These and other important HRMA characteristics are listed in table 3.3.

3.3.2 Advanced CCD Imaging Spectrometer (ACIS)

The Advanced CCD Imaging Spectrometer (ACIS) offers the capability to simultaneously acquire high-resolution images and moderate resolution spectra. The instrument can also be used in conjunction with the High Energy Transmission Grating (HETG) or Low Energy Transmission Grating (LETG) to obtain higher resolution spectra. ACIS contains 10 planar, 1024×1024 pixel CCDs (Figure 3.5); four arranged in a 2×2 array (ACIS-I) used for imaging, and six arranged in a 1×6 array (ACIS-S) used either for imaging or as a grating readout. Currently any combination of up to 6 CCDs may be operated simultaneously. Prior popular combinations include an extended ACIS-I imaging mode, using chips I0-I3 plus S2 and S3; and an ACIS-S imaging mode, using chips S1-S4 plus I2 and I3. Operating six chips enhances the chance of serendipitous science, but at

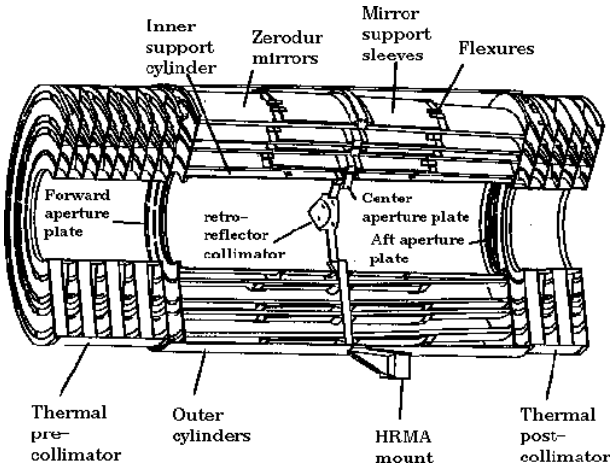

Figure 3.4: The four nested HRMA mirror pairs and associated structures.

Table 3.3: Chandra HRMA and ACIS Characteristics.

HRMA	Focal length	10.07 m
	Ghost-free Field of View	$30'$
	Plate scale	48.8 μm/arcsec
	Effective Area	800 cm^2 at 0.25 keV
		400 cm^2 at 5 keV
		100 cm^2 at 8 keV
	Angular Resolution	$< 0''.5$ (FWHM)
ACIS	Pixel grid	1024×1024
	Pixel size	24 μm ($0''.492$)
	Array size (ACIS-I)	$16'.9 \times 16'.9$
	Array size (ACIS-S)	$8'.3 \times 50'.6$
	Effective Area	110 cm^2 (FI) at 0.5 keV
		600 cm^2 (FI) at 1.5 keV
		40 cm^2 (FI) at 8.0 keV
	Time Resolution	3.2 s (full frame)

the price of increased total background counting rate and therefore a somewhat enhanced probability of saturating telemetry. Another penalty for 6 operating CCDs is an increased power load. Two CCDs are back-illuminated (BI) and eight are front-illuminated (FI). The response of the BI devices extends to energies below that accessible to the FI chips. The chip-average energy resolution of the BI devices is better than that of the FI devices. Many of the characteristics of the ACIS instrument are summarized in table 3.3.

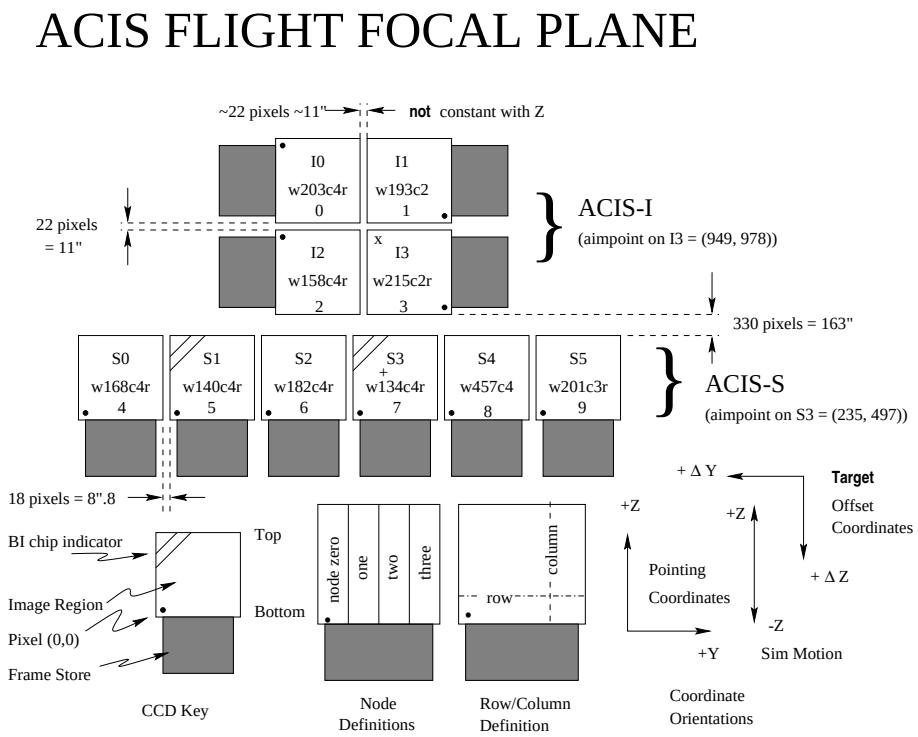

Figure 3.5: A schematic drawing of the ACIS focal plane; insight to the terminology is given in the lower left. Note the nominal aimpoints: on S3 (the '+') and on I3 (the '×').

Chapter 4

Analysis of HESS J1614−518 and HESS J1646−458

The H.E.S.S. Galactic Plane Survey has revealed ~ 40 unidentified VHE γ-ray sources. Origins of the many of the sources are still unclear, but some of them were identified as PWNe (Gallant et al., 2008). It is suspected that a major fraction of unidentified VHE γ-ray sources may be in fact PWNe.

In order to study the nature of unidentified VHE γ-ray sources, we have carried out two sets of Suzaku observations of the unidentified VHE γ-ray sources, HESS J1614−518 and HESS J1646−458.

Sections in this chapter are arranged as follows. We first describe the analysis and results of HESS J1614−518. We then describe the analysis and results of HESS J1646−458. Each section is almost independent; overview, observations, analysis and results, discussion and summary are given for each section.

4.1 HESS J1614−518

4.1.1 Overview and Previous Observation

HESS J1614−518 (hereafter HESS J1614) is one of the brightest, extended TeV γ-ray sources (Aharonian et al., 2005a, 2006a). It has two regions with intense γ-ray emission. Since it has no viable counterpart identified in other wavelengths, HESS J1614 is considered as a dark particle accelerator.

Matsumoto et al. (2008) observed HESS J1614 in 2006 with Suzaku, an X-ray astronomical satellite (Mitsuda et al., 2007), to identify the TeV γ-ray source in X-rays. Two X-ray sources were found in the 3–10 keV band. One of the X-ray objects, Suzaku J1614−5141 (src A), is extended and is located very close to the position of the 1st brightest peak of the TeV γ-ray emission. The other source, Suzaku J1614−5152 (src B), is located at the middle of two TeV γ-ray peaks in HESS J1614. Detailed analysis of src B was proven difficult with the Suzaku observation in 2006 as the source resides near the edge of the field of view and its flux estimate suffers significant uncertainties. Hence the

second Suzaku observation was conducted in 2008 in order to probe the nature of src B. We also observed the position of the 2nd brightest peak of the TeV γ-ray emission.

In the following sections, the results of the second Suzaku observation will be discussed; in addition, our own analysis on the XMM-Newton observation of the HESS J1614 region will be utilized to do a spatial analysis and to examine temporal behavior. The uncertainties in described parameters are at the 90% confidence level; the errors in data points and photon counts are at the 1σ level, unless otherwise stated.

4.1.2 Observations and Data Reduction

The south and center regions of HESS J1614 were observed on 2008 September 20 and 21, respectively. Figure 4.1 shows the Suzaku/X-ray Imaging Spectrometer (XIS: Koyama et al., 2007) field of views in these observations, together with that in the HESS J1614-North observation performed on 2006 September 16. The observations are summarized in table 4.1.

Suzaku consists of two distinct co-aligned scientific instruments. One is the X-ray Imaging Spectrometer (XIS: Koyama et al., 2007), which is an X-ray CCD camera located in the focal plane of the X-ray Telescope (XRT: Serlemitsos et al., 2007). The other is the Hard X-ray Detector (HXD: Kokubun et al., 2007; Takahashi et al., 2007), which is a non-imaging detector. The observations were performed with the three CCD cameras (XISs). One of the XIS sensors (XIS 1) has a back-illuminated (BI) CCD, while the other two (XISs 0 and 3) utilize front-illuminated (FI) CCDs. One of the FIs (XIS 2) suffered catastrophic damage on 2006 November 9, so that no useful data were obtained. The XIS was operated in the normal clocking mode (without the Burst or Window options) with the Spaced-row Charge Injection (SCI) (Uchiyama et al., 2009b). The HXD data were also available.

We analyzed the data with the processing version of 2.2.11.22,[1] utilizing the HEADAS software (version 6.8) and the calibration database (CALDB) released on 2010 February 18. All data affected by the South Atlantic Anomaly and telemetry saturation were excluded. We excluded the data obtained with an elevation angle from the Earth rim of $< 5°$. Additionally, for the XIS data, we also excluded the data obtained with that from the bright Earth rim of $< 20°$ and removed hot/flickering pixels. After these data screenings, the effective exposures for the XIS data were 53.7 ks and 47.7 ks, and those for the HXD-PIN data were 40.9 ks and 43.0 ks, on the HESS J1614-South and the HESS J1614-Center, respectively.

4.1.3 Analysis and Results

XIS Image

We extracted XIS images from each sensor using the screened data for the soft- and hard-energy bands. For the FI sensors, the soft- and hard-bands are defined as 0.4–3 keV and 3–10 keV, respectively, while those for the BI sensor are defined as 0.3–3 keV and

[1] See ⟨http://www.astro.isas.jaxa.jp/suzaku/process/history/v221122.html⟩.

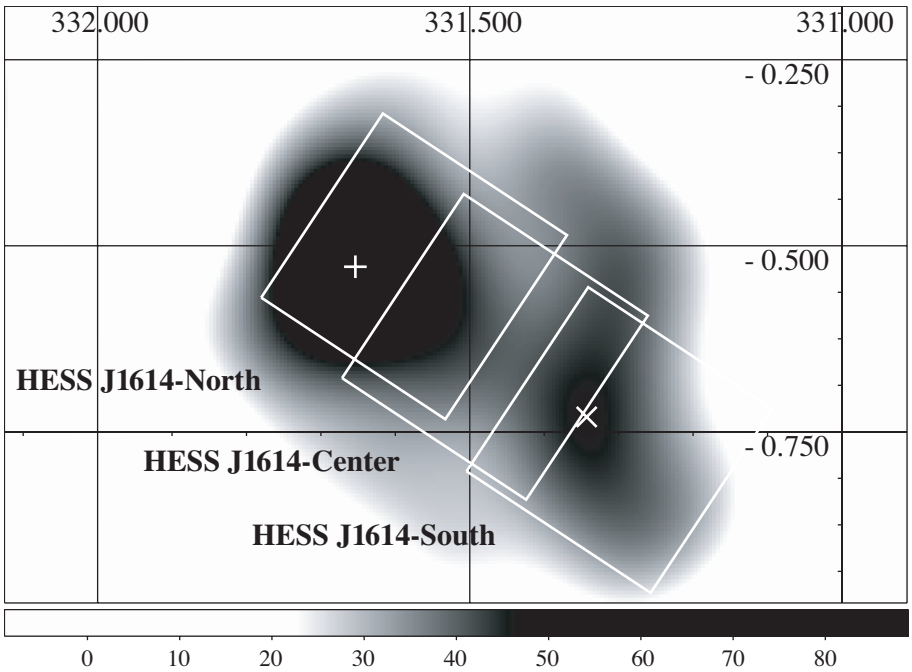

Figure 4.1: Suzaku/XIS field of views (thick boxes) overlaid on the H.E.S.S. smoothed excess map. The scale bar below the figure represents the excess. The coordinates on the interior frame are Galactic. The plus and cross marks represent the positions of the 1st and 2nd brightest peaks of the TeV γ-ray emission.

Table 4.1: Log of Suzaku observations.

Name	OBSID	Pointing direction		Observation start	Effective exposure (ks)	
		l	b	(UT)	XIS	HXD-PIN
HESS J1614-South	503073010	331°.2990	−0°.7611	2008/09/20 18:18	53.7	40.9
HESS J1614-Center	503074010	331°.4663	−0°.6358	2008/09/21 13:31	47.7	43.0
HESS J1614-North[1]	501042010	331°.5717	−0°.5274	2006/09/15 16:00	44.5	-

[1] Matsumoto et al. (2008).

3–7 keV, respectively. We excluded the corners of the CCD chips illuminated by the ^{55}Fe calibration sources. The images of the non-X-ray background (NXB) were generated using `xisnxbgen` (Tawa et al., 2008) and subtracted from the HESS J1614 images. Then, the soft- and hard-band images were divided by flat sky images simulated at 1.49 and 4.5 keV using the XRT+XIS simulator `xissim` (Ishisaki et al., 2007) for vignetting corrections. The images from the two FI sensors were summed and binned by a factor of 8.

The XIS FI images of the HESS J1614 region (HESS J1614-South and HESS J1614-Center) shown in figure 4.2 were smoothed using a Gaussian function with $\sigma = 0'.21$. The BI images were essentially the same, except for the poorer statistics. In the soft-band image, a bright X-ray object with a peak position of $(l,\ b) = (331°.45,\ -0°.59)$ [2] was found. The position uncertainty, defined as a sigma of a Gaussian function obtained by fitting the projection of the object along the Galactic longitude, was $0'.4$. Thus, this object is coincident with Suzaku J1614−5152 (src B). Src B was also conspicuous in the hard-band image.

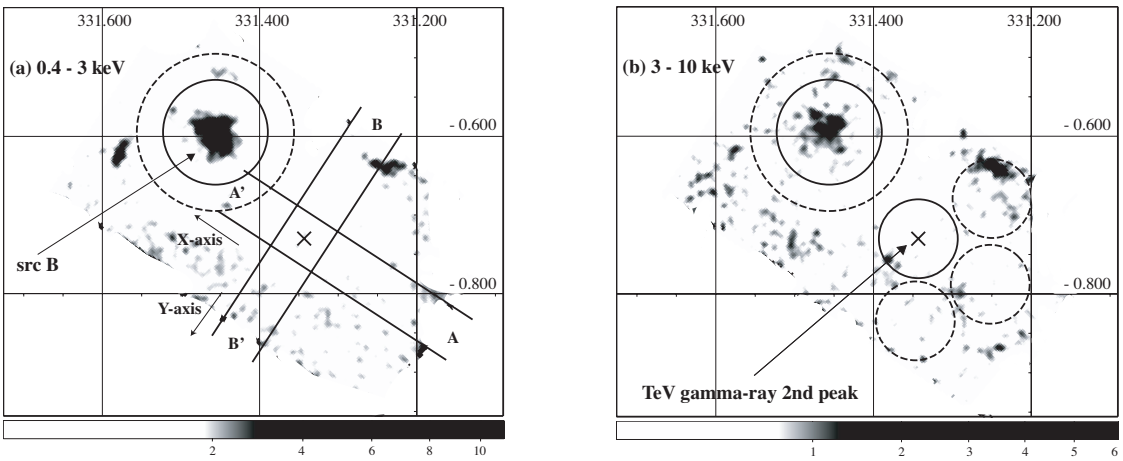

Figure 4.2: Suzaku XIS FI (XIS 0+3) images of the HESS J1614 region (HESS J1614-South and HESS J1614-Center) in the Galactic coordinates: (a) 0.4–3 keV and (b) 3–10 keV bands. The images were smoothed using a Gaussian function with $\sigma = 0'.21$. A vignetting correction was applied after subtracting the NXB, as described in the text. The cross mark represents the position of the 2nd brightest peak of the TeV γ-ray emission. The solid lines in the left panel show the regions used for the photon count profiles shown in figure 4.3. The solid circle and the dashed circles in the right panel show the regions used for the determination of the upper limit to the X-ray emission. The solid circle centered on src B is the integration region of source photons, and the dashed circle excluding the source region is that of background photons.

HESS J1614-South There is no apparent X-ray structure suggesting an X-ray counterpart of the 2nd peak of the TeV γ-ray emission in either the soft- and hard-band images.

[2] $(\alpha,\ \delta)_{\rm J2000.0} = (16^h14^m04^s,\ -51°52'27'')$.

To examine this quantitatively, we made photon count profiles along the strips AA′ and BB′ with a width of 3′.7 in figure 4.2; the profiles are shown in figure 4.3. We see no systematic trend, consistent with the TeV γ-ray profile of HESS J1614-South described by a Gaussian function with $\sigma = 9'.0$ (Rowell et al., 2008), in either the soft and hard X-ray profiles. These profiles strengthen the absence of the X-ray counterpart corresponding to the 2nd peak of the TeV γ-ray emission.

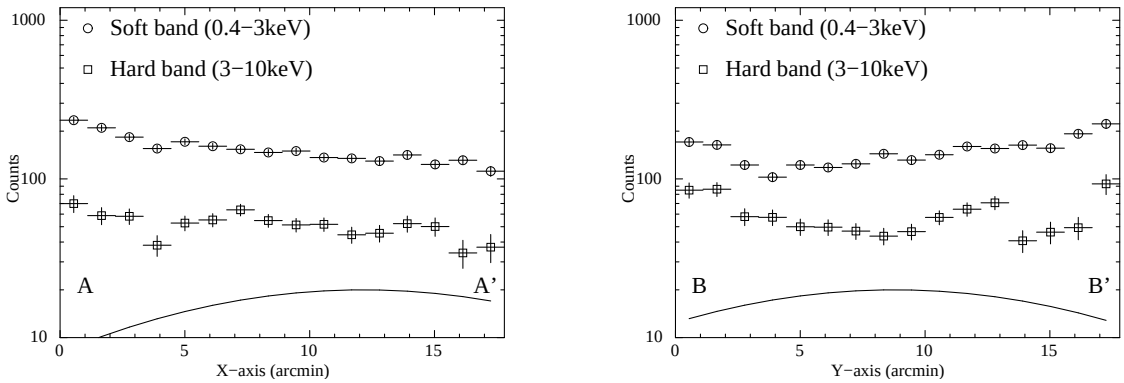

Figure 4.3: Photon count profiles of the XIS images along the strips AA′ (left) and BB′ (right) shown in figure 4.2(a). The solid curve shows the Gaussian function of $\sigma = 9'.0$, which expresses the TeV γ-ray profile of HESS J1614-South.

HESS J1614-Center We created the radial profile of src B and compared it with a point-spread function (PSF). The origin of the radial profile of src B was the peak of the X-ray emission. As for the PSF, we obtained the radial profile using the SS Cyg data observed on 2005 November 2 (OBSID=400006010), which are the verification phase data for the imaging capability of the XRT (Serlemitsos et al., 2007). Since the energy dependence of the PSF is negligible (Serlemitsos et al., 2007), the radial profile was extracted from the 0.4–10 keV band. In this analysis, NXB subtraction and vignetting correction were not applied to both the radial profile of src B and the PSF. Figure 4.4 shows the radial profile of src B in the 3–10 keV band. The profile cannot be fitted with the PSF plus a constant component model (χ^2/d.o.f. = 304.4/48), and therefore src B must be an extended source or unresolved multiple sources.

XIS Spectrum

HESS J1614-South There was no apparent X-ray counterpart corresponding to the 2nd peak of the TeV γ-ray emission, and we estimated the upper limit of the X-ray flux of this region. In order to determine the upper limit, we assumed a spectrum similar to src A; an absorbed power law with the photon index $\Gamma = 2.0$ and the hydrogen-equivalent column density $N_{\rm H} = 1.2 \times 10^{22}$ cm^{-2} (Matsumoto et al., 2008). The cross sections of photoelectric absorption were obtained from Morrison & McCammon (1983).

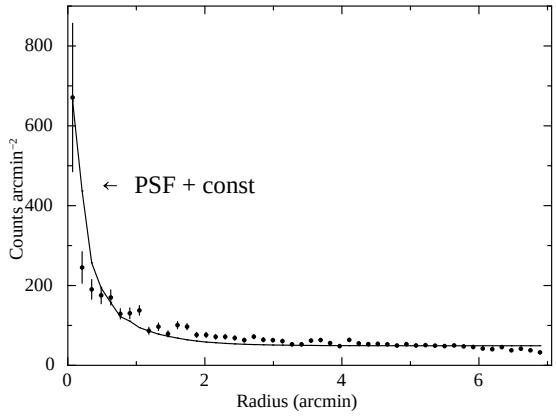

Figure 4.4: Radial profile of src B extracted from the 3–10 keV band image of the XIS FI sensor (XIS 0+3). The solid line represents the XIS PSF profile with a constant component.

We extracted the photons from the source region, the solid circle with a radius of $3'$ centered on the TeV γ-ray 2nd peak in figure 4.2(b), in the 2–10 keV band using the FI sensors (XISs 0 and 3). The number of the accumulated photons was 1111 ± 33 counts. Using three source-free regions surrounding the source region, the dashed circles around the TeV γ-ray 2nd peak in figure 4.2(b), we estimated the photons of the background emission. The number of the accumulated photons scaled the area to that of the source region was 1194 ± 35 counts. The exposure of the source was the same as that of the background. Thus, the number of the source minus background photons was -83 ± 48 counts, and the 3σ confidence upper limit on the photons in the source region was estimated to be 61 counts. Therefore, the 3σ confidence upper limit on the count rate in the source region was 1.1×10^{-3} counts s^{-1}. Then, we calculated the flux upper limit with Redistribution Matrix Files (RMFs) and Ancillary Response Files (ARFs). We obtained RMFs using the `xisrmfgen`, and made ARFs for a flat emission with the `xissimarfgen` software (Ishisaki et al., 2007). The 3σ upper limit on the surface brightness is 5.6×10^{-15} erg cm^{-2} s^{-1} arcmin^{-2}. Therefore, the upper limit on the flux from the circle of $3'$ radius (figure 4.2(b)) is 1.6×10^{-13} erg cm^{-2} s^{-1}.

HESS J1614-Center A source region for src B is defined as the solid circle centered on src B in figure 4.2. We extracted light curves of src B in the soft- and hard-energy bands and found no significant time variability from them. Then, we extracted the XIS spectra of src B and subtracted background spectra. The source photons were extracted from the source region, whereas those of the background were extracted from the dashed circle excluding the source region (figure 4.2). We then combined the background-subtracted spectra obtained from the two FI sensors. We obtained RMFs and ARFs for a point source using the `xisrmfgen` and `xissimarfgen` software.

The spectra of src B are shown in figure 4.5. We fitted the spectra with an ab-

sorbed power-law model. The hydrogen-equivalent column density $N_{\rm H}$, the photon index Γ, and the normalization were set to be free parameters. The best-fit parameters are $N_{\rm H} = 1.1^{+0.2}_{-0.1} \times 10^{22}$ cm^{-2} and $\Gamma = 3.2^{+0.3}_{-0.2}$. The best-fit χ^2 value is 103.47 for 128 degrees of freedom. The observed flux in the 2–10 keV band is F(2–10 keV) = 5.2×10^{-13} erg cm^{-2} s^{-1}.

We also tried fitting an absorbed blackbody model. The following are the best-fit parameters: $N_{\rm H} = 0.29^{+0.10}_{-0.09} \times 10^{22}$ cm^{-2} and $kT = 0.52^{+0.04}_{-0.03}$ keV. However, the best-fit χ^2 value of 169.24 for 128 degrees of freedom rejected the validity of the blackbody model at a confidence level of 99%.

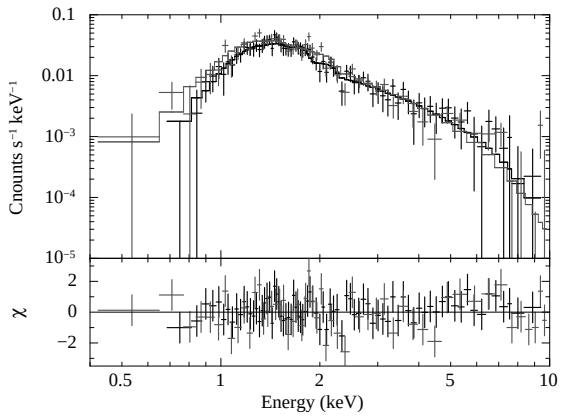

Figure 4.5: XIS spectra of src B, shown with the best-fit power-law model. Black and gray lines represent the data and model for the XIS FI (XIS0+3) and XIS BI (XIS1), respectively.

HXD Data Analysis

We also analyzed the HXD-PIN data of HESS J1614-Center, which includes src B. The HXD-PIN spectrum of HESS J1614-Center was extracted after the selection of a good time interval (GTI). As for the selection, we made a new GTI by ANDing the GTI from the NXB file provided by the HXD team with the GTI in the screened event file. Dead-time correction was also applied to the extracted source spectrum. Since the NXB from charged particles modeled by the HXD team does not contain the cosmic X-ray background (CXB) component (Boldt, 1987), we simulated the CXB for HESS J1614-Center following a recipe[3] provided by the HXD team. We also used the response file provided by the HXD team. Note that the accuracy of the HXD-PIN background model was estimated to be better than 3% in the 15–40 keV range (Fukazawa et al., 2009).

The observed HXD-PIN count of HESS J1614-Center in the 15–40 keV band was 11559 ± 108 counts. The NXB and the simulated CXB count in the 15–40 keV band

[3]See ⟨http://heasarc.nasa.gov/docs/suzaku/analysis/pin_cxb.html⟩.

were 10432 ± 102 counts and 642 ± 25 counts, respectively. Thus, the observed HXD-PIN minus NXB+CXB count was 485 ± 150 counts. However, considering the accuracy of the HXD-PIN background model of 3%, the lower limit on the source count of HESS J1614-Center became 172 ± 151 counts, and the detection was at only 1.1σ. There are not enough net counts to study the HXD-PIN spectrum. We also searched a pulsation in the HXD-PIN data, but we did not detect any pulsation in the 15–40 keV band.

XMM-Newton Analysis

The XMM-Newton observation of the HESS J1614 region was carried out from 2007 February 13 17:54 (UT) to February 14 03:07 (UT) (OBSID=0406550101), and this observation covered the HESS J1614-Center region with the EPIC instrument, which consists of one pn-type CCD camera (Strüder et al., 2001) and two MOS CCD cameras (Turner et al., 2001). In our Suzaku analysis, the radial profile of src B indicates that src B must be an extended source or unresolved multiple sources, and the light curves of src B do not show the time variability. The EPIC instrument provides a high spatial resolution, whose PSF (half energy width) is $\sim 15''$. Moreover, the time resolutions of each EPIC instrument are much better than the Suzaku/XIS (8 s), 73.4 ms for the pn and 2.6 s for the MOS in the full-frame mode. We therefore analyzed the XMM-Newton archival data.

The pn, MOS1 and MOS2 were operated in the standard full-frame mode using the medium filter. We used the Standard Analysis System (SAS) software version 10.0.0 for event selection. We selected the photons with the PATTERN of 0–4 for the pn and those of 0–12 for the MOS1 and MOS2, as valid X-ray events. We removed the time intervals in which the count rate in the 10–12 keV band within the entire field of view was higher than 0.25 counts s^{-1} for the pn and 0.20 counts s^{-1} for the MOS1 and MOS2, since such events are considered to be a rapid increase in the background induced by soft protons. The resultant exposure time was 1 ks for the pn and 10 ks for the MOS1 and MOS2. Since the photon statistics were poor for the pn, we did not use the pn data in this analysis.

Image Analysis Figure 4.6 shows the combined MOS1 and MOS2 image in the 0.4–10 keV band. We found several sources within the source and background regions of src B used to create the XIS spectra. We therefore searched for X-ray point sources using the source detection task `edetect_chain` in the SAS software package. We set the lower threshold of maximum likelihood method used in `edetect_chain` to be 10 (corresponding roughly to 4σ detection). The point sources detected in the 0.4–10 keV band are shown with thick open circles in figure 4.6. Four point sources were detected in the XIS source region for src B, while only one point source was detected in the XIS background region for src B. We designated these objects as XMMU J161406.0−515225 (src B1), XMMU J161409.3−515213 (src B2), XMMU J161409.8−515352 (src B3), XMMU J161414.1−514857 (src B4), and XMMU J161426.8−515705 (src B5). For each point source, we accumulated photons from a circular region with a radius of $15''$, and then estimated their count rates. Table 4.2 summarizes the count rates of these detected point sources. We also gave the count rates of the XIS source and background regions for src B excluding the point sources in order to indicate the count rate of the background photons

in this field. The count rate of src B1 is higher than the other sources by a factor of ~ 5. Moreover, the peak position of src B1, $(l, b) = (331^\circ.45, -0^\circ.59)$ [4] with the position uncertainty of $2''.8$, is consistent with that of Suzaku src B. These indicate that Suzaku src B is multiple sources and the main object is src B1.

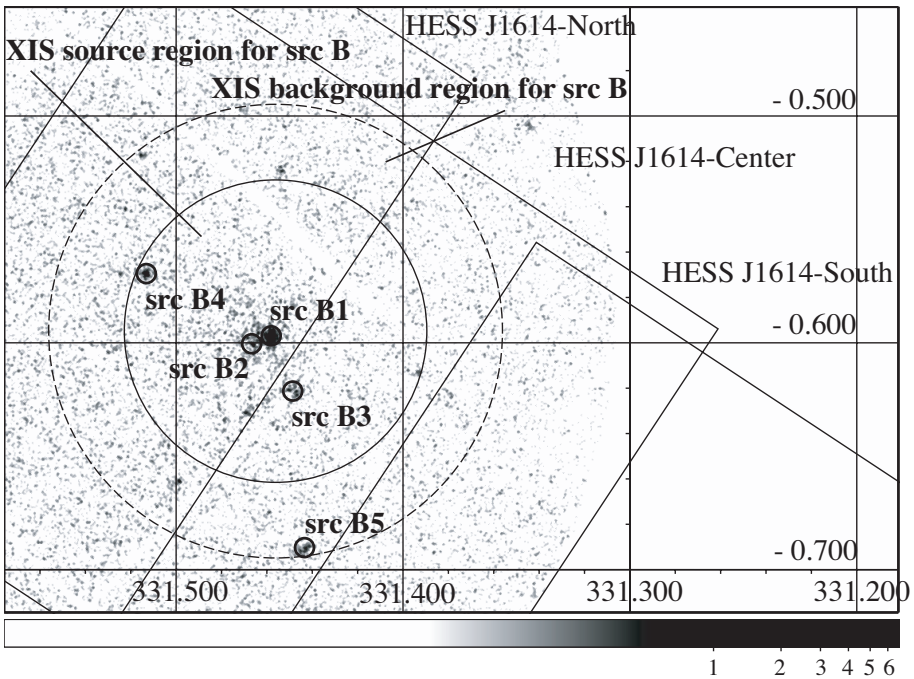

Figure 4.6: MOS 1+2 zoomed image in the 0.4–10 keV band including the XIS source (solid circle) and background (dashed circle excluding the source region) regions for src B. The solid squares represent the Suzaku/XIS field of views of the HESS J1614-North/HESS J1614-Center/HESS J1614-South observations. We also show the extraction regions for the detected point sources, which are used to estimate the source count rates, with thick open circles. Lines of constant Galactic latitude and longitude are plotted and labeled in the interior of the figure.

Figure 4.7 shows the radial profile of src B1 extracted from the MOS detectors in the 1.2–2.4 keV band; The origin of the radial profile was the peak of the X-ray emission, and NXB subtraction and vignetting correction were not applied to it. Then, we compared it with a point-spread function (PSF) in order to investigate whether or not src B1 is a point source. Since the PSF of the XMM-Newton telescopes depends on the energy, we used the PSF at an energy of 1.8 keV. We parameterized the PSF at 1.8 keV with a King-type function: $\mathrm{PSF}(r) = A(1 + (r/r_{\rm c})^2)^\alpha$, where A is a normalization, $r_{\rm c} = 4''.36$ is a core radius and $\alpha = -1.41$ is a slope (see the XMM-SOC-CAL-TN-0022 and XMM-SOC-CAL-TN-0029 documents online at http://xmm.vilspa.esa.es). We fitted the radial profile in the range of $0''.1 < r < 200''$ with the above PSF model plus constant which

[4] $(\alpha, \delta)_{\rm J2000.0} = (16^h14^m06^s, -51^\circ52'25'')$.

Table 4.2: Count rates of XMM-Newton data.

Region	R.A. (J2000.0)	Decl. (J2000.0)	Count rate[1] [10^{-3} counts s^{-1}] 0.4 – 3 keV	3 – 10 keV	Total
src B1[2]	16 14 06	−51 52 25	22.7±1.0	2.03±0.31	24.7±1.1
src B2[2]	16 14 09	−51 52 13	4.70±0.48	0.629±0.175	5.33±0.51
src B3[2]	16 14 09	−51 53 52	3.59±0.42	0.437±0.146	4.03±0.44
src B4[2]	16 14 14	−51 48 57	4.66±0.48	0.776±0.194	5.43±0.51
src B5[2]	16 14 26	−51 57 05	3.83±0.43	0.242±0.108	4.08±0.44
XIS source region − (src B1 + src B2 + src B3 + src B4)[3]			0.670±0.011	0.405±0.009	1.07±0.01
XIS background region − src B5[3]			0.563±0.009	0.377±0.008	0.940±0.012

[1] All errors are at the 1σ confidence level.
[2] Extraction regions are the circle with a radius of 15″.
[3] Extraction regions are scaled to the circle with a radius of 15″.

represents the background. In this fit, the normalization and the constant were free. We overlaid the best-fit model on the radial profile in figure 4.7. The best-fit χ^2 value is 109.6 for 98 degrees of freedom. This result suggests that src B1 is a point source.

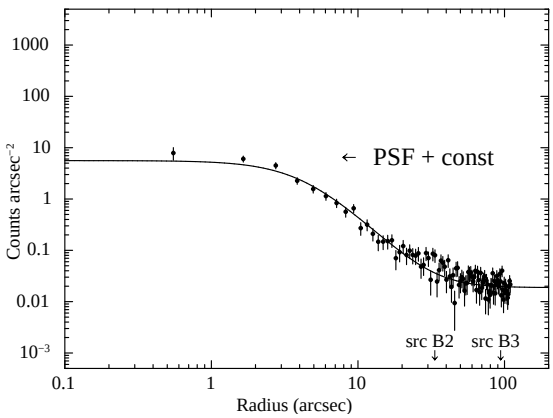

Figure 4.7: Radial profile of src B1 extracted from the MOS detectors in the 1.2–2.4 keV band. The solid line represents the PSF profile with a constant component. The downward arrows represent the positions of src B2 and src B3 (see figure 4.6)

Spectral Analysis

In order to check for consistency with the Suzaku results, we extracted the MOS spectra of the XIS source region for src B and subtracted the background spectra of the XIS background region for src B (figure 4.6). We fitted the spectra with an absorbed power-law model. The fit is acceptable with the best-fit χ^2 value of 47.98 for 65 degrees of freedom. The best-fit parameters are $N_{\rm H} = 1.1^{+0.4}_{-0.3} \times 10^{22}$ cm^{-2} and $\Gamma = 3.0^{+0.6}_{-0.5}$. The observed flux in the 2–10 keV band is F(2–10 keV) $= 6.9 \times 10^{-13}$ erg cm^{-2} s^{-1}. Figure

4.8 shows the background-subtracted spectra together with the best-fit model and the fit residuals. The best-fit results of Suzaku src B and XMM-Newton src B are summarized in table 4.3. The best-fit parameters of src B are consistent with Suzaku and XMM-Newton. The X-ray flux of XMM-Newton is $\sim 30\%$ larger than that of Suzaku, and this may indicate time variability.

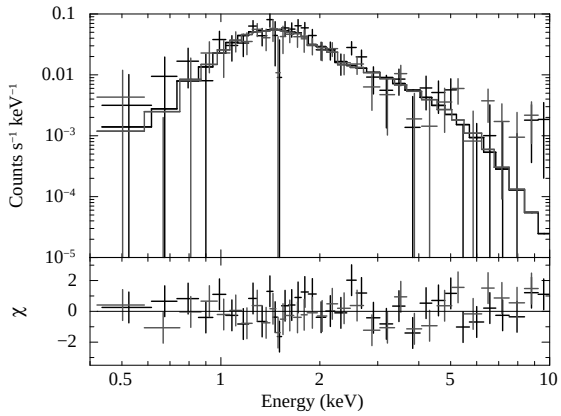

Figure 4.8: MOS1 (black) and MOS2 (grey) spectra of src B. The data and their best-fit power-law model are represented by cross marks and solid lines, respectively.

Table 4.3: Best-fit results of the X-ray spectra.[1]

	Suzaku src B	XMM-Newton src B	XMM-Newton src B1	
Model[2]	PL	PL	PL	BB
$N_{\rm H}$ (10^{22} cm^{-2})	$1.1^{+0.2}_{-0.1}$	$1.1^{+0.4}_{-0.3}$	$2.4^{+0.4}_{-0.4}$	$1.1^{+0.3}_{-0.2}$
$\Gamma/(kT)$ (keV)	$3.2^{+0.3}_{-0.2}$	$3.0^{+0.6}_{-0.5}$	$5.2^{+0.6}_{-0.5}$	$0.38^{+0.04}_{-0.04}$
$F^{\rm obs}_{2-10{\rm keV}}$[3]	5.2	6.9	1.7	1.5
$F^{\rm abscor}_{2-10{\rm keV}}$[4]	6.1	8.0	2.8	2.0
χ^2/d.o.f.	103.47/128	47.98/65	21.98/25	24.91/25

[1] Errors are at the 90% confidence level.
[2] Model used for the spectral fitting: "PL" is a power-law model, and "BB" is a blackbody model.
[3] Observed flux in the 2–10 keV band in units of 10^{-13} erg cm^{-2} s^{-1}.
[4] Absorption corrected flux in the 2–10 keV band in units of 10^{-13} erg cm^{-2} s^{-1}.

Then, we extracted the MOS spectra of src B1. The circle with a radius of 20″ centered on src B1 was the extraction region of the source photons, whereas the XIS background region for src B excluding the circle with a radius of 20″ centered on src B5 was that of the background photons (figure 4.6). The spectra of src B1 are shown in figure 4.9. We fitted the spectra with an absorbed power-law model. The best-fit parameters are

$N_{\rm H} = 2.4^{+0.4}_{-0.4} \times 10^{22}$ cm^{-2} and $\Gamma = 5.2^{+0.6}_{-0.5}$. We also tried to fit the spectra by an absorbed blackbody model. The best-fit parameters are as follows: $N_{\rm H} = 1.1^{+0.3}_{-0.2} \times 10^{22}$ cm^{-2} and $kT = 0.38^{+0.04}_{-0.04}$ keV. The best-fit parameters of the power-law and blackbody models are listed in table 4.3. Moreover, we tried fitting a thermal plasma model (the MEKAL model: Mewe et al., 1985). However, the thermal model yielded an abundance of zero (< 0.044) solar, which is an extremely low abundance, and therefore is not realistic. Since the statistics were poor, it was impossible to study the spectra of the other sources.

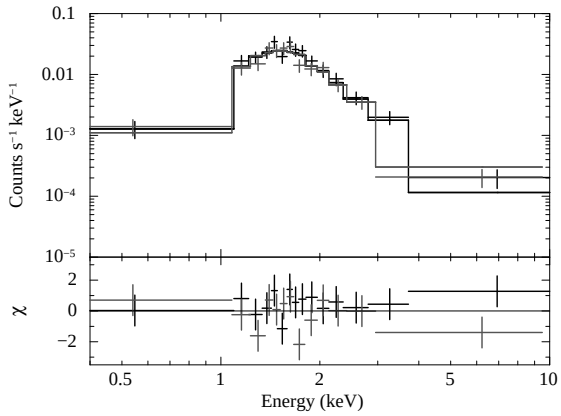

Figure 4.9: MOS1 (black) and MOS2 (grey) spectra of src B1. The data and their best-fit power-law model are represented by cross marks and solid lines, respectively.

Timing Analysis

We carried out a timing analysis of src B1. Since there was nearly no source flux below ~ 1 keV and above ~ 5 keV, we searched a pulsation in the 1–5 keV band for the MOS data. After barycentric correction to the event file, we created the light curve of src B1 with the minimum time resolution (2.6 s). The power spectrum on the basis of the combined MOS1 and MOS2 light curve in the 1–5 keV band is shown in figure 4.10. We did not detect a pulsation of src B1 for the MOS data.

4.1.4 Discussion

The TeV-to-X-ray flux ratio of HESS J1614

HESS J1614 has two regions with intense γ-ray emission. The γ-ray spectrum yields $\Gamma = 2.46$ and the flux in the 1–10 TeV band from a circular region with a radius of $0^\circ.4$ is estimated to be 1.8×10^{-11} erg cm^{-2} s^{-1} (Aharonian et al., 2006a). Matsumoto et al. (2008) found the hard extended emission, Suzaku src A, at the position of the 1st brightest peak of the TeV γ-ray emission, as the best candidate for the X-ray counterpart of HESS J1614; the best-fit parameters are $N_{\rm H} = 1.2^{+0.5}_{-0.4} \times 10^{22}$ cm^{-2} and $\Gamma = 1.7^{+0.3}_{-0.3}$, and

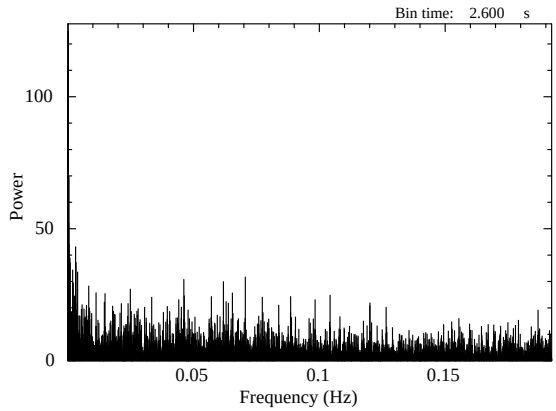

Figure 4.10: Power spectrum of src B1 in the 1–5 keV band with the time bin size of 2.6 s for the MOS data.

the flux of Suzaku src A in the 2–10 keV band is $F(2\text{–}10\ \text{keV}) = 5.3 \times 10^{-13}$ erg cm^{-2} s^{-1}. Additionally, we reveal that there is no evidence for the X-ray emission at the position of the 2nd brightest peak of the TeV γ-ray emission; the XIS sets the stringent upper limit of 1.6×10^{-13} erg cm^{-2} s^{-1} in the 2–10 keV band. As a result, the X-ray counterpart to the TeV γ-ray emission is just Suzaku src A. Therefore, it is ensured that the flux ratio $F(1\text{–}10\ \text{TeV})/F(2\text{–}10\ \text{keV})$ of HESS J1614 is ~ 34, which is still one of the largest values observed among extended VHE objects (see Matsumoto et al., 2007 and references therein).

The nature of HESS J1614

XMM-Newton src B1 is located at the middle of HESS J1614. Within the error circle of XMM-Newton src B1, there is an infrared source, 2MASS J16140610−5152264, at (l, b) = (331°.4579, −0°.5973). The X-ray spectrum of XMM-Newton src B1 is described using a power-law model with $\Gamma = 5.2^{+0.6}_{-0.5}$ or a blackbody model with $kT = 0.38^{+0.04}_{-0.04}$ keV. The best-fit column densities of both models are different by a factor of ~ 2. The best-fit column density of the power-law model is almost the same as the total Galactic HI column density towards the HESS J1614 region ($\sim 2.2 \times 10^{22}$ cm^{-2}: Dickey & Lockman, 1990), while that of the blackbody model is approximately equal to half of it. On the other hand, the best-fit column density of the power-law model is about twice larger than that of Suzaku src A, while that of the blackbody model is almost the same as that of Suzaku src A. If we assume the blackbody emission, XMM-Newton src B1 may be at about the same distance to Suzaku src A and may also be physically related to HESS J1614.

An object which shows a soft X-ray spectrum like XMM-Newton src B1 includes an anomalous X-ray pulsar (AXP: Mereghetti, 2008). The spectra of AXPs are described by steep power laws ($\Gamma > 3$) and/or blackbody models with low temperature ($kT \leq 0.5$ keV). AXPs often show time variability with a period of 2–12 s. However, no such variability

was found from XMM-Newton src B1.

If XMM-Newton src B1 is related to Suzaku src A and HESS J1614, the nature of HESS J1614 is similar to that of CTB37B (Nakamura et al., 2009). CTB37B is an SNR which has the diffuse non-thermal power-law component ($\Gamma \sim 1.5$) at the position of the TeV γ-ray emission. Moreover, the point source which shows the soft spectrum considered to be an AXP was found at the offset position of the TeV γ-ray emission (Nakamura et al., 2009; Sato et al., 2010). Thus, if XMM-Newton src B1 is an AXP, HESS J1614 may be an SNR associated with an AXP. In that case, it is considered that XMM-Newton src B1 is an AXP produced by a supernova explosion, and a shocked region in the SNR can be seen as Suzaku src A. The approximate radius of HESS J1614 ($r \sim 10' = 30$ pc @ 10 kpc) suggests that HESS J1614 may be an SNR with an age of $\sim 10^5$ yr (Padmanabhan, 2001). Yamazaki et al. (2006) suggested that the ratio of TeV γ-ray to X-ray energy flux of old SNRs with an age of $\sim 10^5$ yr could be very large, in some instances more than ~ 100. The flux ratio of HESS J1614 is in agreement with this scenario. Here, we assume the distance to HESS J1614 is 10 kpc, since the best-fit column density of the blackbody model which is almost the same as that of Suzaku src A, is approximately equal to half of the total Galactic HI column density towards the HESS J1614 region. Assuming a distance of 10 kpc, the luminosities of XMM-Newton src B1 in the 2–10 keV band are 3×10^{33} erg s^{-1} for the power-law model and 2×10^{33} erg s^{-1} for the blackbody model. These luminosities are consistent with that of AXPs (e.g., The McGill SGR/AXP Online Catalog.[5]). Meanwhile, assuming a distance of 10 kpc, the luminosity of Suzaku src A in the 2–10 keV band is 6×10^{33} erg s^{-1} (Matsumoto et al., 2008). This luminosity is smaller than the synchrotron X-ray luminosity of young SNRs (e.g., Dyer et al., 2004).

Recently, Mizukami et al. (2011) discussed the possible counterparts and considered radiation mechanisms based on hadronic and leptonic processes, by combining their CANGAROO-III result with multi-wavelength data. They discussed two scenarios to explain the large flux ratio of HESS J1614. One is a time-evolving electron injection model, in which the number of electrons injected into space by the pulsar decreases proportionally to the spin-down of the pulsar (Funk et al., 2007; Higashi et al., 2008). The other is an old SNR scenario, in which the large flux ratio is expected, because of the difference between the cooling times of electrons and protons (Yamazaki et al., 2006). They concluded that hadronic-origin emission from an unknown supernova remnant is preferred although a leptonic origin from a PWN driven by an unknown pulsar remains possible. Our results that HESS J1614 may be an old SNR with an AXP support this conclusion.

On the other hand, Rowell et al. (2008) suggested the relation between HESS J1614 and Pismis 22. Pismis 22 is an open cluster characterized by the following cluster fundamental parameters: E(B−V) color excess = 2.00±0.10 mag, distance = 1.0±0.4 kpc and Age = 40±15 Myr (Piatti et al., 2000). Rowell et al. (2008) pointed out that Pismis 22 may easily account for the TeV luminosity if the cluster has a stellar wind luminosity of ten B-type stars and 20% of the stellar wind kinetic energy is converted to the γ ray. The size of Pismis 22 is $4'.0$, it is conceivable that XMM-Newton src B1 is within this cluster.

[5]See ⟨http://www.physics.mcgill.ca/∼pulsar/magnetar/main.html⟩.

However, according to the best-fit column densities of both models, the distance to XMM-Newton src B1 of 1.0 kpc is too close. Moreover, the spectrum of XMM-Newton src B1 cannot be described by the optically thin thermal plasma model seen from some O and B-type stars (Albacete Colombo et al., 2007). There are other TeV γ-ray sources, such as Cyg-OB2 (TeV J2032+4130), suspected the relation with the open cluster (Aharonian et al., 2002). However, in the case of TeV J2032+4130, the size of the extended X-ray emission is similar to that of the TeV γ-ray emission (Horns et al., 2007). Thus there are some differences with HESS J1614.

4.1.5 Summary

We observed the south and center regions of HESS J1614 with Suzaku. There was no positive detection at the 2nd peak position, and we set an upper limit of 1.6×10^{-13} erg cm^{-2} s^{-1} to the 2–10 keV band flux. The high value of $f_{\rm TeV}/f_{\rm X} \sim 34$ may suggest that HESS J1614 is a proton accelerator. We also detected the soft X-ray source, Suzaku J1614−5152 (Suzaku src B), at the middle of HESS J1614. Using the XMM-Newton archival data, we revealed that Suzaku src B consists of multiple point sources. The brightest point source, XMMU J161406.0−515225 (XMM-Newton src B1), shows a soft X-ray spectrum. XMM-Newton src B1 might be an AXP and may be physically related to Suzaku J1614−5141 (Suzaku src A), which was found at the 1st peak position in the previous observation.

4.2 HESS J1646−458

4.2.1 Overview

The H.E.S.S. Collaboration has recently reported the detection of the degree-scale extended very-high-energy (VHE) γ-ray source HESS J1646−458 (Abramowski et al., 2012). The VHE γ-ray source is centered on the massive stellar cluster Westerlund 1 (Westerlund, 1961). Abramowski et al. (2012) proposed two scenarios. One is a single-source scenario, where Westerlund 1 is favored as site of VHE particle acceleration. Here, a hadronic parent population would be accelerated within the stellar cluster. The other is a multi-source origin, where a scenario involving the pulsar PSR J1648−4611 (Kramer et al., 2003) could be viable to explain parts of the VHE γ-ray emission of HESS J1646−458.

PSR J1648−4611 is a radio pulsar discovered by the Parkes Multibeam Pulsar Survey (Kramer et al., 2003). It is located at the position $(l, b) = (339°.4383, -00°.7938)$ [6] with a pulse period of $P = 0.1649$ s and a period derivative of $\dot{P} = 23.7 \times 10^{-15}$ s s^{-1}. The distance to the source was estimated to be $d = 5.7$ kpc from the pulsar's dispersion measure using the Taylor & Cordes (1993) model for the Galactic distribution of free electrons. The characteristic age and the spin-down luminosity are $\tau_c = 1.1 \times 10^5$ yr and $\dot{E} = 2.1 \times 10^{35}$ erg s^{-1}, respectively.

Recently, the Large Area Telescope (LAT) on the Fermi Gamma-ray Space Telescope (Fermi) detected γ-ray source that is spatially associated with the PSR J1648−4611 (2FGL J1648.4−4612; Nolan et al., 2012). A γ-ray pulse detection from this pulsar is also reported in the Public List of LAT-Detected Gamma-Ray Pulsars.[7] These results imply that the origin of the VHE γ-ray emission also relates to this pulsar. Active pulsars are losing a significant part of energy via relativistic particles, and form pulsar wind nebulae (PWNe). PWNe emit synchrotron emission from the radio to X-ray bands. In addition, some PWNe are known to be VHE γ-ray emitters. Thus, PSR J1648−4611 is a possible candidate for the source of the energy of HESS J1646−458. However, X-ray emission from PSR J1648−4611 has not been reported.

In the following sections, the results of the Suzaku observation of PSR J1648−4611 will be discussed; in addition, our own analysis on the Chandra observation of this region will be utilized to estimate the contribution of point sources. In this paper, uncertainties are described at the 90% confidence level, while the errors of data points in X-ray spectra and radial profiles are at the 1σ level, unless otherwise stated.

4.2.2 Observations and Data Reduction

Suzaku

We observed the PSR J1648−4611 region with Suzaku (Mitsuda et al., 2007) on 2010 September 23 and 24 (OBSID=505051010). The observation was performed with the

[6] $(\alpha, \delta)_{\rm J2000.0} = (16^h48^m22^s.0, -46°11'16''.0)$.

[7] See ⟨https://confluence.slac.stanford.edu/display/GLAMCOG/Public+List+of+LAT-Detected+Gamma-Ray+Pulsars⟩.

three CCD cameras (XISs: Koyama et al., 2007) located in the focal planes of the X-ray telescopes (XRTs: Serlemitsos et al., 2007) and the non-imaging detector (HXD: Kokubun et al., 2007; Takahashi et al., 2007). One of the XIS sensors (XIS 1) has a back-illuminated (BI) CCD, while the other two (XISs 0 and 3) utilize front-illuminated (FI) CCDs. Because one of the FIs (XIS 2) suffered catastrophic damage on 2006 November 9, no useful data were obtained. The XIS was operated in the normal clocking mode (without the Burst or Window options) with Spaced-raw Charge Injection (SCI) (Uchiyama et al., 2009b).

We analyzed the data with the processing version of 2.5.16.28,[8] utilizing the HEADAS software (version 6.11.1) and calibration database (CALDB) released on 2011 November 10. All data affected by the South Atlantic Anomaly and telemetry saturation were excluded. We excluded the data obtained with an elevation angle from the Earth rim of $< 5°$. Additionally, for the XIS data, we also excluded the data obtained with that from the bright Earth rim of $< 20°$ and removed hot/flickering pixels. After these data screenings, the effective exposure for the XIS data was 50.2 ks, and that for the HXD data was 40.8 ks. In this paper, we concentrate on the XIS data.

Chandra

Chandra observed the PSR J1648−4611 region on 2010 January 24 (OBSID=11836). The exposure time was 10.2 ks. Chandra has a superior angular resolving capability. We analyzed Chandra data in order to estimate the contribution of point sources and the intensity upper limit of an undetected source, using the Chandra Interactive Analysis of Observations (CIAO) software version 4.3.1 with CALDB version 4.4.6.

4.2.3 Analysis and Results

Images

We extracted XIS images in the soft- and hard-energy bands from each sensor using the screened data. For the FI sensors, the soft- and hard-bands are defined as 0.4–3 keV and 3–10 keV, respectively, while those for the BI sensor are defined as 0.3–3 keV and 3–7 keV, respectively. The corners of the CCD chips illuminated by the ^{55}Fe calibration sources were excluded. Non-X-ray backgrounds (NXB) generated with `xisnxbgen` (Tawa et al., 2008) were subtracted from the images. Then, the soft- and hard-band images were divided by flat sky images simulated at 1.49 and 4.5 keV using the XRT+XIS simulator `xissim` (Ishisaki et al., 2007) for vignetting corrections. The images were binned by a factor of 8. The images from the two FI sensors were summed.

Figure 4.11 shows the XIS FI images of the PSR J1648−4611 region smoothed using a Gaussian function with $\sigma = 0'.28$. The XIS BI images were essentially the same, except for the poorer statistics. In the hard-band image, an X-ray source with a peak position of $(l,\ b) = (339°.44,\ -0°.79)$ [9] was found, and was designated as Suzaku J1648−4610

[8] See ⟨http://www.astro.isas.jaxa.jp/suzaku/process/history/v251628.html⟩.

[9] $(\alpha,\ \delta)_{\rm J2000.0} = (16^h48^m20^s,\ -46°10'57'')$.

(Src A). The peak position of Src A is close to PSR J1648−4611. The spatial distribution of Src A in the soft-band image seems to be different from that in the hard-band image (Figures 4.11(a) and (b)). The peak position in the soft-band image is $(l,\ b) = (339°.44,\ -0°.78)$ [10] and is close to Src 1 found in a Chandra image (see the end of section 3.1).

Another X-ray source, found at $(l,\ b) = (339°.42,\ -0°.90)$ [11], was also bright in the soft X-ray band. We designated this source as Suzaku J1648−4615 (Src B). Src B was not conspicuous in the hard-band image.

We created a radial profile of Src A in the 3–10 keV band as shown in Figure 4.12, and the profile was compared with a point-spread function (PSF). The origin of the radial profile was the peak in the hard-band image. As for the PSF, we obtained the radial profile using the SS Cyg data observed on 2005 November 2 (OBSID=400006010), which are the verification phase data for the imaging capability of the XRT (Serlemitsos et al., 2007). Since the energy dependence of the PSF is negligible (Serlemitsos et al., 2007), the radial profile was extracted from the 0.4–10 keV band. In this analysis, the NXB subtraction and vignetting correction were not applied to both the radial profiles of Src A and the PSF. As shown in Figure 4.12, the profile cannot be fitted adequately with the PSF plus a constant component model ($\chi^2/d.o.f. = 146.1/48$), and therefore Src A must be diffuse emission or unresolved multiple sources.

Figure 4.13 shows the Chandra image around Src A in the 0.4–10 keV band. Several sources can be seen around Src A. A point source search was carried out in the image with `wavdetect`. This tool uses a wavelet method (Freeman et al., 2002). The wavelet scales of `wavdetect` were the $\sqrt{2}$ series: 1.0 1.414 2.0 2.828 4.0 5.657 8.0 11.314 16.0. The threshold significance was set to 10^{-6}, this is equivalent to stating that the expected number of false sources per the ACIS-I3 CCD chip is one. We resolved 5 point sources from the whole region of the ACIS-I3 CCD chip. Their positions and counts are listed in table 4.4. The point sources detected around Src A are indicated by solid circles with the source numbers in figure 4.13. From the SIMBAD Astronomical Database operated at CDS, Strasbourg, France, we found a counterpart of Src 1 at $(l,\ b) = (339°.4396,\ -00°.7792)$ [12] which is an A0 Star: HD 151228.

Table 4.4: Chandra point sources around the field of PSR J1648−4611.

Source numbers	*RA* (J2000.0)	*Dec* (J2000.0)	Counts[1] (0.4 – 10 keV)
Src 1	16 48 18.30	-46 10 39.4	26 ± 5
Src 2	16 48 16.16	-46 10 59.7	7 ± 3
Src 3	16 48 24.78	-46 10 16.6	8 ± 3
Src 4	16 48 34.95	-46 12 43.7	4 ± 2
Src 5	16 48 24.91	-46 08 39.6	3 ± 2

[1] The sum of all counts in the source cell minus the sum of the estimated background counts.

[10] $(\alpha,\ \delta)_{\mathrm{J2000.0}} = (16^h48^m18^s,\ -46°10'32'')$.
[11] $(\alpha,\ \delta)_{\mathrm{J2000.0}} = (16^h48^m45^s,\ -46°15'57'')$.
[12] $(\alpha,\ \delta)_{\mathrm{J2000.0}} = (16^h48^m18^s.4,\ -46°10'38''.5)$.

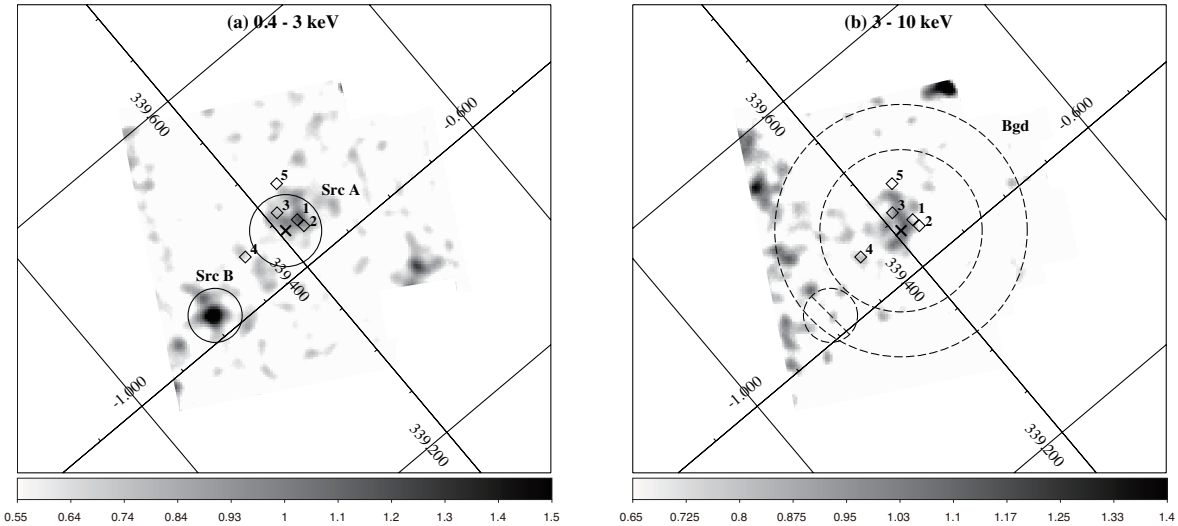

Figure 4.11: Suzaku XIS FI (XIS 0+3) images of the PSR J1648−4611 region in the Galactic coordinates: (a) 0.4–3 keV and (b) 3–10 keV bands. The images were smoothed using a Gaussian function with $\sigma = 0'.28$. A vignetting correction was applied after subtracting the NXB, as described in the text. The cross mark represents the position of PSR J1648−4611. The numbered diamond points mark the Chandra point sources, whose properties are listed in table 4.4. The source regions for the spectrum of Src A and Src B are shown by the solid circles. The background region is shown by the dashed annulus excluding the source region of Src B.

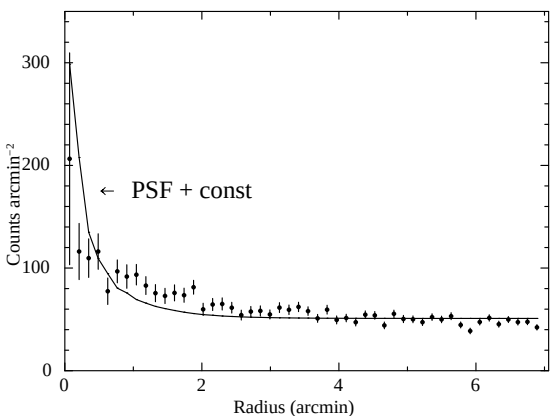

Figure 4.12: Radial profile of Src A extracted from the 3–10 keV band image of the XIS FI sensor (XIS 0+3). The solid line represents the XIS PSF profile with a constant component.

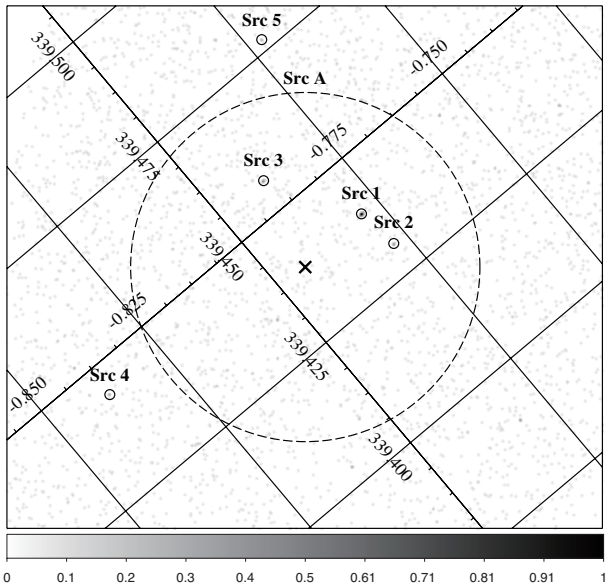

Figure 4.13: Chandra image around PSR J1648−4611 in the 0.4–10 keV band including the XIS source region for Src A (dashed circle). Point sources are indicated by solid circles with the source numbers. Src 1 is coincident with HD 151228. The cross mark represents the position of PSR J1648−4611. Lines of constant Galactic latitude and longitude are plotted and labeled in the interior of the figure.

Spectra

Src A An X-ray spectrum of Src A of each XIS sensor was extracted from a circular region with a radius of $2'$. An annulus region with an inner radius of $4'.5$ and an outer radius of $7'$ was used for a background spectrum. NXB spectra in the source and background regions were constructed using `xisnxbgen` (Tawa et al., 2008), and the NXB were subtracted from the source and background spectra. When the background spectrum was subtracted from the source spectrum, a vignetting correction was taken into account. The spectra of Src A thus obtained are shown in figure 4.14. In the spectrum analysis below, Redistribution Matrix Files (RMFs) and Ancillary Response Files (ARFs), made using the softwares `xisrmfgen` and `xissimarfgen` (Ishisaki et al., 2007), were used.

The Chandra image (figure 4.13) shows that the Src A region includes three point sources. A Chandra spectrum including all three sources was constructed in order to estimate the contribution of the point sources to the Suzaku spectra. Circular regions with a radius of $3''.4$ centered on each source were used for the source spectrum, and annular regions with an inner radius of $5''$ and an outer radius of $12''.6$ around each source were used for a background spectrum. The spectrum thus obtained (figure 4.15) is soft where almost no X-ray photon can be seen above 2 keV. Note that the Suzaku soft-band image seems to follow the distribution of the Chandra point sources, while the hard-band image shows a different distribution (figure 4.11). This suggests that the soft emission of Src A is attributed to the Chandra sources and that the origin of the hard

emission of Src A is different from that of the soft emission. We fitted a bremsstrahlung model with interstellar absorption to the Chandra spectrum of point sources in the 0.4–2 keV band. The cross sections of the photoelectric absorption were obtained from Morrison & McCammon (1983). A hydrogen-equivalent column density $N_{\rm H}$, plasma temperature kT, and a normalization were set to be free parameters. The best-fit parameters are $N_{\rm H} = 0.1^{+0.7}_{-0.1} \times 10^{22}$ cm^{-2} and $kT = 0.45^{+0.60}_{-0.28}$ keV, and $\chi 2/d.o.f.$=5.99/15. The observed flux in the 0.4–2 keV band is F(0.4–2 keV) $= (3.4 \pm 1.0) \times 10^{-14}$ erg cm^{-2} s^{-1}.

The Suzaku spectra of Src A in the 0.4–2 keV band were compared with simulated spectra of the Chandra sources within the Src A region. In the simulation, we took into account the leakage of photons from Srcs 1, 2, and 3, and the contamination from Srcs 4 and 5. Since the count rates of Srcs 4 and 5 were quite small (table 4.4), a qualitative analysis of the combined spectrum of Srcs 4 and 5 was impossible. We assume that Srcs 4 and 5 have the same spectral shape as the best-fit model to the Chandra Srcs 1, 2, and 3. The count rates of the Chandra sources were varied, but the ratios between them were fixed according to the values in table 4.4. We found that the Suzaku spectra in the 0.4–2 keV band can be explained ($\chi^2/d.o.f = 20.37/15$) when the total flux of the Chandra Srcs 1, 2, and 3 is $(2.6 \pm 1.3) \times 10^{-14}$ erg cm^{-2} s^{-1} (figure 4.16). This value is consistent with the above Chandra result of $(3.4 \pm 1.0) \times 10^{-14}$ erg cm^{-2} s^{-1}, and it is reasonable to conclude that the Suzaku soft-band spectra of Src A can be explained by the Chandra point sources.

On the other hand, the Suzaku spectra of Src A in the 2–10 keV band cannot be described by the Chandra point sources alone having soft X-ray emission. In the model fitting of the Suzaku spectra of Src A in the 0.4–10 keV band, we added a power-law component modified by interstellar absorption to explain the remaining hard X-ray emission. A hydrogen column density ($N_{\rm H}$), a photon index (Γ), and a normalization were free parameters. The spectra of Src A with the best-fit model are shown in figure 4.16; the best-fit parameters are $N_{\rm H} = 3.4^{+2.4}_{-1.6} \times 10^{22}$ cm^{-2}, $\Gamma = 2.0^{+0.9}_{-0.7}$, and $\chi 2/d.o.f.$=60.49/55. The observed flux of the power-law component in the 2–10 keV band is F(2–10 keV) $= 1.4 \times 10^{-13}$ erg cm^{-2} s^{-1}. The contribution of point sources is indicated by the dotted lines in the soft-band. The additional dotted lines in the hard-band show the power-law model.

Src B The Suzaku spectra of Src B were extracted from a circular region centered on Src B. We found no counterpart for Src B in literatures. A circle with a radius of $1'.5$ is used as the source region and an annulus with an inner radius of $4'.5$ and an outer radius of $7'$ is used for the background. The spectra of Src B are shown in figure 4.17. We fitted the spectra with an absorbed power-law model. The best-fit parameters are $N_{\rm H} = 0.3^{+0.3}_{-0.2} \times 10^{22}$ cm^{-2}, $\Gamma = 3.0^{+1.4}_{-0.8}$, and $\chi 2/d.o.f.$=29.88/31. The observed flux in the 0.4–10 keV band is F(0.4–10 keV) $= 6.4 \times 10^{-14}$ erg cm^{-2} s^{-1}.

We also tried to fit an absorbed thermal plasma model (the APEC model: Smith et al., 2001). The thermal model yields a hydrogen column of zero ($< 1.0 \times 10^{22}$) cm^{-2}, a temperature of $1.9^{+1.1}_{-1.3}$ keV, an abundance of 0.26 (< 1.03) solar, and $\chi 2/d.o.f.$=28.73/30. The observed flux in the 0.4–10 keV band is F(0.4–10 keV) $= 6.4 \times 10^{-14}$ erg cm^{-2} s^{-1}.

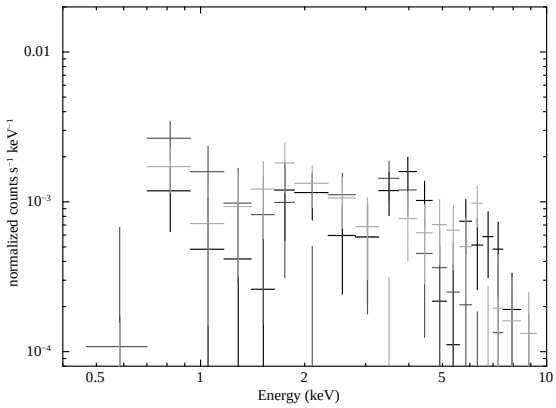

Figure 4.14: XIS spectra of Src A. Black, Dark Gray and Light Gray lines represent the data for the XIS0, XIS1 and XIS3, respectively.

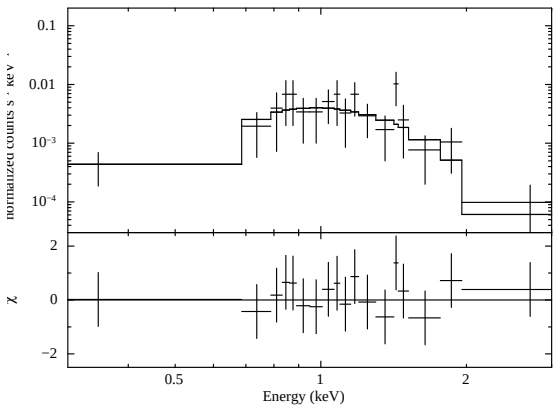

Figure 4.15: Combined Chandra spectrum of three point sources (Srcs 1, 2 and 3). Black lines represent the best-fit model.

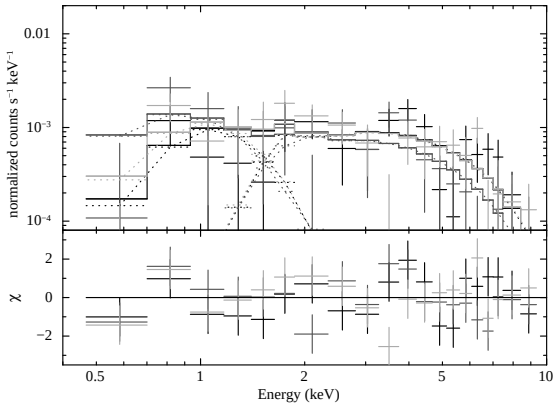

Figure 4.16: XIS spectra of Src A. Black, Dark Gray and Light Gray lines represent the data and model for the XIS0, XIS1 and XIS3, respectively. The contribution of Chandra point sources is indicated by the dotted lines in the soft-band. The additional dotted lines in the hard-band show the diffuse component.

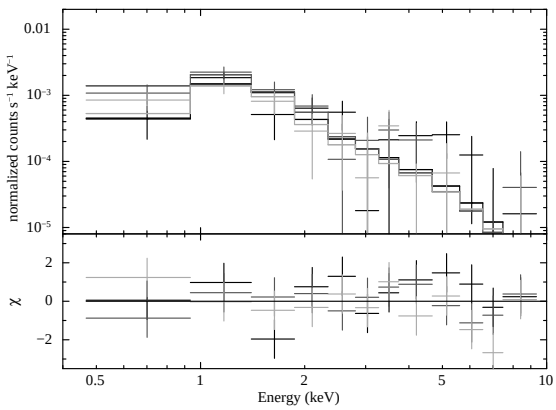

Figure 4.17: XIS spectra of Src B. Black, Dark Gray and Light Gray lines represent the data and model for the XIS0, XIS1 and XIS3, respectively.

Intensity upper limit of PSR J1648−4611

Since the X-ray emission of PSR J1648−4611 was not detected by the point source search for the Chandra image, we estimated the intensity upper limit using the Chandra data as follows. The event number in the 0.4–10 keV band in a circular region with a radius of 3″ centered on the pulsar is 3 counts. We set the source region larger than the point spread function of Chandra to include the possible extended emission from a compact PWN (Kargaltsev et al., 2012). A background was estimated using an annular region with an inner radius of 2′ and an outer radius of 3′, which was outside of the Suzaku Src A region, and the background event number in the 0.4–10keV band was 1300; the event number normalized to the source region was 0.65 counts. The event number in the source region after subtracting the background was estimated to be $2.35^{+3.01}_{-2.05}$ counts by a numerical simulation assuming the Poisson statistics; since the 99% confidence range was estimated to be $2.35^{+4.01}_{-3.02}$ counts and was consistent with zero, we conservatively think that the X-rays from the pulsar is not statistically significant. The upper limit on the pulsar X-rays in the 0.4–10 keV band at the 90% confidence level was thus 5.4 counts. The count number was converted to the energy flux in the 0.4–10 keV band by using webPIMMS[13] assuming a power-law model with $\Gamma = 2$ and a hydrogen column of $N_{\rm H} = 2 \times 10^{22}$ cm^{-2} where we adopted the total Galactic HI column density towards PSR J1648−4611 (Dickey & Lockman, 1990). The upper limit on the X-ray flux of PSR J1648−4611 in the 0.4–10 keV band was thus calculated to be 1.0×10^{-14} erg s^{-1} cm^{-2}, while that on the unabsorbed flux was 2.3×10^{-14} erg s^{-1} cm^{-2}.

4.2.4 Discussion

X-ray emission from PSR J1648−4611

The X-ray emission from the pulsar PSR J1648−4611 was not detected in the Chandra image. The upper limit on the flux of PSR J1648−4611 yields the upper limit on the luminosity of 8.8 $d_{5.7}^2 \times 10^{31}$ erg s^{-1} in the 0.4–10.0 keV band, where $d_{5.7}$ is the distance scaled to 5.7 kpc.

Kargaltsev et al. (2012) also analyzed the same Chandra data and detected no X-rays from the pulsar. Their upper limit on the X-ray count in the 0.4–10 keV band in the circular region with a radius of 3″ is, however, 3.1 counts, which we converted from their upper limit on the X-ray flux in the 0.5–8 keV band (5.2×10^{-15}erg s^{-1} cm^{-2}) using their assumed model (a power-law model of $\Gamma = 1.5$ and $N_{\rm H} = 1.2 \times 10^{22}$ cm^{-2}). This value is only ∼60% of our estimate. The main reason for the discrepancy is the difference of the methods for the upper limit; Kargaltsev et al. (2012) estimated the upper limit only from the background event number, while we obtained it using both the source and background event numbers. Our value is conservative anyway.

The upper limit on the X-ray luminosity in the 0.1–2.4 keV band is 8.7 $d_{5.7}^2 \times 10^{31}$ erg s^{-1}. Following the relation between the spin-down power and X-ray luminosity of rotation-powered pulsars (Becker & Trümper, 1997), the expected X-ray luminosity of PSR J1648−4611

[13] http://heasarc.gsfc.nasa.gov/Tools/w3pimms.html

in the 0.1–2.4 keV band would be $L_{\rm X} \sim 10^{32}$ erg s^{-1}. This value is consistent with our upper limit. Since pulsed GeV emission with the rotation period of PSR J1648−4611 is observed with the Fermi satellite,[14] it is natural to expect an X-ray emission of the pulsar. However, even if PSR J1648−4611 would have X-ray emission with the luminosity expected from the spin-down luminosity, we would not be able to detect it with the short exposure time (∼10 ks) because of the heavy extinction due to the Galactic plane and of the distance.

Diffuse hard X-ray emission from Src A

We found the diffuse hard X-ray emission from Src A in the Suzaku image. The peak position of the emission is close to PSR J1648−4611. A natural interpretation is that the diffuse hard X-ray emission comes from a PWN around PSR J1648−4611. The photon index of the hard X-ray emission is $2.0^{+0.9}_{-0.7}$. This value is consistent with the typical values of PWNe (Fleishman & Bietenholz, 2007 and references therein). The column density $N_{\rm H} = 3.4^{+2.4}_{-1.6} \times 10^{22}$ cm^{-2} is also consistent with the Galactic HI column density towards PSR J1648−4611 ($\sim 2 \times 10^{22}$ cm^{-2}; Dickey & Lockman, 1990). Furthermore, a constant component in the GeV emission is reported (Abramowski et al., 2012), and the component also suggests the existence of the PWN.

On the other hand, the luminosity of the diffuse hard X-ray emission is 7.3 $d_{5.7} \times 10^{32}$ erg s^{-1} in the 2–10 keV band. Following the relation between spin-down power/characteristic age and X-ray luminosity of PWNe (Mattana et al., 2009), the expected X-ray luminosity of the associated PWN would be $L_{\rm X} \sim 10^{31}$ erg s^{-1}. Thus our result is much larger than the expected luminosity, even when the uncertainty in the distance estimation of $\sim$ 30% (Kramer et al., 2003) is taken into account. Furthermore we obtained the lower limit on the ratio of the PWN to pulsar luminosities $L_{\rm PWN(0.5-8keV)}/L_{\rm PSR(0.5-8keV)} \geq 16$. This value is larger than the average $L_{\rm PWN(0.5-8keV)}/L_{\rm PSR(0.5-8keV)} \sim 4$ reported by Kargaltsev et al. (2007). Additionally, the physical size of the diffuse X-ray emission is $\sim 3.3\ d_{5.7}(\theta/2')$pc, where θ is the angular radius of Src A. This size is an order of magnitude smaller than the expected value based on the PWN size-age relation reported by Bamba et al. (2010). Therefore if the diffuse hard X-ray emission is the PWN of PSR J1648−4611, it is much brighter than that expected from the spin-down luminosity of the pulsar, and the spatial extension is rather compact.

Connection to HESS J1646-458

If the origin of the TeV emission from HESS J1646−458 is PSR J1648−4611, an unreasonably high efficiency of $\epsilon_\gamma = L_\gamma/\dot{E} = 96\ d_{5.7}^2\%$ is required for the production of TeV flux of HESS J1646−458, which is 5.2×10^{-11} cm^{-2} s^{-1} above 0.2 TeV (Abramowski et al., 2012). Additionally, the observed VHE γ-ray emitting region has a diameter of about 2°, which is a factor of $\sim$ 30 larger than that of the X-ray emitting region of Src A and is not consistent with the ratio between the predicted VHE γ-ray and X-ray size of PWN (~ 6 :

[14] See ⟨https://confluence.slac.stanford.edu/display/GLAMCOG/Public+List+of+LAT-Detected+Gamma-Ray+Pulsars⟩.

Aharonian et al., 2005d). These results imply that HESS J1646−458 seems unlikely to be explained only as a PWN powered by PSR J1648−4611. However, it is conceivable that parts of the VHE γ-ray emission of HESS J1646−458 are powered by the pulsar.

4.2.5 Summary

We observed the pulsar PSR J1648−4611 with Suzaku, and discovered the diffuse hard X-ray emission around PSR J1648−4611. The spatial distribution and the photon index of the diffuse emission suggest that a PWN exists around the pulsar. The luminosity of the diffuse emission, however, is much larger than that expected from the spin-down luminosity of the pulsar. Parts of the VHE γ-ray emission of HESS J1646−458 could be caused by this PWN powered by PSR J1648−4611.

Chapter 5

Analysis of the other unidentified VHE γ-ray sources

In this chapter, we have analyzed the X-ray data of the other unidentified VHE γ-ray sources to quantify their common properties, especially we focused on the presence or absence of the possible counterpart in the hard-energy band.

Here, we selected 8 sources according to the criteria described below. First, we selected sources which are categorized as "UNID: unidentified source"(28), "DARK: dark accelerator (same as UNID)"(1) and "Massive Star Cluster"(4) in the online catalog for TeV Astronomy (TeVCat:http://tevcat.uchicago.edu/). Since most of the criteria for identification as a massive star cluster include a positional coincidence such as HESS J1614−518, we included "Massive Star Cluster". Second, we removed 10 sources which do not have sufficient positional and spectral information in the VHE γ-ray band. Then the number of selected sources were 23. Among them, except for HESS J1614−518 and HESS J1646−458, 8 sources have the X-ray data which have not yet been published, thus we analyzed in this chapter.

When we analyzed the X-ray data, we concentrated on the hard-energy band because X-ray sources found in the soft-energy band are likely to be foreground sources. In particular, for the Suzaku data, we focused on the X-ray sources found in the hard-energy band. For the XMM-Newton and Chandra data, if the best-fit position of the VHE γ-ray emission is located within the field of view, we focused on the X-ray sources found near the best-fit position. If not, we focused on diffuse X-ray emission because most X-ray sources related to VHE γ-ray sources are extended. When we found such X-ray sources, we investigated their spatial, temporal and spectral properties.

5.1 HESS J1503−582

5.1.1 Overview

The VHE γ-ray emitter HESS J1503−582 (shown in figure 5.1 (left)) has been recently discovered by H.E.S.S. (Renaud et al., 2008a), and it is still unidentified, i.e. it did not

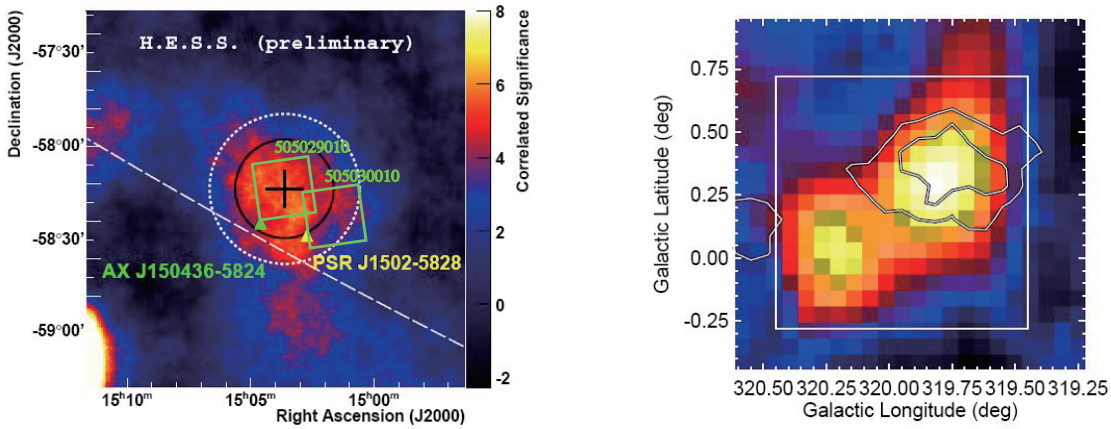

Figure 5.1: Left: γ-ray image of HESS J1503−582. The black cross and circle denote the uncertainty of the source centroid and its intrinsic size, respectively. The Galactic Plane is shown as the dashed line. The bright source in the lower left corner is MSH 15−52. Green squares represent the Suzaku/XIS field of views. Right: SGPS (Parkes) image of the HI line emission centered on FVW 319.8+0.3, velocity-integrated between −123 and −98 km/s. H.E.S.S. significance contours are shown as 4 and 5σ levels. Note that the image is in Galactic coordinates. (Both figures adapted from Renaud et al. (2008a).)

have any of the typical counterparts at lower energies (e.g. SNRs, energetic pulsars, or bright Fermi LAT sources). However, it is now considered unique in that it is the first VHE γ-ray source that appears to be associated with a forbidden-velocity wing (FVW). FVWs are faint HI 21 cm emission line structures which are visible at velocities which deviate from the canonical Galactic rotation curve, suggesting associated dynamical phenomena (Kang & Koo, 2007), as shown in figure 5.1 (right).

HESS J1503−582, visible in figure 5.1 (left), shows significance of $\sim 6\sigma$ in ~ 24 hours of effective exposure. The spectrum can be fit well by a power law with index $\Gamma = 2.4 \pm 0.4_{\rm stat} \pm 0.2_{\rm syst}$ with a flux above 1 TeV of $\sim 6 \times 10^{-12}{\rm cm}^{-2}\ {\rm s}^{-1}$ ($\sim 6\%$ of the Crab flux).

5.1.2 Observations

Suzaku observed HESS J1503−582 in August, 2010. Suzaku also observed one nearby position (BGD). Three XISs (XIS 0, 1, 3) were operated in the normal clocking mode with the Spaced-row Charge Injection (SCI) (Uchiyama et al., 2009b). We analyzed the data prepared by the version 2.5 pipeline. We concentrated on the analysis of the XIS data because we were interested in the spatial distribution of the emission. We applied the standard screening criteria to the XIS[1] data to obtain cleaned event lists. After the data screening, the net exposures were 51.4 ks and 51.6 ks for the HESS J1503−582 and BGD regions, respectively. The journal of these observations are summarized in table 5.1. We used HEADAS version 6.11.1 software package for the data analysis of HESS

[1] ⟨http://www.astro.isas.jaxa.jp/suzaku/process/v2changes/criteria_xis.html⟩.

J1503−582.

Table 5.1: Journal of the Suzaku observations of HESS J1503−582.

Satellite	Suzaku	Suzaku
Sequence ID	505029010	505030010
Start time (UT)[1]	2010/08/05 03:45	2010/08/05 22:21
End time (UT)[1]	2010/08/05 22:20	2010/08/06 16:08
Aim point R.A. (J2000.0)	225°.9130	225°.4141
Aim point Decl. (J2000.0)	−58°.2332	−58°.3766
Net exposure (ks)	51.4	51.6

[1] Time form of yyyy/mm/dd hh:mm.

5.1.3 Analysis and Results

XIS Image

We extracted XIS images from each FI sensor using the screened data for the soft- (0.4–3 keV) and hard- (3–10 keV) energy bands. We excluded the corners of the CCD chips illuminated by the ^{55}Fe calibration sources. The images of the non-X-ray background (NXB) were generated using `xisnxbgen` (Tawa et al., 2008) and subtracted from the images. Then, the soft- and hard-band images were divided by flat sky images simulated at 1.49 and 4.5 keV using the XRT+XIS simulator `xissim` (Ishisaki et al., 2007) for vignetting corrections. Finally, the images from the two FI sensors were summed and binned by a factor of 8.

The XIS FI images of the HESS J1503−582 region (HESS J1503−582 and BGD) smoothed using a Gaussian function with $\sigma = 0'.28$ is shown in figure 5.2. In the hard-band image, three X-ray sources (Src1, Src2 and Src3 in figure 5.2 (right)) were found. Src3 is also conspicuous in the soft-band image (figure 5.2 (left)). The coordinates are summarized in table 5.2.

We also examined the radial profiles in the 3–10 keV band. The profiles are consistent with the PSF plus a constant component model, supporting the assumption of point sources.

Table 5.2: X-ray sources in HESS J1503−582.

Source name	l (deg)	b (deg)	R.A. (deg)	Decl. (deg)
Src1	319.69	0.37	225.96	−58.13
Src2	319.53	0.24	225.82	−58.32
Src3	319.42	0.26	225.61	−58.35

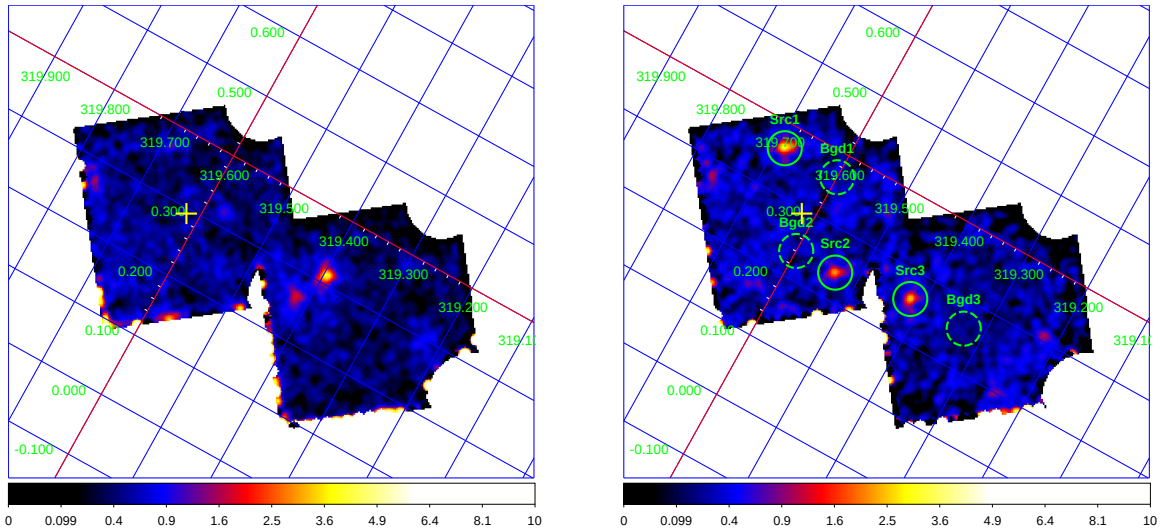

Figure 5.2: Suzaku XIS FI (XIS 0+3) images of the HESS J1503−582 region (HESS J1503−582 and BGD) in the Galactic coordinates: (left) 0.4–3 keV and (right) 3–10 keV bands. The images were smoothed using a Gaussian function with $\sigma = 0'.21$. A vignetting correction was applied after subtracting the NXB, as described in the text. The yellow cross indicates the best-fit position of the TeV γ-ray emission. The solid circles indicate the integration regions of source photons, and the dashed circles are that of background photons.

XIS Spectrum

There are three X-ray sources (Src1, Src2 and Src3 in figure 5.2 (right)) in the hard-band image. We also examined the light curves of the sources in the hard-energy band from these regions and found no significant time variability from them. Then, we investigated the spectra of these sources. The source and background regions for each source are described in figure 5.2 (right). The background-subtracted spectra of each source with the best-fit model are shown in figure 5.3. The best-fit parameters and the fluxes are listed in table 5.3.

Table 5.3: Best-fit results of the X-ray spectra in HESS J1503−582.[1]

	Src1	Src2	Src3
Model[2]	PL	PL	PL
$N_{\rm H}$ (10^{22} cm^{-2})	$0.5^{+1.6}_{-0.5}$	$21.0^{+27.7}_{-18.7}$	$0.9^{+0.6}_{-0.5}$
Γ	$0.3^{+0.6}_{-0.5}$	$1.9^{+5.4}_{-2.5}$	$1.9^{+0.5}_{-0.4}$
$F^{\rm obs}_{2-10{\rm keV}}$[3]	3.1	1.5	1.8
$F^{\rm abscor}_{2-10{\rm keV}}$[4]	3.1	3.8	1.9
χ^2/d.o.f.	31.13/27	16.31/24	25.30/31

[1] Errors are at the 90% confidence level.
[2] Model used for the spectral fitting: "PL" is a power-law model.
[3] Observed flux in the 2–10 keV band in units of 10^{-13} erg cm^{-2} s^{-1}.
[4] Absorption corrected flux in the 2–10 keV band in units of 10^{-13} erg cm^{-2} s^{-1}.

Although no counterparts are found in literatures, the X-ray spectrum of Src2 with an absorption column density of $N_{\rm H} \sim 10^{23}$ cm^{-2} indicates an extragalactic source because that is much larger than the Galactic absorption determined by the HI emission ($\sim 1.7 \times 10^{22}$ cm^{-2}; Dickey & Lockman, 1990), and the photon index $\Gamma \sim 2$ may suggest active galactic nucleus (AGN).

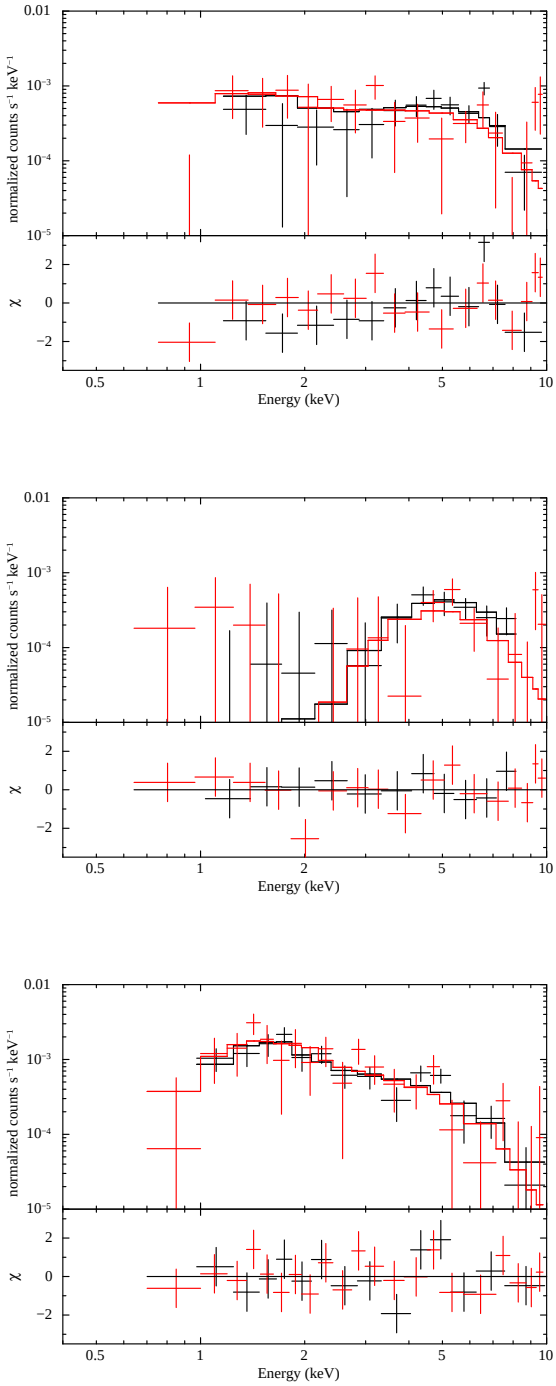

Figure 5.3: XIS spectra of Src1 (top), Src2 (middle) and Src3 (bottom) in HESS J1503−582, shown with the best-fit model. Black and red lines represent the data and model for the XIS FI (XIS0+3) and XIS BI (XIS1), respectively.

5.2 HESS J1507−622

5.2.1 Overview

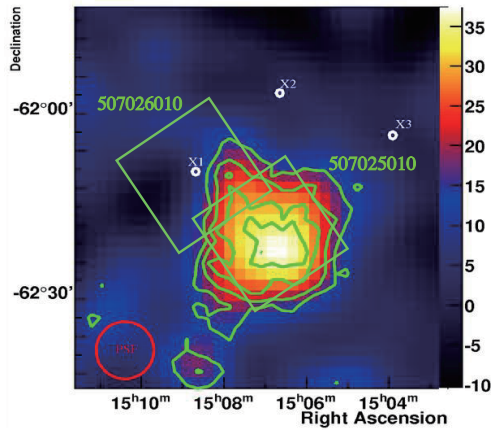

Figure 5.4: Smoothed γ-ray count map of HESS J1507−622 (H.E.S.S. Collaboration et al., 2011a). The green contours show 3, 4, 5 and 6σ significance. White circles indicate three faint ROSAT X-ray sources (Voges et al., 2000):X1 indicates 1RXS J150841.2−621006, X2 indicates 1RXS J150639.1−615704 and X3 indicates 1RXS J150354.7−620408. Green squares represent the Suzaku/XIS field of views.

HESS J1507−622 (shown in figure 5.4) is one of the most interesting newly discovered sources (Chaves et al., 2009). HESS J1507−622 is among the brightest ($\sim$ 8% of Crab Flux) newly discovered sources and it is so far without plausible counterparts. While all unidentified VHE sources that have been discovered in the H.E.S.S. Galactic Plane Survey so far are located in a quite narrow angular band of $\pm 1°$ around the Galactic plane, HESS J1507−622 is unique in this respect since it lies $\sim$ 3°.5 offset from the Galactic plane. If truly offset from the plane and not simply a nearby source, it would be even more surprising to not find any trace of counterparts, considering the comparably lower $n_{\rm H}$ at 3°.5 off the plane and, hence, the lower Galactic absorption in X-rays and the reduced background emission. The discovery peak significance is 9.3σ. Figure 5.4 shows the excess count map (smoothed with Gaussian of 0°.07). The best fit position is at RA = 226°.72 ± 0°.05, Dec = −62°.35 ± 0°.03, and the source is slightly extended with an intrinsic size of 0°.15.

H.E.S.S. Collaboration et al. (2011a) discovered eleven point-like sources (mainly identified as stars) and one extended source by the Chandra observation of HESS J1507−622. The extended source is spatially coincident with the radio source MGPS J150850−621025 (Green et al., 1999), and is compatible with the X-ray source 1RXS J150841.2−621006 (Voges et al., 2000) when considering the well known systematics in the positional accuracy of 30″ of ROSAT (Harris et al., 1998). The flux of this source is $(7.0\pm0.7)\times10^{-13}$ erg cm^{-2} s^{-1} in the 2–10 keV band. However, they mentioned that the extended source is not a plau-

sible counterpart for HESS J1507−622, because the source is located outside of the 3σ significance contour. H.E.S.S. Collaboration et al. (2011a) also found a faint extended source. The flux of this source is $(1.1^{+0.3}_{-0.5}) \times 10^{-13}$ erg cm^{-2} s^{-1} in the 2–10 keV band. However, it has to be noted that an association can not be established with Chandra data.

5.2.2 Observations

Suzaku observed HESS J1507−622 in September, 2012. Suzaku also observed one nearby position (BGD). Three XISs (XIS 0, 1, 3) were operated in the normal clocking mode with the Spaced-row Charge Injection (SCI) (Uchiyama et al., 2009b). We analyzed the data prepared by the version 2.8 pipeline. We concentrated on the analysis of the XIS data because we were interested in the spatial distribution of the emission. We applied the standard screening criteria to the XIS[2] data to obtain cleaned event lists. After the data screening, the net exposures were 79.9 ks and 40.9 ks for the HESS J1507−622 and BGD regions, respectively. The journal of these observations are summarized in table 5.4. We used HEADAS version 6.11.1 software package for the data analysis of HESS J1507−622.

Table 5.4: Journal of the Suzaku observations of HESS J1507−622.

Satellite	Suzaku	Suzaku
Sequence ID	507025010	507026010
Start time (UT)[1]	2012/09/11 11:42	2012/09/13 22:56
End time (UT)[1]	2012/09/13 22:55	2012/09/15 02:30
Aim point R.A. (J2000.0)	226°.7316	227°.1815
Aim point Decl. (J2000.0)	−62°.3464	−62°.1646
Net exposure (ks)	79.9	40.9

[1] Time form of yyyy/mm/dd hh:mm.

5.2.3 Analysis and Results

XIS Image

We extracted XIS images from each FI sensor using the screened data for the soft- (0.4–3 keV) and hard- (3–10 keV) energy bands. We excluded the corners of the CCD chips illuminated by the ^{55}Fe calibration sources. The images of the non-X-ray background (NXB) were generated using `xisnxbgen` (Tawa et al., 2008) and subtracted from the images. Then, the soft- and hard-band images were divided by flat sky images simulated at 1.49 and 4.5 keV using the XRT+XIS simulator `xissim` (Ishisaki et al., 2007) for vignetting corrections. Finally, the images from the two FI sensors were summed and binned by a factor of 8.

[2] ⟨http://www.astro.isas.jaxa.jp/suzaku/process/v2changes/criteria_xis.html⟩.

The XIS FI images of the HESS J1507−622 region (HESS J1507−622 and BGD) smoothed using a Gaussian function with $\sigma = 0'.28$ is shown in figure 5.5. In the hard-band image, two X-ray sources (Src1 and Src2 in figure 5.5 (right)) in the literature were found (H.E.S.S. Collaboration et al., 2011a), and the other sources were mainly identified as stars. Src2 is also conspicuous in the soft-band image (figure 5.5 (left)). The coordinates above two sources are summarized in table 5.5. Table 5.6 shows possible counterpart of X-ray sources from the SIMBAD Astronomical Database.

According to H.E.S.S. Collaboration et al. (2011a), CXOU J150850.6−621018 is extended (35–40″). Then, we compared a radial profile of Src2 with a point-spread function (PSF) of Suzaku obtained from the radial profile of the SS Cyg data observed on 2005 November 2 (OBSID=400006010). The origin of the radial profile was the peak in the hard-band image. Note that the NXB subtraction and vignetting correction were not applied to both the radial profiles of Src2 and the PSF. Figure 5.6 shows the radial profile of Src2 in the 3–10 keV band. The profile cannot be fitted adequately with the PSF plus a constant component model ($\chi^2/d.o.f. = 249.4/48$), and therefore Src2 must be extended or unresolved multiple sources.

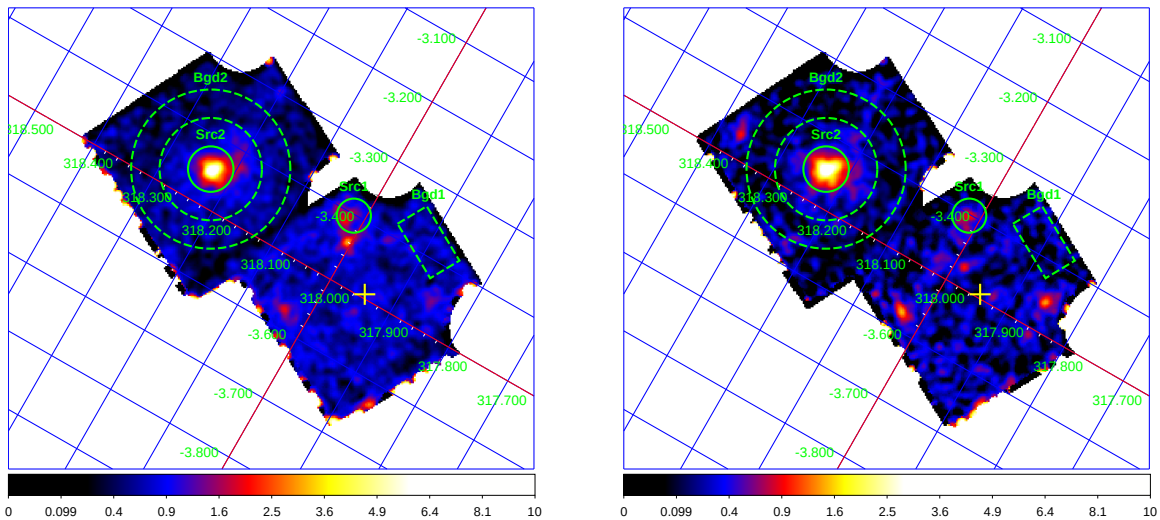

Figure 5.5: Suzaku XIS FI (XIS 0+3) images of the HESS J1507−622 region (HESS J1507−622 and BGD) in the Galactic coordinates: (left) 0.4–3 keV and (right) 3–10 keV bands. The images were smoothed using a Gaussian function with $\sigma = 0'.21$. A vignetting correction was applied after subtracting the NXB, as described in the text. The yellow cross indicates the best-fit position of the TeV γ-ray emission. The solid circles indicate the integration regions of source photons, and the regions bounded by a dashed line are those of background photons.

XIS Spectrum

We investigated the spectra of above two X-ray sources (Src1 and Src2 in figure 5.5 (right)). The source and background regions for each source are described in figure 5.5

Table 5.5: X-ray sources in HESS J1507−622.

Source name	l (deg)	b (deg)	R.A. (deg)	Decl. (deg)
Src1	318.02	−3.40	226.75	−62.23
Src2	318.23	−3.45	227.20	−62.17

Table 5.6: Possible counterpart of X-ray sources of HESS J1507−622.

Source name	R.A. (deg)	Decl. (deg)	MAIN_ID	OTYPE[1]
Src2	227.171679	-62.168469	1RXS J150841.2−621006	X
	227.20912	-62.17375	MGPS J150850−621025	Radio
	227.210987	-62.171733	CXOU J150850.6−621018	X

[1] Object type.

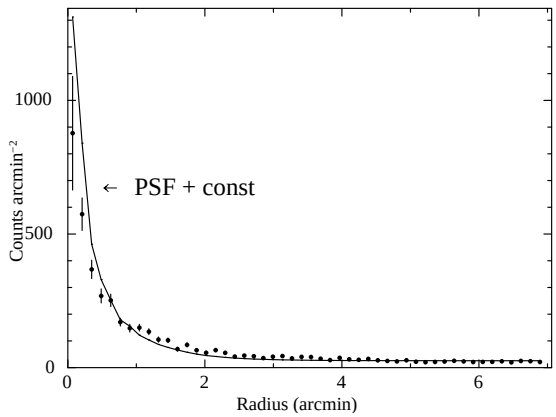

Figure 5.6: Radial profile of Src2 extracted from the 3–10 keV band image of the XIS FI sensor (XIS 0+3). The solid line represents the XIS PSF profile with a constant component.

(right). The background-subtracted spectra of each source with the best-fit model are shown in figure 5.7. The best-fit parameters and the fluxes are listed in table 5.7. We also examined the light curves of the sources in the hard-energy band from these regions and found no significant time variability from them.

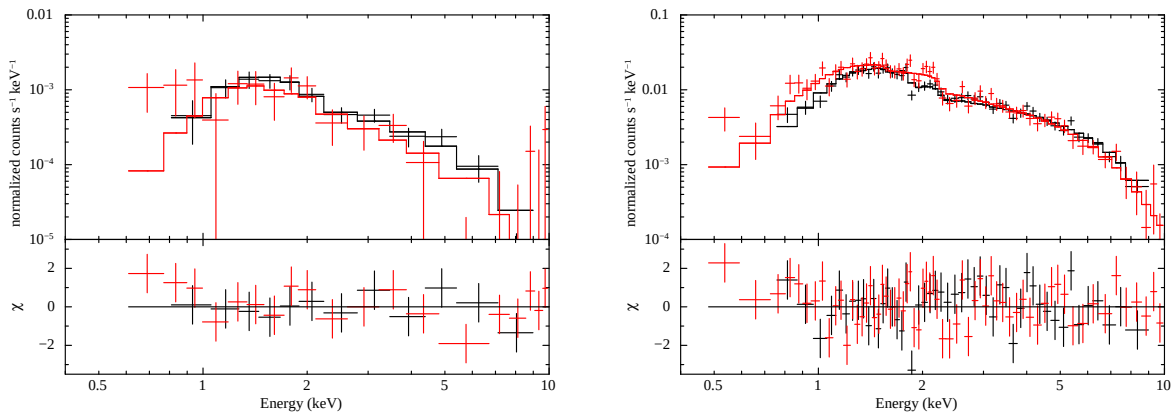

Figure 5.7: XIS spectra of Src1 (left) and Src2 (right) in HESS J1507−622, shown with the best-fit model. Black and red lines represent the data and model for the XIS FI (XIS0+3) and XIS BI (XIS1), respectively.

Table 5.7: Best-fit results of the X-ray spectra in HESS J1507−622.[1]

	Src1	Src2
Model[2]	PL	PL
$N_{\rm H}$ (10^{22} cm^{-2})	$0.8^{+0.6}_{-0.4}$	$0.5^{+0.1}_{-0.1}$
Γ	$2.4^{+0.6}_{-0.4}$	$1.8^{+0.1}_{-0.1}$
$F^{\rm obs}_{2-10{\rm keV}}$[3]	0.8	9.7
$F^{\rm abscor}_{2-10{\rm keV}}$[4]	0.9	10.2
χ^2/d.o.f.	19.83/27	114.93/109

[1] Errors are at the 90% confidence level.
[2] Model used for the spectral fitting: "PL" is a power-law model.
[3] Observed flux in the 2–10 keV band in units of 10^{-13} erg cm^{-2} s^{-1}.
[4] Absorption corrected flux in the 2–10 keV band in units of 10^{-13} erg cm^{-2} s^{-1}.

The X-ray flux of Src1 is compatible with that of Chandra. Therefore, Src1 might be a stable source. On the other hand, the extended nature and the X-ray spectrum of Src2 implies emission from PWN, but there is no pulsar emission detected so far.

5.3 HESS J1841−055

5.3.1 Overview

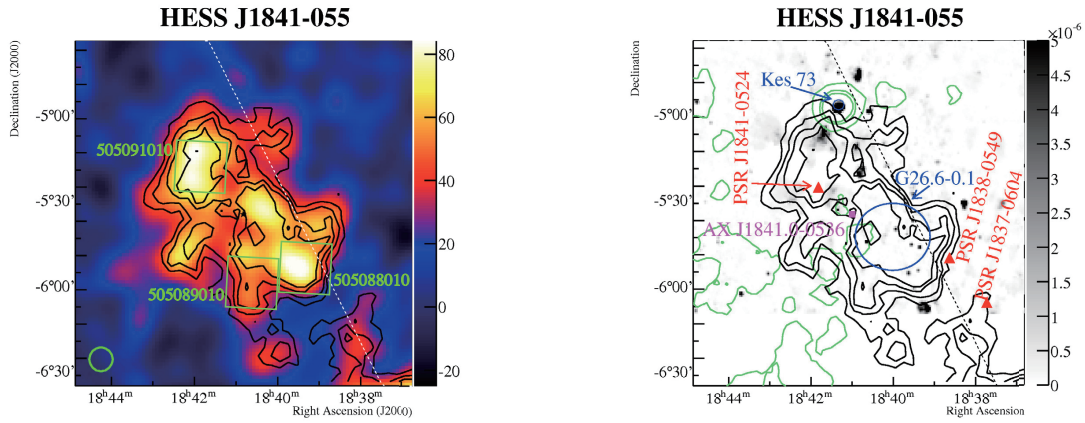

Figure 5.8: Left: γ-ray image of HESS J1841−055. The dotted line indicates the Galactic plane. Green squares represent the Suzaku/XIS field of views. Right: View of the region around HESS J1841−055 in other wavelength: H.E.S.S. significance contours (black) and adaptively smoothed ROSAT X-ray contours (green), overlaid on a NVSS radio image (grey-scale). Also shown are the positions of known high spin-down flux pulsars (filled triangles), the SNR Kes 73 (circle), the X-ray candidate SNR G26.6−0.1 (blue circle), and the HMXB AX J1841.0+0536. The Ginga source GS 1839-06 is compatible with the location of AX J1841.0+0536. (Both figures adapted from Aharonian et al. (2008b).)

HESS J1841−055 (Aharonian et al., 2008b) exhibits a highly extended, possibly two or three-peaked, morphology; however, the "dip" between the peaks along the major axis is not statistically significant ($< 1.5\sigma$). The source has a spectrum that is fit by a power law with index $2.4 \pm 0.1_{\rm stat} \pm 0.2_{\rm sys}$. An association with either pulsar PSR J1841−0524 or PSR J1838−0549, is not ruled out, however taken separately, each would require approximately 200% efficiency to explain the VHE emission. PSR J1837−0604 has a high enough spin-down flux to be a counterpart candidate, however it is well outside the emission region. There are no cataloged PWN at longer wavelengths identified with any of the three pulsars. The SNR G027.4+00.0 (also known as Kes 73), which is visible in both X-ray and radio wave bands, lies at the edge of the emission, though does not appear related due to its small angular size. Additionally, the high-mass X-ray binary also lies near the edge of the significant TeV excess.

5.3.2 Observations

Suzaku observed four regions of HESS J1841−055 in March, 2011. One of the regions, covered the HMXB AX J1841.0+0536, was recently analyzed and published (Kawabata et al., 2012). Then, we concentrated on the other three regions of HESS J1841−055. Three XISs (XIS 0, 1, 3) were operated in the normal clocking mode with the Spaced-row

Charge Injection (SCI) (Uchiyama et al., 2009b). We analyzed the data prepared by the version 2.5 pipeline. We concentrated on the analysis of the XIS data because we were interested in the spatial distribution of the emission. We applied the standard screening criteria to the XIS[3] data to obtain cleaned event lists. After the data screening, the net exposures were 49.7 ks, 50.0 ks and 51.2 ks for the three regions of HESS J1841−055, respectively. The journal of these observations are summarized in table 5.8. We used HEADAS version 6.11.1 software package for the data analysis of HESS J1841−055.

Table 5.8: Journal of the Suzaku observations of HESS J1841−055.

Satellite	Suzaku	Suzaku	Suzaku
Sequence ID	505088010	505089010	505091010
Start time (UT)[1]	2011/03/25 07:00	2011/03/26 10:41	2011/03/28 19:01
End time (UT)[1]	2011/03/26 10:40	2011/03/27 15:20	2011/03/29 23:07
Aim point R.A. (J2000.0)	279°.8307	280°.1473	280°.4555
Aim point Decl. (J2000.0)	−5°.8897	−5°.9564	−5°.2917
Net exposure (ks)	49.7	50.0	51.2

[1] Time form of yyyy/mm/dd hh:mm.

5.3.3 Analysis and Results

XIS Image

We extracted XIS images from each FI sensor using the screened data for the soft- (0.4–3 keV) and hard- (3–10 keV) energy bands. We excluded the corners of the CCD chips illuminated by the ^{55}Fe calibration sources. The images of the non-X-ray background (NXB) were generated using `xisnxbgen` (Tawa et al., 2008) and subtracted from the images. Then, the soft- and hard-band images were divided by flat sky images simulated at 1.49 and 4.5 keV using the XRT+XIS simulator `xissim` (Ishisaki et al., 2007) for vignetting corrections. Finally, the images from the two FI sensors were summed and binned by a factor of 8.

The XIS FI images of the HESS J1841−055 region smoothed using a Gaussian function with $\sigma = 0'.28$ is shown in figure 5.9. In the hard-band image, four conspicuous X-ray sources (Src1, Src2, Src3 and Src4 in figure 5.9 (right)) were found. Src1 is also conspicuous in the soft-band image (figure 5.9 (left)). The coordinates are summarized in table 5.9. Table 5.10 shows possible counterpart of X-ray sources from the SIMBAD Astronomical Database.

We also examined the radial profiles in the 3–10 keV band. The profiles are consistent with the PSF plus a constant component model, supporting the assumption of point sources.

[3] ⟨http://www.astro.isas.jaxa.jp/suzaku/process/v2changes/criteria_xis.html⟩.

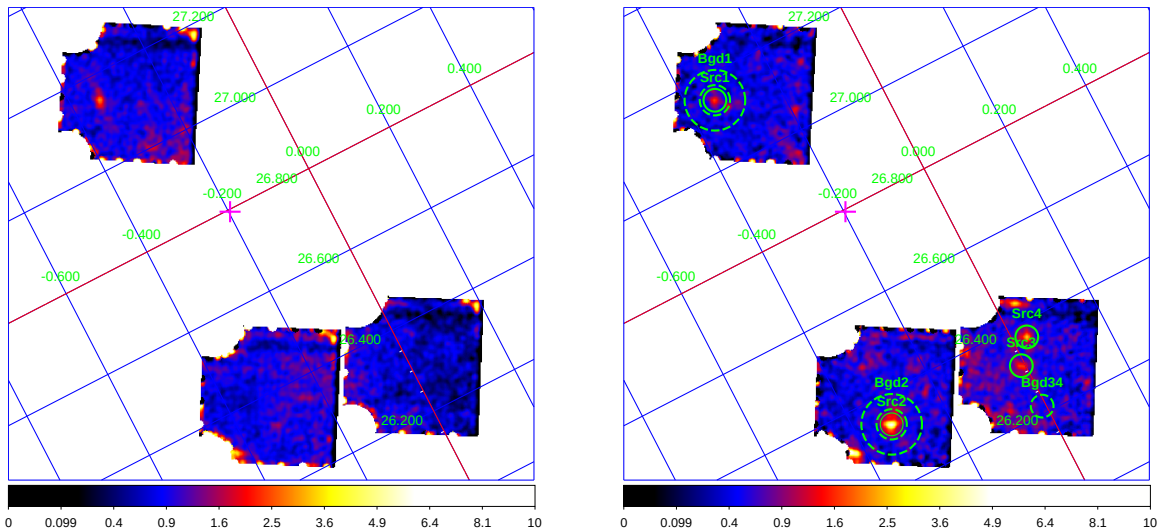

Figure 5.9: Suzaku XIS FI (XIS 0+3) images of the HESS J1841−055 region in the Galactic coordinates: (left) 0.4–3 keV and (right) 3–10 keV bands. The images were smoothed using a Gaussian function with $\sigma = 0'.21$. A vignetting correction was applied after subtracting the NXB, as described in the text. The magenta cross indicates the best-fit position of the TeV γ-ray emission. The solid circles indicate the integration regions of source photons, and the regions bounded by a dashed line are those of background photons.

Table 5.9: X-ray sources in HESS J1841−055.

Source name	l (deg)	b (deg)	R.A. (deg)	Decl. (deg)
Src1	27.14	−0.34	280.52	−5.31
Src2	26.33	−0.32	280.13	−6.02
Src3	26.32	−0.01	279.84	−5.89
Src4	26.37	0.03	279.83	−5.83

Table 5.10: Possible counterpart of X-ray sources of HESS J1841−055.

Source name	R.A. (deg)	Decl. (deg)	MAIN_ID	OTYPE[1]
Src3	279.845860	-05.888870	2MASS J18392300−0553199	Star

[1] Object type.

XIS Spectrum

There are four conspicuous X-ray sources (Src1, Src2, Src3 and Src4 in figure 5.9 (right)) in the hard-band image. We also examined the light curves of the sources in the hard-energy band from these regions and found no significant time variability except for Src2. The best-fit χ^2/d.o.f. values of 132.0/77 (XIS 0), 93.90/74 (XIS 1), and 124.3/78 (XIS 3) were obtained by fitting the light curve of Src2 with a constant model. Then, we investigated the spectra of these sources. The source and background regions for each source are described in figure 5.9 (right). The background-subtracted spectra of each source with the best-fit model are shown in figure 5.10. The best-fit parameters and the fluxes are listed in table 5.11.

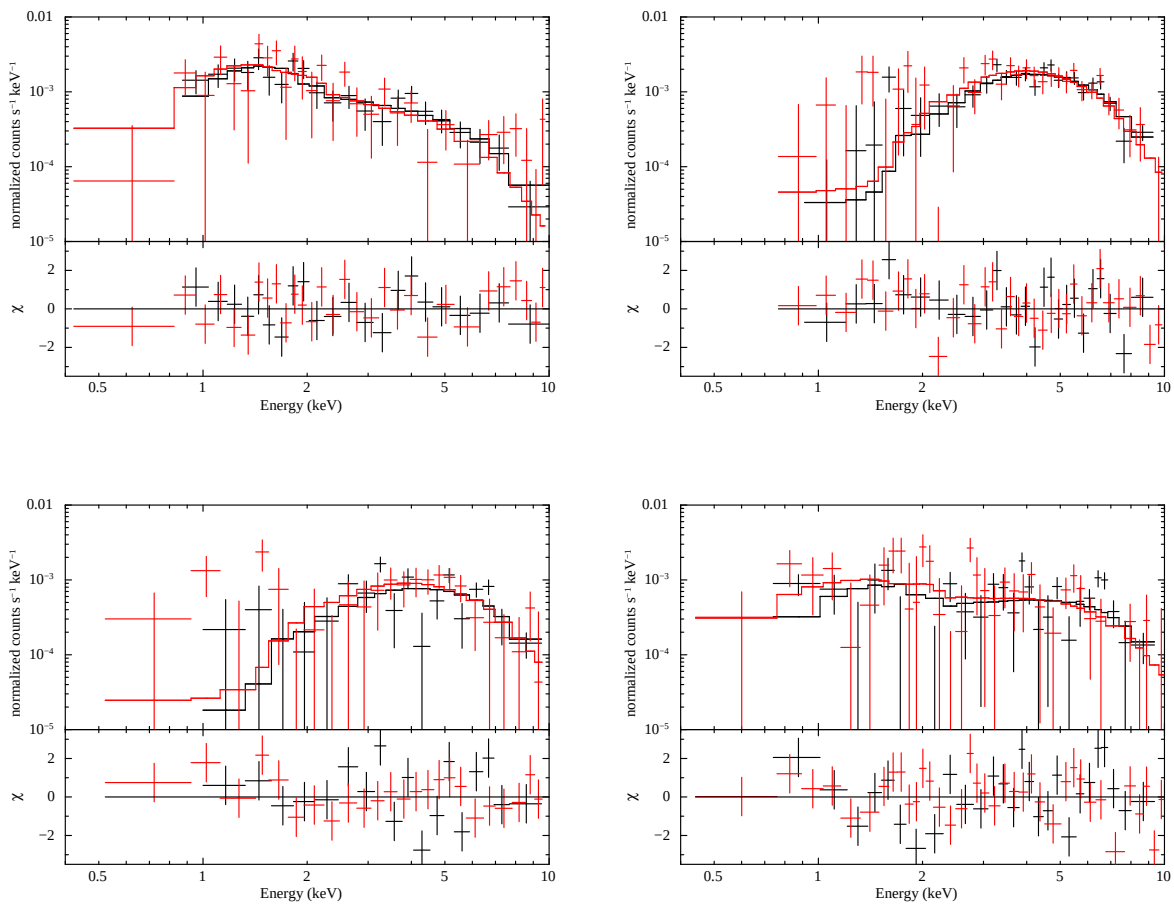

Figure 5.10: XIS spectra of Src1 (top-left), Src2 (top-right), Src3 (bottom-left) and Src4 (bottom-right) in HESS J1841−055, shown with the best-fit model. Black and red lines represent the data and model for the XIS FI (XIS0+3) and XIS BI (XIS1), respectively.

Although no counterpart is found in literatures, the X-ray spectrum of Src2 with an absorption column density of $N_{\rm H} \sim 10^{23}$ cm^{-2} indicates an extragalactic source because that is larger than the Galactic absorption determined by the HI emission ($\sim$ 1.9 $\times$

Table 5.11: Best-fit results of the X-ray spectra in HESS J1841−055.[1]

	Src1	Src2	Src3	Src4
Model[2]	PL	PL	PL	PL
$N_{\rm H}$ (10^{22} cm^{-2})	$0.5^{+0.3}_{-0.2}$	$8.2^{+3.3}_{-2.7}$	$5.8^{+5.5}_{-3.8}$	—[5]
Γ	$1.7^{+0.4}_{-0.3}$	$1.8^{+0.5}_{-0.5}$	$1.4^{+0.9}_{-0.9}$	$0.4^{+0.2}_{-0.3}$
$F^{\rm obs}_{2-10{\rm keV}}$[3]	1.5	5.6	2.5	2.3
$F^{\rm abscor}_{2-10{\rm keV}}$[4]	1.6	9.4	3.5	2.3
χ^2/d.o.f.	41.77/48	67.53/57	53.06/38	96.72/60

[1] Errors are at the 90% confidence level.
[2] Model used for the spectral fitting: "PL" is a power-law model.
[3] Observed flux in the 2–10 keV band in units of 10^{-13} erg cm^{-2} s^{-1}.
[4] Absorption corrected flux in the 2–10 keV band in units of 10^{-13} erg cm^{-2} s^{-1}.
[5] The data are insensitive to the parameter, $N_{\rm H}$.

10^{22} cm^{-2}; Dickey & Lockman, 1990), and the photon index $\Gamma \simeq 2$ is agreed with that of the values of active galactic nuclei (AGNs). Time variation supports this scenario.

5.4 HESS J1857+026

5.4.1 Overview

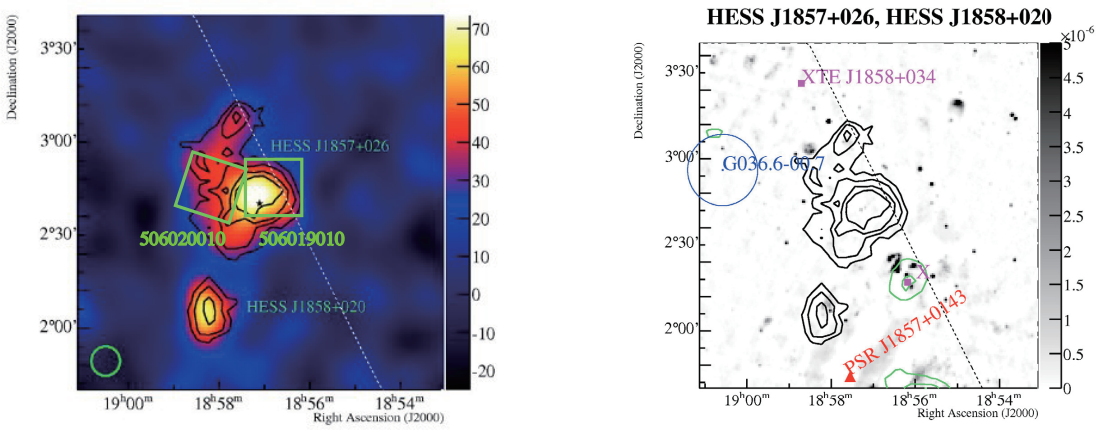

Figure 5.11: Left: γ-ray image of HESS J1857+026 and HESS J1858+020. The dotted line indicates the Galactic plane. Green squares represent the Suzaku/XIS field of views. Right: View of the region around HESS J1857+026 in other wavelength: H.E.S.S. significance contours (black) and adaptively smoothed ROSAT X-ray contours (green), overlaid on a NVSS radio image (grey-scale). Also shown are the positions of a known high spin-down flux pulsar (filled triangle), the supernova remnant G036.6−00.7 (circle), and the X-ray binary XTE J1858+034 (square). None of the objects qualifies as a plausible counterpart. (Both figures adapted from Aharonian et al. (2008b).)

HESS J1857+026 (Aharonian et al., 2008b) is an approximately radially-symmetric extended VHE γ-ray source located on the Galactic Plane, as shown in figure 5.11 (left). The source is detected by H.E.S.S. at a 9σ significance level at energies above 300 GeV and has a differential spectral index of $2.4 \pm 0.1_{\text{stat}} \pm 0.2_{\text{sys}}$. A view of the region in other wavelengths shows no plausible counterparts, as shown in figure 5.11 (right); a pulsar with high spin-down energy loss and a supernova remnant are both too far away from the γ-ray sources.

This situation changed with the recent discovery by Hessels et al. (2008) of a new pulsar, PSR J1856+0245, by the PALFA survey. Timing observations determined, beyond the spin period of 81 ms, the spin-down energy loss of 4.6×10^{36}erg s^{-1} and the characteristic age of 21000 yr, and provided a distance estimate of about 9 kpc (Hessels et al., 2008). The pulsar is located within the γ-ray source, slightly offset from its center, as shown in figure 5.12. Electrons accelerated near the pulsar are presumable responsible for γ-ray production, converting about 3% of the pulsar's spin down energy loss into high energy γ rays.

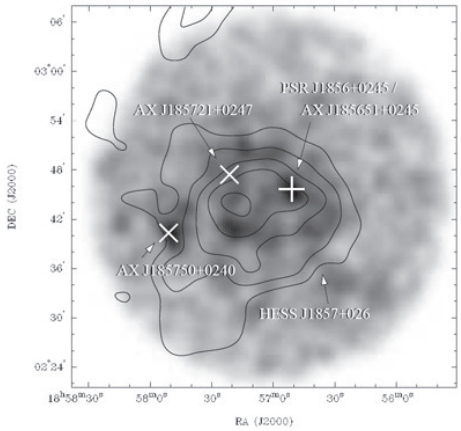

Figure 5.12: ASCA X-ray image of the HESS J1857+026 region, with H.E.S.S. significance contours (black lines) and the newly discovered pulsar PSR J1856+0245 marked with a plus sign (Hessels et al., 2008).

5.4.2 Observations

Suzaku observed HESS J1857+026 in September, 2011. Suzaku also observed one nearby position (BGD). Three XISs (XIS 0, 1, 3) were operated in the normal clocking mode with the Spaced-row Charge Injection (SCI) (Uchiyama et al., 2009b). We analyzed the data prepared by the version 2.7 pipeline. We concentrated on the analysis of the XIS data because we were interested in the spatial distribution of the emission. We applied the standard screening criteria to the XIS[4] data to obtain cleaned event lists. After the data screening, the net exposures were 40.9 ks and 40.7 ks for the HESS J1857+026 and BGD regions, respectively. The journal of these observations are summarized in table 5.12. We used HEADAS version 6.11.1 software package for the data analysis of HESS J1857+026.

Table 5.12: Journal of the Suzaku observations of HESS J1857+026.

Satellite	Suzaku	Suzaku
Sequence ID	506019010	506020010
Start time (UT)[1]	2011/09/18 22:04	2011/11/01 19:00
End time (UT)[1]	2011/09/19 23:37	2011/11/02 16:40
Aim point R.A. (J2000.0)	284°.2126	284°.5485
Aim point Decl. (J2000.0)	2°.7519	2°.7494
Net exposure (ks)	40.9	40.7

[1] Time form of yyyy/mm/dd hh:mm.

[4] ⟨http://www.astro.isas.jaxa.jp/suzaku/process/v2changes/criteria_xis.html⟩.

5.4.3 Analysis and Results

XIS Image

We extracted XIS images from each FI sensor using the screened data for the soft- (0.4–3 keV) and hard- (3–10 keV) energy bands. We excluded the corners of the CCD chips illuminated by the ^{55}Fe calibration sources. The images of the non-X-ray background (NXB) were generated using `xisnxbgen` (Tawa et al., 2008) and subtracted from the images. Then, the soft- and hard-band images were divided by flat sky images simulated at 1.49 and 4.5 keV using the XRT+XIS simulator `xissim` (Ishisaki et al., 2007) for vignetting corrections. Finally, the images from the two FI sensors were summed and binned by a factor of 8.

The XIS FI images of the HESS J1857+026 region (HESS J1857+026 and BGD) smoothed using a Gaussian function with $\sigma = 0'.28$ is shown in figure 5.13. In the hard-band image, five conspicuous X-ray sources (Src1, Src2, Src3, Src4 and Src5 in figure 5.13 (right)) were found. Src4 is also conspicuous in the soft-band image (figure 5.13 (left)). The coordinates are summarized in table 5.13. Table 5.14 shows possible counterpart of X-ray sources from the SIMBAD Astronomical Database.

We also examined the radial profiles in the 3–10 keV band. The profiles are consistent with the PSF plus a constant component model except for Src3 ($\chi^2/d.o.f. = 32.96/16$), and therefore Src3 must be extended or unresolved multiple sources.

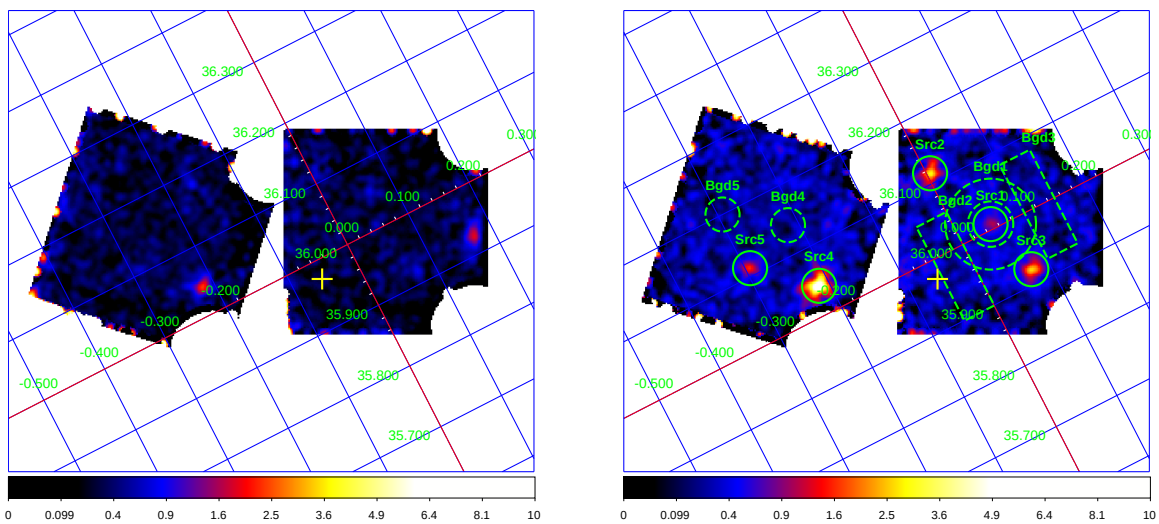

Figure 5.13: Suzaku XIS FI (XIS 0+3) images of the HESS J1857+026 region (HESS J1857+026 and BGD) in the Galactic coordinates: (left) 0.4–3 keV and (right) 3–10 keV bands. The images were smoothed using a Gaussian function with $\sigma = 0'.21$. A vignetting correction was applied after subtracting the NXB, as described in the text. The yellow cross indicates the best-fit position of the TeV γ-ray emission. The solid circles indicate the integration regions of source photons, and the regions bounded by a dashed line are those of background photons.

Table 5.13: X-ray sources in HESS J1857+026.

Source name	l (deg)	b (deg)	R.A. (deg)	Decl. (deg)
Src1	36.01	0.05	284.22	2.76
Src2	36.11	0.01	284.31	2.83
Src3	35.92	0.07	284.16	2.69
Src4	36.04	−0.22	284.47	2.67
Src5	36.11	−0.29	284.57	2.70

Table 5.14: Possible counterpart of X-ray sources of HESS J1857+026.

Source name	R.A. (deg)	Decl. (deg)	MAIN_ID	OTYPE[1]
Src1	284.213	2.763	AX J1856.8+0245	X
	284.21167	2.76394	PSR J1856+0245	Pulsar
Src2	284.30254	2.83631	SWIFT J185712.6+025010	X
Src4	284.463	2.672	AX J1857.8+0240	X
	284.4654	2.6800	SSTGLMC G036.0491−00.2060	Candidate_AGB*

[1] Object type.

XIS Spectrum

There are five conspicuous X-ray sources (Src1, Src2, Src3, Src4 and Src5 in figure 5.13 (right)) in the hard-band image. We also examined the light curves of the sources in the hard-energy band from these regions and found no significant time variability from them. Then, we investigated the spectra of these sources. The source and background regions for each source are described in figure 5.13 (right). The background-subtracted spectra of each source with the best-fit model are shown in figure 5.14. The best-fit parameters and the fluxes are listed in table 5.15.

The X-ray spectrum of Src1 is similar to that of PWNe and their parent pulsars (Kargaltsev & Pavlov, 2008). Since the radial profile of Src1 supports the assumption of a point source, it is reasonable to interpret as the X-ray emission comes from the pulsar PSR J1856+0245. However, Src1 could be an X-ray PWN created by PSR J1856+0245. The X-ray spectrum of Src2 with an absorption column density of $N_{\rm H} \sim 10^{23}$ cm^{-2} indicates an extragalactic source because that is much larger than the Galactic absorption determined by the HI emission ($\sim 1.8 \times 10^{22}$ cm^{-2}; Dickey & Lockman, 1990), and the photon index $\Gamma \sim 2$ may suggest active galactic nucleus (AGN). On the other hand, the extended nature and the X-ray spectrum of Src3 also implies emission from PWN, but there is no pulsar identified so far.

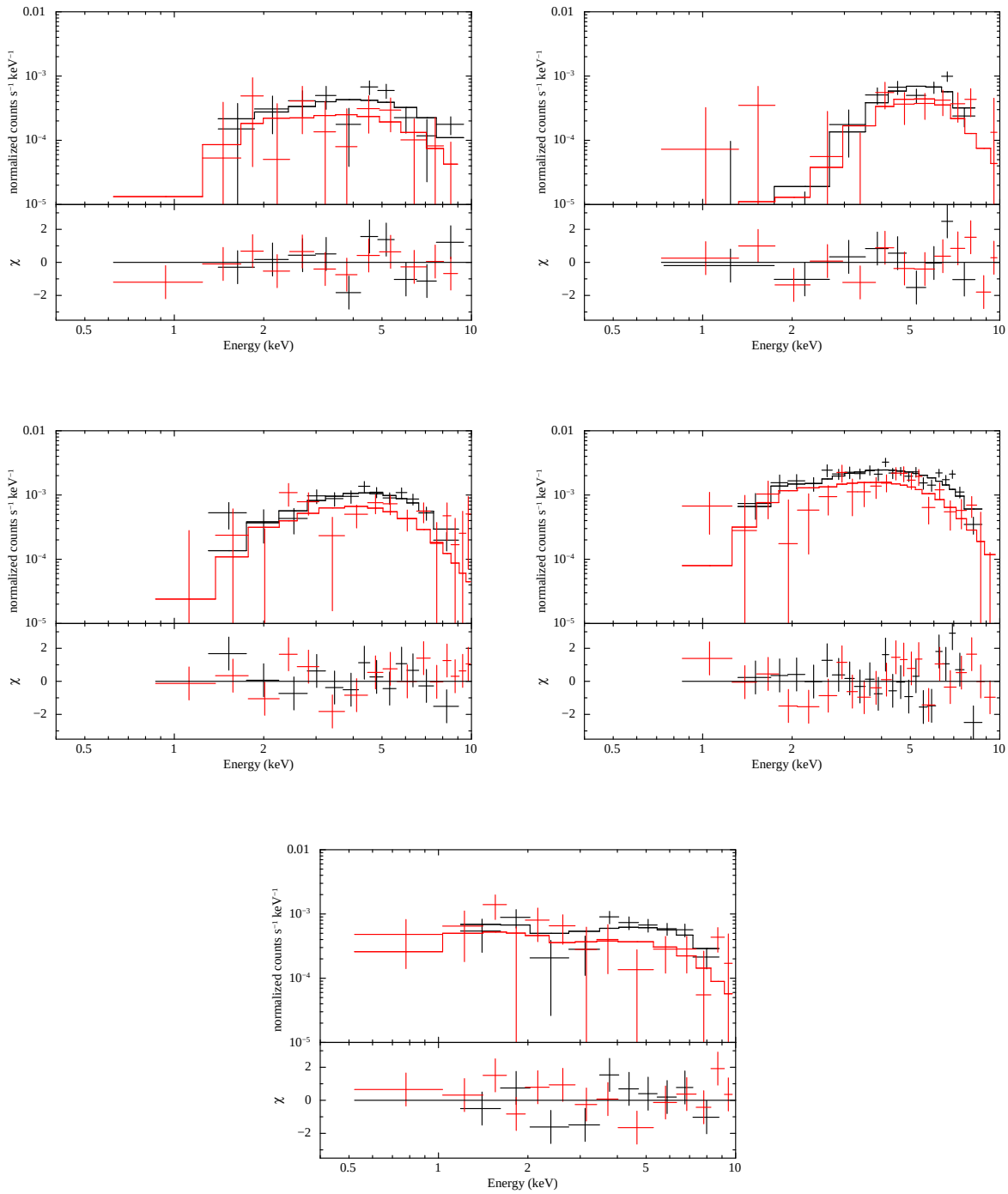

Figure 5.14: XIS spectra of Src1 (top-left), Src2 (top-right), Src3 (middle-left), Src4 (middle-right) and Src5 (bottom) in HESS J1857+026, shown with the best-fit model. Black and red lines represent the data and model for the XIS FI (XIS0+3) and XIS BI (XIS1), respectively.

Table 5.15: Best-fit results of the X-ray spectra in HESS J1857+026.[1]

	Src1	Src2	Src3	Src4	Src5
Model[2]	PL	PL	PL	PL	PL
$N_{\rm H}$ (10^{22} cm^{-2})	$2.7^{+5.2}_{-2.3}$	$19.7^{+20.5}_{-12.1}$	$4.8^{+4.6}_{-2.7}$	$3.1^{+1.3}_{-1.0}$	—
Γ	$1.0^{+1.2}_{-0.9}$	$0.9^{+1.7}_{-1.3}$	$1.1^{+0.7}_{-0.6}$	$1.0^{+0.3}_{-0.7}$	$0.2^{+0.3}_{-0.3}$
$F^{\rm obs}_{2-10{\rm keV}}$[3]	1.1	4.0	3.3	9.1	2.2
$F^{\rm abscor}_{2-10{\rm keV}}$[4]	1.2	7.6	4.2	10.8	2.2
χ^2/d.o.f.	16.54/18	23.74/18	24.41/25	54.64/40	22.25/20

[1] Errors are at the 90% confidence level.
[2] Model used for the spectral fitting: "PL" is a power-law model.
[3] Observed flux in the 2–10 keV band in units of 10^{-13} erg cm^{-2} s^{-1}.
[4] Absorption corrected flux in the 2–10 keV band in units of 10^{-13} erg cm^{-2} s^{-1}.
[5] The data are insensitive to the parameter, $N_{\rm H}$.

5.5 HESS J1843−033

5.5.1 Overview

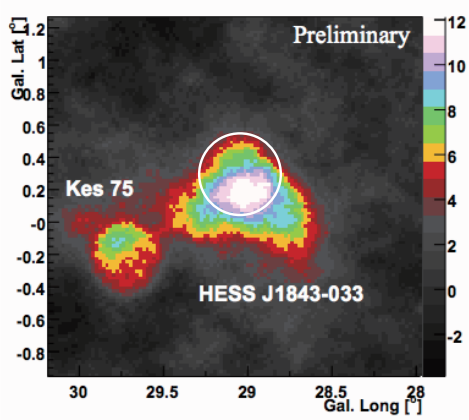

Figure 5.15: γ-ray significance map of the region containing Kes 75 (Hoppe et al., 2008). White circle represents the XMM-Newton/MOS field of view.

In the same field of view of the young shell-type supernova remnant (SNR) Kes 75, an extended source HESS J1843−033 was discovered with a statistical significance of more than 11σ post-trials (Hoppe et al., 2008). In contrast to Kes 75, no obvious counterpart for this source was found yet.

5.5.2 Observations

We analyzed the XMM-Newton archival data around HESS J1843−033. We used the standard processed and filtered event data of MOS 1 and MOS 2. The journal of this observation is summarized in table 5.16.

Table 5.16: Journal of the XMM-Newton observation of HESS J1843−033.

Satellite	XMM-Newton
Sequence ID	0654960101
Start time (UT)[1]	2010/09/24 22:49
End time (UT)[1]	2010/09/25 07:36
Aim point R.A. (J2000.0)	280°.8250
Aim point Decl. (J2000.0)	−3°.3125
Net exposure (ks)	31.6

[1] Time form of yyyy/mm/dd hh:mm.

5.5.3 Analysis and Results

X-ray Image

Figure 5.16 (left) shows the combined image of entire MOS 1 and MOS 2 field around HESS J1843−033 in the 2–10 keV band smoothed with a Gaussian function of $\sigma = 5''.5$ with the detected point sources using the source detection task `edetect_chain` in the SAS software package.

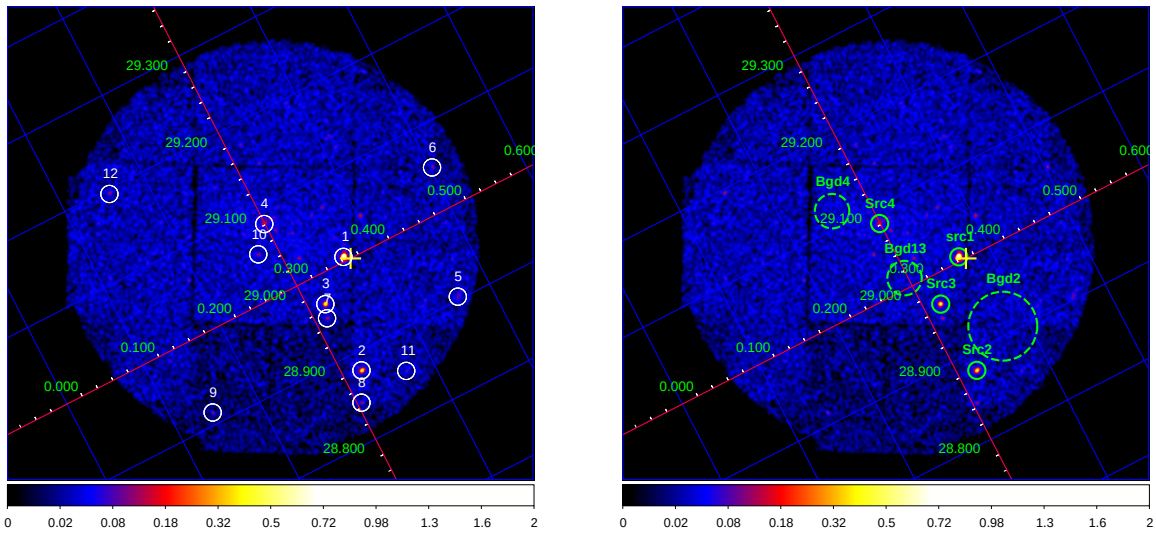

Figure 5.16: Left: XMM-Newton MOS 1 and MOS 2 combined image around HESS J1843−033. Vignetting was not corrected. The yellow cross indicates the best-fit position of the TeV γ-ray emission. Point sources identified by the SAS software package source detection task `edetect_chain` are indicated by white solid circles with the source numbers, which are numbered in order of decreasing count rate. Right: The same image as left. The solid circles indicate the integration regions of source photons, and the dashed circles are that of background photons.

X-ray Spectrum

There are four X-ray sources (Src1, Src2, Src3 and Src4 in figure 5.16 (right)) located in the vicinity of the best-fit position of the TeV γ-ray emission $(l,\ b) = (29°,\ 0°.37)$ with high count rate. The coordinates are summarized in table 5.17. We first examined the light curves of the sources in the hard-energy band from these regions and found no significant time variability from them. Then, we investigated the spectra of these sources. The source and background regions for each source are described in figure 5.16 (right). The background-subtracted spectra of each source with the best-fit model are shown in figure 5.17. The best-fit parameters and the fluxes are listed in table 5.18

Table 5.17: X-ray sources in HESS J1843−033.

Source name	l (deg)	b (deg)	R.A. (deg)	Decl. (deg)
Src1	29.01	0.36	280.74	−3.33
Src2	28.88	0.32	280.72	−3.46
Src3	28.97	0.32	280.76	−3.38
Src4	29.08	0.30	280.84	−3.29

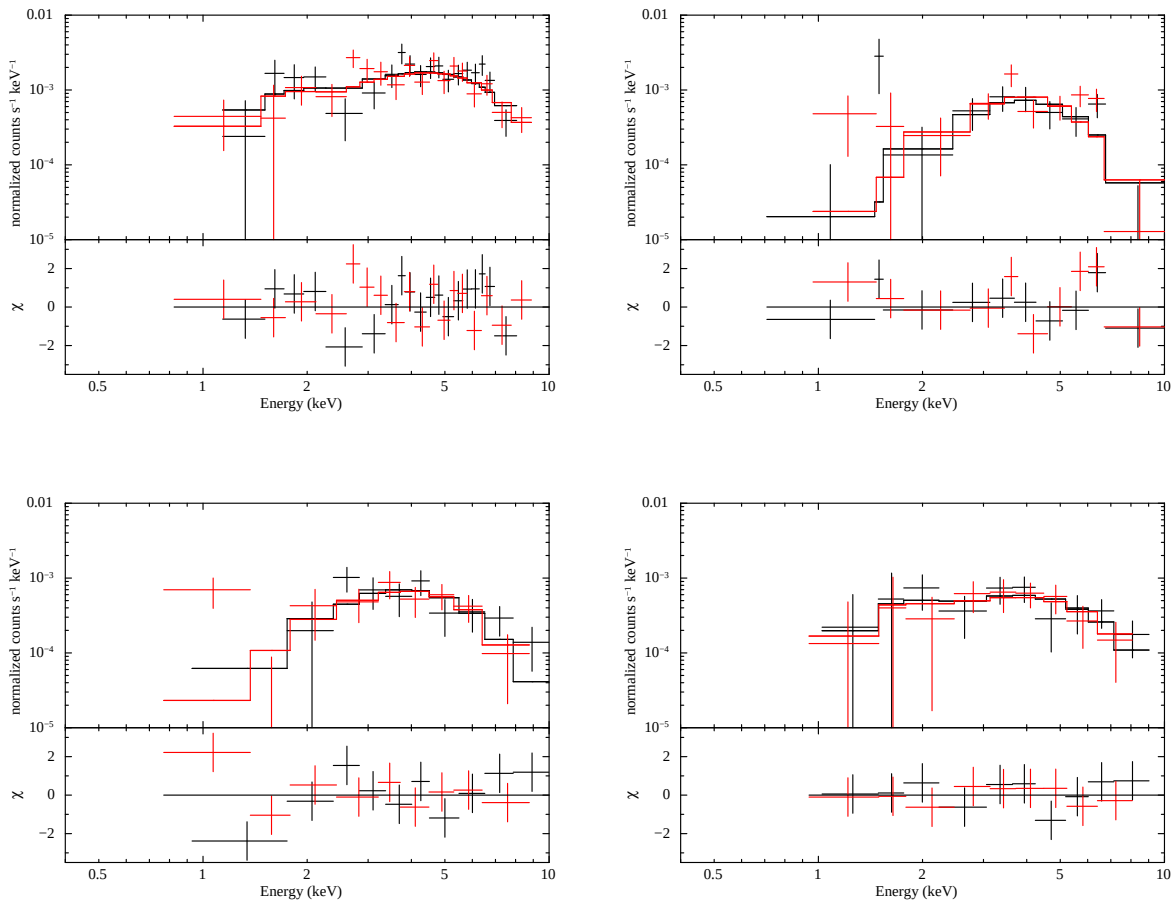

Figure 5.17: X-ray spectra of Src1 (top-left), Src2 (top-right), Src3 (bottom-left) and Src4 (bottom-right) in HESS J1843−033, shown with the best-fit model. Black and red lines represent the data and model for the MOS 1 and MOS 2, respectively.

Table 5.18: Best-fit results of the X-ray spectra in HESS J1843−033.[1]

	Src1	Src2	Src3	Src4
Model[2]	PL	PL	PL	PL
$N_{\rm H}$ (10^{22} cm^{-2})	$0.9^{+1.8}_{-0.9}$	$7.9^{+9.2}_{-5.3}$	$5.3^{+6.2}_{-3.6}$	$1.6^{+5.3}_{-1.6}$
Γ	$-0.5^{+0.5}_{-0.4}$	$1.4^{+2.0}_{-1.3}$	$1.0^{+1.7}_{-1.3}$	$0.4^{+1.6}_{-1.0}$
$F^{\rm obs}_{2-10{\rm keV}}$[3]	6.1	2.4	1.4	1.3
$F^{\rm abscor}_{2-10{\rm keV}}$[4]	6.3	3.6	1.8	1.4
χ^2/d.o.f.	36.53/33	23.02/16	20.43/15	5.60/15

[1] Errors are at the 90% confidence level.
[2] Model used for the spectral fitting: "PL" is a power-law model.
[3] Observed flux in the 2–10 keV band in units of 10^{-13} erg cm^{-2} s^{-1}.
[4] Absorption corrected flux in the 2–10 keV band in units of 10^{-13} erg cm^{-2} s^{-1}.

5.6 HESS J1634−472

5.6.1 Overview

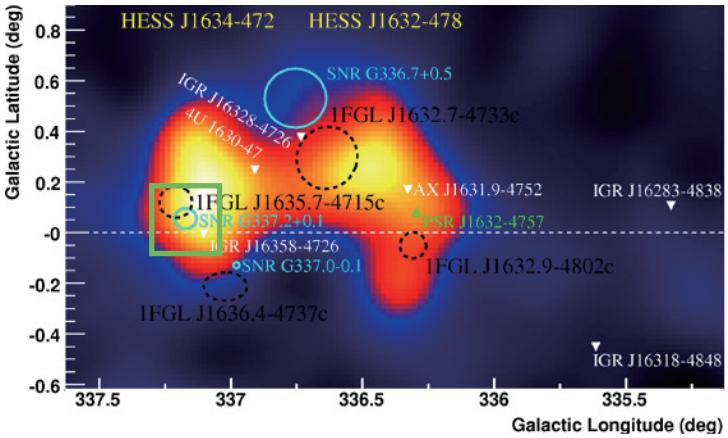

Figure 5.18: γ-ray sky map of the regions of HESS J1634−472 and HESS J1632−478 (Aharonian et al., 2006a). Also included are the locations of four Fermi LAT sources (black dashed circles; the circle size indicates position uncertainty, not source size), supernova remnants (green circles), X-ray sources and the pulsar PSR J1632−4757. Green square represents the Chandra/ACIS-I field of view.

The size of HESS J1634−472 (left-hand source in figure 5.18) emission region is $6'.6 \pm 1'.8$ and its flux above 200 GeV is close to 6% of the Crab flux with a photon index for the energy spectrum of 2.38 ± 0.26 (Aharonian et al., 2006a). HESS J1634−472 has no direct positional counterpart, although it is interesting to note that yet another INTEGRAL source IGR J16358−4726 is located close by (Revnivtsev et al., 2003). This source presumably belongs to the class of highly absorbed X-ray binary systems, like IGR J16320−4751 (Tomsick et al., 2003). Another potential counterpart of HESS J1634−472 is the recently discovered SNR candidate G337.2+0.1 (Combi et al., 2005, 2006). The object was discovered by the Molonglo Observatory Synthesis Telescope Galactic plane survey at 843 MHz toward the Norma spiral arm (Whiteoak & Green, 1996), and later, detected with the ASCA telescope during a survey of part of the Galactic plane (Sugizaki et al., 2001). Its integrated flux was reported to be $\sim 1.2 \times 10^{-12}$ erg cm^{-2} s^{-1} in the 0.7–10 keV band. The photon index is $\Gamma = 2.8^{+2.6}_{-1.6}$, and the absorption column density yielded $N_{\rm H} = 15^{+15}_{-9} \times 10^{22}$ cm^{-2} (Combi et al., 2005). Combi et al. (2005) also found a sharp absorption feature in the HI distribution toward the continuum radio source in the velocity range of ~ -25 to -19 km s^{-1}, and estimated the lower bound of 14 kpc on the distance to the SNR candidate. Then, Combi et al. (2006) reported the XMM-Newton observations of the object. They confirmed the SNR nature and suggested that the central region of the source is a PWN, originated by a nondetected energetic pulsar.

5.6.2 Observations

We analyzed the Chandra archival data around HESS J1634−472. We used the standard processed and filtered event data. The journal of this observation is summarized in table 5.19.

Table 5.19: Journal of the Chandra observation of HESS J1634−472.

Satellite	Chandra
Sequence ID	10087
Start time (UT)[1]	2009/06/22 13:18
End time (UT)[1]	2009/06/22 16:27
Aim point R.A. (J2000.0)	248°.9908
Aim point Decl. (J2000.0)	−47°.3217
Net exposure (ks)	10.0

[1] Time form of yyyy/mm/dd hh:mm.

5.6.3 Analysis and Results

X-ray Image

Figure 5.19 shows the entire image around HESS J1634−472 covered by the 4 CCD of ACIS-I in the 2.0–7.0 keV band smoothed with a Gaussian function of $\sigma = 7''.4$ with the detected point sources using the source detection tool `wavdetect` in the CIAO software package. As mentioned before, since the best-fit position of the VHE γ-ray emission is located outside of the field of view, we focused on diffuse X-ray emission. In the image, one extended X-ray source (Src1 in figure 5.19) was found. The coordinates are summarized in table 5.20. Table 5.21 shows possible counterpart of X-ray source from the SIMBAD Astronomical Database.

Table 5.20: X-ray sources in HESS J1634−472.

Source name	l (deg)	b (deg)	R.A. (deg)	Decl. (deg)
Src1	337.18	0.06	248.98	−47.32

X-ray Spectrum

We investigated the spectrum of the X-ray source (Src1 in figure 5.19). The source and background regions for the source is described in figure 5.19. The background-subtracted spectrum of the source with the best-fit model is shown in figure 5.20. The best-fit

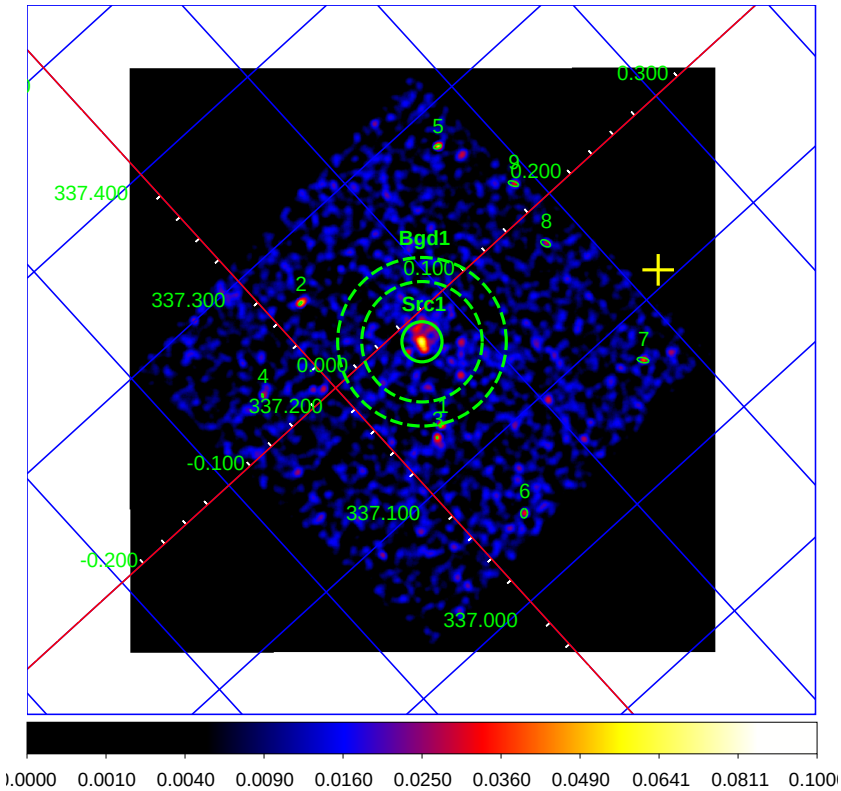

Figure 5.19: Chandra ACIS image in Galactic coordinate around HESS J1634−472 in the 2.0–7.0 keV band. The image is smoothed with a Gaussian function of $\sigma = 7''.4$. Vignetting was not corrected. The yellow cross indicates the best-fit position of the TeV γ-ray emission. Point sources identified by the CIAO software package source detection tool `wavdetect` are indicated by solid circles with the source numbers. The solid circle (Src1) indicates the integration region of source photons, and the dashed annulus (Bgd1) is that of background photons.

Table 5.21: Possible counterpart of X-ray source of HESS J1634−472.

Source name	R.A. (deg)	Decl. (deg)	MAIN_ID	OTYPE[1]
Src1	248.9833	-47.3317	SNR G337.2+00.1	SNR
	248.963204	-47.330983	2MASS J16355116−4719515	IR
	248.987	-47.317	MSC 337.2+0.7	SNR?

[1] Object type.

parameters and the fluxes are listed in table 5.22. We also examined the light curve of the source in the hard-energy band and found no significant time variability.

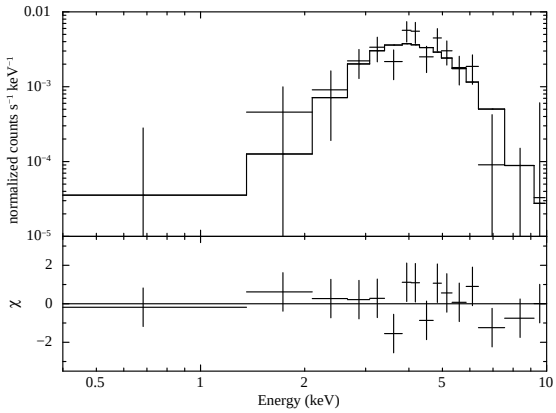

Figure 5.20: X-ray spectrum of Src1 in HESS J1634−472, shown with the best-fit model. Black lines represent the data and model.

Table 5.22: Best-fit results of the X-ray spectrum in HESS J1634−472.[1]

	Src1
Model[2]	PL
$N_{\rm H}$ (10^{22} cm^{-2})	$15.6^{+13.5}_{-9.8}$
Γ	$3.3^{+3.5}_{-2.0}$
$F^{\rm obs}_{2-10{\rm keV}}$ [3]	3.2
$F^{\rm abscor}_{2-10{\rm keV}}$ [4]	12.3
χ^2/d.o.f.	10.74/15

[1] Errors are at the 90% confidence level.
[2] Model used for the spectral fitting: "PL" is a power-law model.
[3] Observed flux in the 2–10 keV band in units of 10^{-13} erg cm^{-2} s^{-1}.
[4] Absorption corrected flux in the 2–10 keV band in units of 10^{-13} erg cm^{-2} s^{-1}.

The best-fit parameters of Src1 are consistent with that of ASCA and XMM-Newton (Combi et al., 2005, 2006). However, if the distance to the source is 14 kpc, the distance of the source to HESS J1634−472 would be $\sim$ 43 pc, and render a correlation unlikely.

5.7 HESS J1848−018

5.7.1 Overview

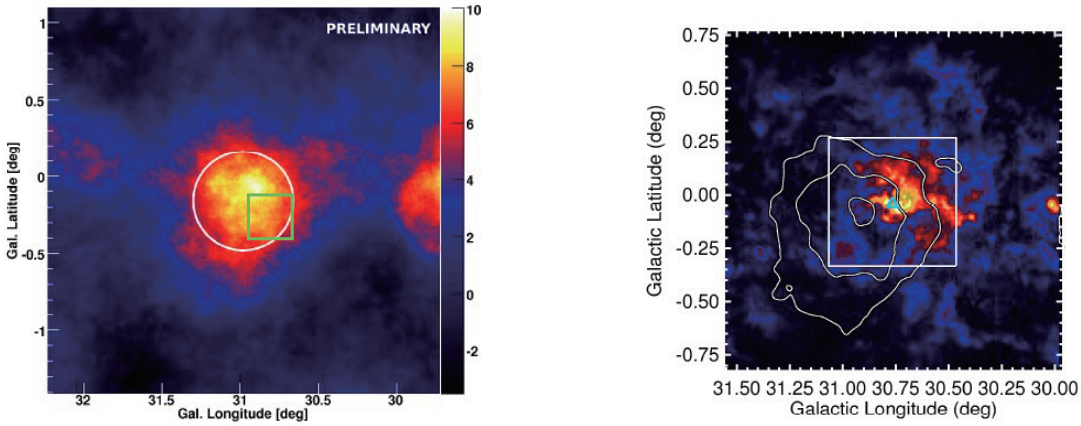

Figure 5.21: Left: Sky map of HESS J1848−018 region, showing the significance of γ-ray counts. The white circle shows the estimate of the intrinsic size of the source of about $0^{\circ}.3$. The source at the right edge of the image is the supernova remnant Kes 75. Green square represents the Chandra/ACIS-I field of view. Right: Color map: CO emission tracing molecular clouds at a distance of about 5 kpc (corresponding to 85 to 95 km/s velocity). Overlayed in white are the HESS J1848−018 contours of detection significance, for 5, 7 and 9σ. The position of the Wolf-Rayet star WR 121 is marked by the green triangle. The white square used for the region of the velocity profile (Chaves et al., 2008). (Both figures adapted from Chaves et al. (2008).)

HESS J1848−018 is an extended VHE γ-ray source which was recently detected in the H.E.S.S. Galactic Plane Survey with a statistical significance of $\sim 9\sigma$ in ~ 50 hours of effective exposure (Chaves et al., 2008). Figure 5.21 (left) shows the significance map of the recently discovered source HESS J1848−018. Its differential energy spectrum is well fit by a power law with index $\Gamma = 2.8 \pm 0.2_{\rm stat}$ and it has an integrated flux above 1 TeV of $\sim 2 \times 10^{-12}$ erg cm^{-2} s^{-1}, corresponding to $\sim 8\%$ that of the Crab nebula. HESS J1848−018 is located along the Scutum-Crux spiral arm tangent and is in the direction of, but slightly offset from, the star-forming region W 43, which hosts a giant HII region (G30.8−0.2), a giant molecular cloud, and the Wolf-Rayet (WR) star WR 121a in the central stellar cluster. If HESS J1848−018 is indeed associated with W 43, it would be only the second known case, after Westerlund 2 (Aharonian et al., 2007a), of VHE γ-ray emission associated with a star-forming region and WR star.

5.7.2 Observations

We analyzed the Chandra archival data around HESS J1848−018. We used the standard processed and filtered event data. The journal of this observation is summarized in table 5.23.

Table 5.23: Journal of the Chandra observation of HESS J1848−018.

Satellite	Chandra
Sequence ID	12152
Start time (UT)[1]	2010/08/08 08:03
End time (UT)[1]	2010/08/08 11:27
Aim point R.A. (J2000.0)	282°.1325
Aim point Decl. (J2000.0)	−1°.9972
Net exposure (ks)	9.92

[1] Time form of yyyy/mm/dd hh:mm.

5.7.3 Analysis and Results

X-ray Image

Figure 5.22 shows the entire image around HESS J1848−018 covered by the 4 CCD of ACIS-I in the 2.0–7.0 keV band smoothed with a Gaussian function of $\sigma = 3''.4$ with the detected point sources using the source detection tool `wavdetect` in the CIAO software package. As mentioned before, since the best-fit position of the VHE γ-ray emission is located outside of the field of view, we focused on diffuse X-ray emission. However, there was no extended X-ray source.

X-ray Spectrum

The overall topology of the source bears similarity to the γ-ray source HESS J1023−575, which is slightly offset from, but overlapping with the Westerlund 2 stellar cluster with its Wolf-Rayet stars WR 20a and WR 20b (Aharonian et al., 2007a). Since the X-ray observation of Westerlund 2 using the Suzaku satellite found diffuse X-ray emission extends to $\sim 8'$ from the cluster center (Fujita et al., 2009), we estimated the flux upper limit of the diffuse X-ray emission of this region. In order to determine the upper limit, we assumed a spectrum; an absorbed power law with the photon index $\Gamma = 2.0$ and the hydrogen-equivalent column density $N_{\rm H} = 2.2 \times 10^{22}$ cm^{-2}.

We extracted the photons from the source region, the solid circle with a radius of $8'.5$ (figure 5.22) excluding the regions of the detected point sources with a radius of $0'.5$, in the 2–7 keV band. The number of the accumulated photons was 5741 ± 76 counts. We estimated the photons of the background emission, using the other observational data set with the same manner as the source region. The number of the accumulated photons was 13596 ± 117 counts. Thus, the number of the area and exposure corrected source minus background photons was 398 ± 89 counts, and the 3σ confidence upper limit on the photons in the source region was estimated to be 665 counts. Therefore, the 3σ confidence upper limit on the count rate in the source region was 0.067 counts s^{-1}. Then, the upper limit on the flux from the circle of $8'.5$ radius (figure 5.22) is 2.1×10^{-12} erg cm^{-2} s^{-1} in the 2–10 keV band.

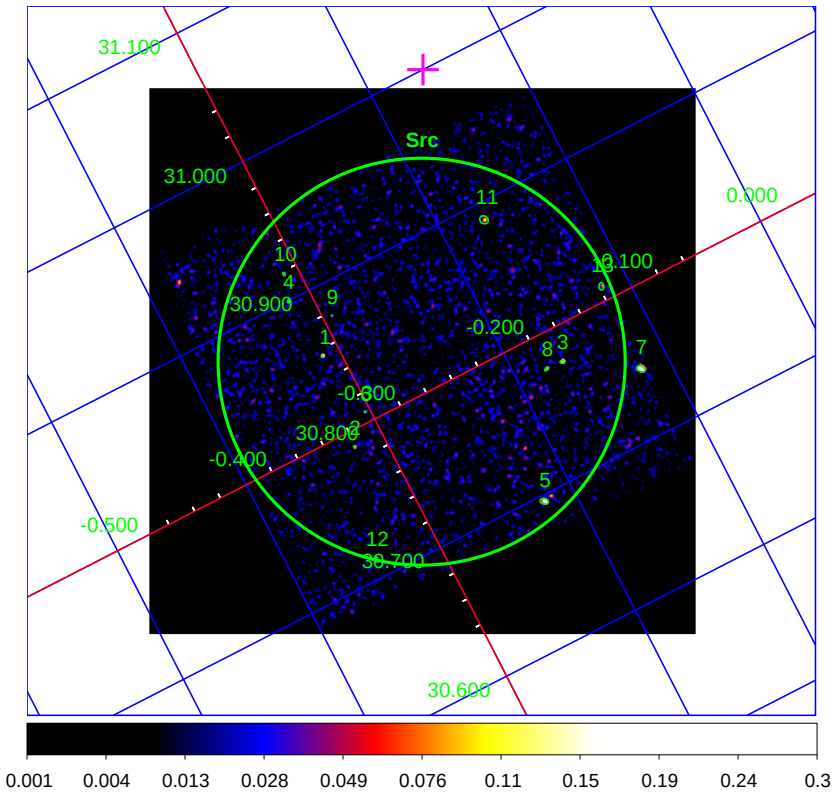

Figure 5.22: Chandra ACIS image in Galactic coordinate around HESS J1848−018 in the 2.0–7.0 keV band. The image is smoothed with a Gaussian function of $\sigma = 3''.4$. Vignetting was not corrected. The magenta cross indicates the best-fit position of the TeV γ-ray emission. Point sources identified by the CIAO software package source detection tool `wavdetect` are indicated by solid circles with the source numbers. The large solid circle (Src) indicates the integration region of source photons.

5.8 HESS J1858+020

5.8.1 Overview

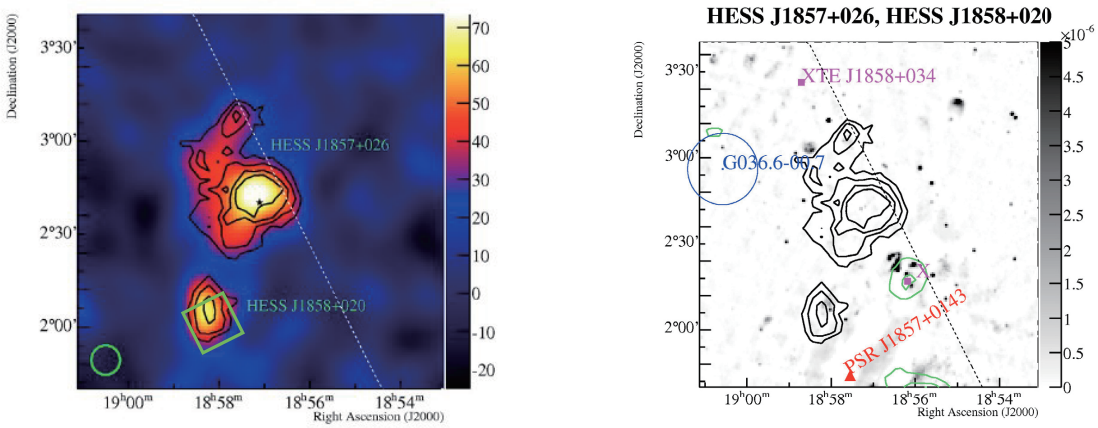

Figure 5.23: Left: a VHE γ-ray image of HESS J1857+026 and HESS J1858+020. Green square represents the Chandra/ACIS-I field of view. Right: the H.E.S.S. significance (block) and adaptively smoothed ROSAT X-ray contours (green), overlaid on an NVSS radio image (grey-scale). Also shown are the positions of a known high spin-down flux pulsar (filled triangle), the SNR G036.6−00.7 (circle), the ROSAT point-source 1RXS J185609.2+021744 (labeled X), and the HMXB XTE J1858+034 (square). (Both figures adapted from Aharonian et al. (2008b).)

The weak γ-ray source HESS J1858+020 (shown in figure 5.23) lies close to HESS J1857+026; however, there is no significant emission connecting them, suggesting that they are distinct objects (Aharonian et al., 2008b). It is detected at a significance level of 7σ with a differential spectral index of $2.2 \pm 0.1_{\rm stat} \pm 0.2_{\rm sys}$. Though nearly point-like, its morphology shows a slight extension of $\sim 5'$ along its major axis.

5.8.2 Observations

We analyzed the Chandra archival data around HESS J1858+020. We used the standard processed and filtered event data. The journal of this observation is summarized in table 5.24.

5.8.3 Analysis and Results

X-ray Image

Figure 5.24 (left) shows the entire image around HESS J1858+020 covered by the 4 CCD of ACIS-I in the 2.0–7.0 keV band smoothed with a Gaussian function of $\sigma = 3''.4$ with the detected point sources using the source detection tool `wavdetect` in the CIAO software package.

Table 5.24: Journal of the Chandra observation of HESS J1858+020.

Satellite	Chandra
Sequence ID	9116
Start time (UT)[1]	2008/06/21 14:52
End time (UT)[1]	2008/06/21 23:53
Aim point R.A. (J2000.0)	284°.5587
Aim point Decl. (J2000.0)	2°.0417
Net exposure (ks)	29.8

[1] Time form of yyyy/mm/dd hh:mm.

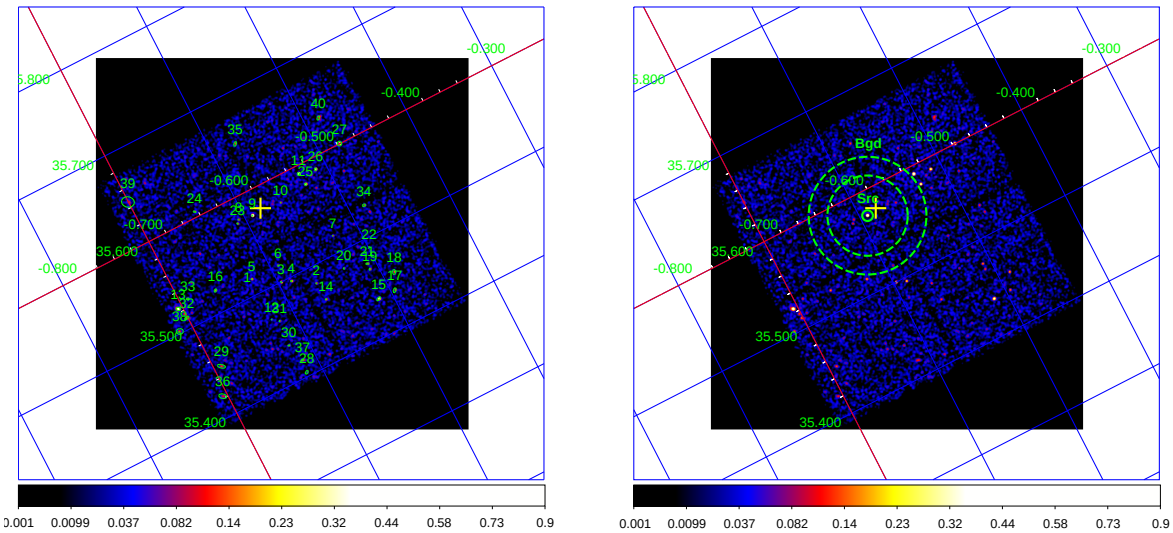

Figure 5.24: Left: Chandra ACIS image in Galactic coordinate around HESS J1858−020 in the 2.0–7.0 keV band. The image is smoothed with a Gaussian function of $\sigma = 3''.4$. Vignetting was not corrected. The yellow cross indicates the best-fit position of the TeV γ-ray emission. Point sources identified by the CIAO software package source detection tool `wavdetect` are indicated by solid circles with the source numbers. Right: The same image as left. The solid circle indicates the integration region of source photons, and the dashed annulus is that of background photons.

X-ray Spectrum

There is the X-ray source (Src in figure 5.24 (right)) located in the vicinity of the best-fit position of the TeV γ-ray emission $(l,\ b) = (35°.578,\ -0°.581)$. The coordinates are summarized in table 5.25. Table 5.26 shows possible counterpart of X-ray source from the SIMBAD Astronomical Database. We also examined the light curve of the source in the hard-energy band and found no significant time variability. Then, we investigated the spectrum of this source. The source and background regions for the source is described in figure 5.24 (right). The background-subtracted spectrum of the source with the best-fit model is shown in figure 5.25. The best-fit parameters and the fluxes are listed in table 5.27.

Table 5.25: X-ray sources in HESS J1858+020.

Source name	l (deg)	b (deg)	R.A. (deg)	Decl. (deg)
Src	35.57	−0.59	284.59	2.08

Table 5.26: Possible counterpart of X-ray source of HESS J1858+020.

Source name	R.A. (deg)	Decl. (deg)	MAIN_ID	OTYPE[1]
Src	284.592279	2.083617	2MASS J18582214+0205010	IR

[1] Object type.

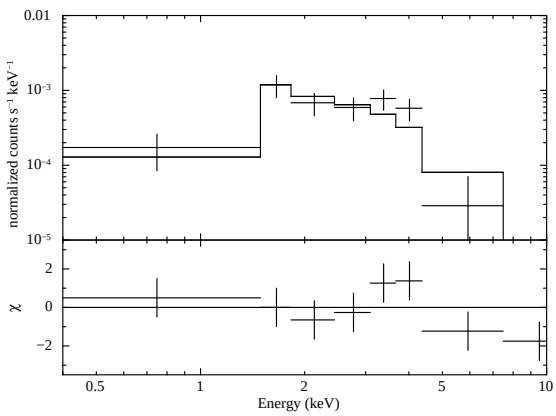

Figure 5.25: X-ray spectrum of Src in HESS J1858−020, shown with the best-fit model. Black lines represent the data and model.

Table 5.27: Best-fit results of the X-ray spectrum in HESS J1858−020.[1]

	Src
Model[2]	PL
$N_{\rm H}$ (10^{22} cm^{-2})	$3.6^{+3.8}_{-1.9}$
Γ	$3.5^{+2.1}_{-1.3}$
$F^{\rm obs}_{2-10{\rm keV}}$[3]	0.3
$F^{\rm abscor}_{2-10{\rm keV}}$[4]	0.5
χ^2/d.o.f.	8.83/5

[1] Errors are at the 90% confidence level.
[2] Model used for the spectral fitting: "PL" is a power-law model.
[3] Observed flux in the 2–10 keV band in units of 10^{-13} erg cm^{-2} s^{-1}.
[4] Absorption corrected flux in the 2–10 keV band in units of 10^{-13} erg cm^{-2} s^{-1}.

5.9 Discussion of the unidentified VHE γ-ray sources

5.9.1 Summary of the unidentified VHE γ-ray sources

Here we summarize the results obtained from our analysis of the X-ray data of the unidentified VHE γ-ray sources together with those from literature. The summaries are arranged in tables.

In table 5.28, we list the unidentified VHE γ-ray sources, which are selected according to the criteria described in the beginning of §5, with the best-fit positions and sizes. Related references to the unidentified VHE γ-ray sources are also summarized in the table.

In table 5.29, we list the spectral parameters and fluxes in both VHE γ-ray and X-ray bands. For the sources we do not analyzed, possible counterparts and parameters were taken from the literature. On the other hand, for the sources we analyzed, all X-ray sources we found are listed as a possible counterpart. The VHE γ-ray fluxes were taken from the literature and were converted in the 1–10 TeV band. The unabsorbed X-ray fluxes, which were normalized to 2–10 keV band, were also taken from the literature except for the sources which were analyzed in this thesis. Related references to the unidentified VHE γ-ray sources and X-ray sources are also summarized in the table.

Table 5.28: Positions and sizes of the unidentified VHE γ-ray sources.

Name	l (deg)	b (deg)	R.A. (deg)	Decl. (deg)	σ (deg)[1]	σ' (deg)[2]	ω (deg)[3] / ω' (deg)[4]	References[5]
HESS J1018-589	284.26	-1.82	154.44	-59.00	0.30	···	···	1
HESS J1427-608	314.409	-0.145	216.97	-60.85	0.04	0.08	— / 80	2
HESS J1507-622	317.95	-3.49	226.72	-62.35	0.15	···	···	3
HESS J1626-490	334.772	0.045	246.52	-49.09	0.07	0.10	— / 3	2
HESS J1634-472	337.11	0.22	248.74	-47.27	0.11	···	···	4
HESS J1702-420	344.30	-0.18	255.68	-42.02	0.30	0.15	— / 68	2
HESS J1708-410	345.68	-0.47	257.10	-41.09	0.06	0.08	— / -20	2
HESS J1729-345	353.44	-0.13	262.40	-34.54	0.14	···	···	5
HESS J1741-302	(358.40)	(0.19)	(265.25)	(-30.20)	—	—	—	6 (14)
HESS J1804-216	8.40	-0.03	271.13	-21.70	0.200	···	···	4
HESS J1834-087	23.24	-0.32	278.69	-8.76	0.09	···	···	4
HESS J1837-069	25.18	-0.11	279.41	-6.95	0.12	0.05	149 / —	4
HESS J1841-055	26.795	-0.197	280.23	-5.55	0.41	0.25	— / 39	2
HESS J1843-033	(29)	(0.37)	(280.75)	(-3.3)	—	—	—	7 (15)
HESS J1857+026	35.972	-0.056	284.30	2.67	0.11	0.08	— / -3	2
HESS J1858+020	35.578	-0.581	284.58	2.09	0.08	0.02	— / 4	2
HESS J1503-582	319.7	0.3	225.91	-58.23	0.26	···	···	8
HESS J1614-518	331.52	-0.58	243.58	-51.82	0.23	0.15	49 / —	4
HESS J1646-458	339.55	-0.35	251.71	-45.82	1.10	···	···	9
HESS J1848-018	31.00	-0.16	282.12	-1.79	0.32	···	···	10
MGRO J1908+06	40.39	-0.79	286.98	6.27	0.34	···	···	11
TeV J2032+4130	80.32	1.09	307.99	41.50	0.10	···	···	12
Westerlund 2	284.19	-0.39	155.83	-57.76	0.18	···	···	13

[1] The best-fit major-axis.
[2] The best-fit minor-axis.
[3] The orientation angle ω counter-clockwise with respect to the positive Galactic latitude axis.
[4] The position angle is measured counter-clockwise relative to the RA axis.
[5] (1)H.E.S.S. Collaboration et al. (2012), (2)Aharonian et al. (2008a), (3)H.E.S.S. Collaboration et al. (2011a), (4)Aharonian et al. (2006a), (5)H.E.S.S. Collaboration et al. (2011b), (6)Tibolla et al. (2009), (7)Hoppe et al. (2008), (8)Renaud et al. (2008a), (9)Abramowski et al. (2012), (10)Chaves et al. (2008), (11)Aharonian et al. (2009), (12)Aharonian et al. (2005c), (13)Aharonian et al. (2007a), (14)TeVCat, (15)TeGaSoCat

Table 5.29: Spectral parameters and fluxes of the unidentified VHE γ-ray sources.

Name	Type[1]	Possible counterpart	Satellite	$\Gamma_{\rm TeV}$[2]	$f_{\rm TeV}$[3]	$N_{\rm H}$[4]	$\Gamma_{\rm X}$[5]	$f_{\rm X}$[6]	$f_{\rm TeV}/f_{\rm X}$	References[7]
HESS J1018-589	UNID	XMMU J101855.4-58564	XMM-Newton	2.9 ± 0.4	0.11	6.6 ± 0.8	1.7 ± 0.1	0.069	1.6	1, 1
HESS J1427-608	UNID	No name	Suzaku	2.2 ± 0.1	0.4	51^{+13}_{-11}	$2.0^{+0.4}_{-0.3}$	0.46	0.9	2, 11
HESS J1507-622	UNID	No name	Chandra	2.5 ± 0.2	0.68	—	—	0.011	62	3, 3
HESS J1507-622 1	UNID	No name (src1)	Suzaku	2.5 ± 0.2	0.68	8^{+6}_{-4}	$2.4^{+0.6}_{-0.4}$	0.009	76	3, This work
HESS J1507-622 2	UNID	No name (src2)	Suzaku	2.5 ± 0.2	0.68	5 ± 1	1.8 ± 0.1	0.10	6.8	3, This work
HESS J1626-490	UNID	$\cdots$	XMM-Newton	2.2 ± 0.1	1.5	—	—	< 0.49 (1–10 keV)	> 3.1	2, 12
HESS J1634-472	UNID	AX J1635.9-4719 (src1)	Chandra	2.4 ± 0.3	0.49	156^{+135}_{-98}	$3.3^{+3.5}_{-2.0}$	0.12	4.1	4, This work
HESS J1702-420	UNID	$\cdots$	Suzaku	2.1 ± 0.1	3.1	—	—	< 0.27	> 11	2, 13
HESS J1708-410	UNID	$\cdots$	XMM-Newton	2.5 ± 0.1	0.61	—	—	< 0.18 (0.3–10 keV)	> 3.4	2, 14
HESS J1729-345	UNID	— No X-ray observation —		2.2 ± 0.2	0.1	— No X-ray observation —				5
HESS J1741-302	UNID	No name	Suzaku	2.8 ± 0.2	0.27	40 ± 27	1.1 ± 0.6	0.040	7	6, 15
HESS J1804-216 1	UNID	Suzaku J1804-2142	Suzaku	2.7 ± 0.1	1.0	$2\ (< 22)$	$-0.3^{+0.1}_{-0.5}$	0.025	40	4, 16
HESS J1804-216 2	UNID	Suzaku J1804-2140	Suzaku	2.7 ± 0.1	1.0	110^{+100}_{-57}	$1.7^{+1.4}_{-1.0}$	0.043	23	4, 16
HESS J1834-087	UNID	CXOU J183434.9-084443	Chandra	2.5 ± 0.2	0.60	272 (fixed)	2.7 ± 0.5	0.058	10	4, 17
HESS J1837-069	UNID	AX J1838.0-0655	Suzaku	2.3 ± 0.1	1.4	54 ± 5	1.3 ± 0.1	1.1	1.3	4, 18
HESS J1841-055 1	UNID	No name (src1)	Suzaku	2.4 ± 0.1	3.1	5^{+3}_{-2}	$1.7^{+0.4}_{-0.3}$	0.016	194	2, This work
HESS J1841-055 2	UNID	No name (src2)	Suzaku	2.4 ± 0.1	3.1	82^{+33}_{-27}	1.8 ± 0.5	0.094	33	2, This work
HESS J1841-055 3	UNID	No name (src3)	Suzaku	2.4 ± 0.1	3.1	58^{+55}_{-38}	1.4 ± 0.9	0.035	89	2, This work
HESS J1841-055 4	UNID	No name (src4)	Suzaku	2.4 ± 0.1	3.1	—	$0.4^{+0.2}_{-0.3}$	0.023	135	2, This work
HESS J1843-033 1	UNID	No name (src1)	XMM-Newton	—	—	9^{+18}_{-9}	$-0.5^{+0.5}_{-0.4}$	0.063	—	7, This work
HESS J1843-033 2	UNID	No name (src2)	XMM-Newton	—	—	79^{+92}_{-53}	$1.4^{+2.0}_{-1.3}$	0.036	—	7, This work
HESS J1843-033 3	UNID	No name (src3)	XMM-Newton	—	—	53^{+62}_{-36}	$1.0^{+1.7}_{-1.3}$	0.018	—	7, This work
HESS J1843-033 4	UNID	No name (src4)	XMM-Newton	—	—	16^{+53}_{-16}	$0.4^{+1.6}_{-1.0}$	0.014	—	7, This work
HESS J1857+026 1	UNID	No name (src1)	Suzaku	2.4 ± 0.1	1.5	27^{+52}_{-23}	$1.0^{+1.2}_{-0.9}$	0.012	125	2, This work
HESS J1857+026 2	UNID	No name (src2)	Suzaku	2.4 ± 0.1	1.5	197^{+205}_{-121}	$0.9^{+1.7}_{-1.3}$	0.076	20	2, This work
HESS J1857+026 3	UNID	No name (src3)	Suzaku	2.4 ± 0.1	1.5	48^{+46}_{-27}	$1.1^{+0.7}_{-0.6}$	0.042	36	2, This work
HESS J1857+026 4	UNID	No name (src4)	Suzaku	2.4 ± 0.1	1.5	31^{+13}_{-10}	$1.0^{+0.3}_{-0.7}$	0.11	14	2, This work
HESS J1857+026 5	UNID	No name (src5)	Suzaku	2.4 ± 0.1	1.5	—	0.2 ± 0.3	0.022	68	2, This work
HESS J1858+020	UNID	No name (src)	Chandra	2.2 ± 0.1	0.18	36^{+38}_{-19}	$3.5^{+2.1}_{-1.3}$	0.005	36	2, This work
HESS J1503-582 1	DARK	No name (src1)	Suzaku	2.4 ± 0.4	0.39	5^{+16}_{-5}	$0.3^{+0.6}_{-0.5}$	0.031	13	8, This work
HESS J1503-582 2	DARK	No name (src2)	Suzaku	2.4 ± 0.4	0.39	210^{+277}_{-187}	$1.9^{+5.4}_{-2.5}$	0.038	10	8, This work
HESS J1503-582 3	DARK	No name (src3)	Suzaku	2.4 ± 0.4	0.39	9^{+6}_{-5}	$1.9^{+0.5}_{-0.4}$	0.019	21	8, This work
HESS J1614-518	MSC	Suzaku J1614-5141 (srcA)	Suzaku	2.5 ± 0.2	1.8	12^{+5}_{-4}	1.7 ± 0.3	0.053	34	4, 19
HESS J1646-458	MSC	Suzaku J1648-4610 (srcA)	Suzaku	2.2 ± 0.1	2.7	34^{+24}_{-16}	$2.0^{+0.9}_{-0.7}$	0.019	142	9, This work
HESS J1848-018	MSC	$\cdots$	Chandra	2.8 ± 0.2	0.62	22 (fixed)	2.0 (fixed)	< 0.21	> 3.0	10, This work
MGRO J1908+06	UNID	$\cdots$	ASCA	2.1 ± 0.1	1.4	20 (fixed)	1.5 (fixed)	< 0.005	> 280	20, 23
TeV J2032+4130	UNID	Structure 1 (diffuse)	Suzaku	1.9 ± 0.1	0.26	6^{+4}_{-2}	$2.1^{+0.4}_{-0.3}$	0.021	12	21, 24
Westerlund 2	MSC	$\cdots$	Suzaku	2.5 ± 0.2	0.96	—	—	< 0.61 (0.7–10 keV)	> 2.7	22, 25

[1] MSC = Massive Star Cluster.
[2] Photon index of TeV spectra.
[3] Unabsorbed flux in the 1–10 TeV band (in 10^{-11} erg cm^{-2} s^{-1}).
[4] Column density for X-ray spectra (in 10^{21} cm^{-2}).
[5] Photon index of X-ray spectra.
[6] Unabsorbed flux in the 2–10 keV band (in 10^{-11} erg cm^{-2} s^{-1}).
[7] (1)H.E.S.S. Collaboration et al. (2012), (2)Aharonian et al. (2008a), (3)H.E.S.S. Collaboration et al. (2011a), (4)Aharonian et al. (2006a), (5)H.E.S.S. Collaboration et al. (2011b), (6)Tibolla et al. (2009), (7)Hoppe et al. (2008), (8)Renaud et al. (2008a), (9)Abramowski et al. (2012), (10)Chaves et al. (2008), (11)Fujinaga et al. (2010), (12)Eger et al. (2011), (13)Fujinaga et al. (2011), (14)Van Etten et al. (2009), (15)Matsumoto et al. (2009), (16)Bamba et al. (2007), (17)Misanovic et al. (2011), (18)Anada et al. (2009), (19)Matsumoto et al. (2008), (20)Aharonian et al. (2009), (21)Aharonian et al. (2005c), (22)Aharonian et al. (2007a), (23)Abdo et al. (2010), (24)Murakami et al. (2011), (25)Fujita et al. (2009)

5.9.2 Association of a possible counterpart with the unidentified VHE γ-ray sources

Although some X-ray sources are found in the vicinity of the unidentified VHE γ-ray sources, this does not necessarily mean that they are physically associated. From the results of HESS J1614−518 and HESS J1646−458 shown in Chapter 4, one of the key objects considering the association of the unidentified VHE γ-ray sources is extended X-ray emission and/or pulsar. Since we found such objects from the other two unidentified VHE γ-ray sources, we discuss their properties below.

HESS J1507−622

We found the possibly extended X-ray emission (Src2) located outside of the 3σ significance contour of HESS J1507−622. The X-ray spectrum implies emission from PWN, but there is no pulsar emission detected so far. On the other hand, if we assume the interstellar gas density of $n_{\rm H} = 1$ cm^{-3}, the distance to the source can be estimated to be 1 kpc. If that so, the offset is not so large compared to that of the identified PWNe which emit VHE γ rays (Hessels et al., 2008). Assuming a distance of 1 kpc, the luminosity of the source in the 2–10 keV band are 1.2×10^{32} erg s^{-1}. From this luminosity, if we assume the source is PWN, the spin-down luminosity of a pulsar $\dot{E} \sim 2 \times 10^{36}$ erg s^{-1} is expected (Mattana et al., 2009). Then, if the origin of the VHE γ-ray emission from HESS J1507−622 is this source, a reasonably efficiency of $\epsilon_\gamma = L_\gamma/\dot{E} = 0.04\%$ is required for the production of VHE γ-ray flux of HESS J1507−622, which is 1.5×10^{-12} cm^{-2} s^{-1} above 1 TeV (H.E.S.S. Collaboration et al., 2011a).

HESS J1857+026

We found the X-ray emission (Src1) at the position of PSR J1856+0245. PSR J1856+0245 has a spin period of 81 ms, a spin-down energy loss of 4.6×10^{36}erg s^{-1} and a characteristic age of 21000 yr (Hessels et al., 2008). The inferred γ-ray efficiency is $\epsilon_\gamma = L_\gamma/\dot{E} = 3.1\%$ (1–10 TeV, for a distance of 9 kpc), comparable to that observed in similar associations (Hessels et al., 2008). The X-ray spectrum of Src1 is similar to that of PWNe and their parent pulsars (Kargaltsev & Pavlov, 2008). Since the radial profile of Src1 supports the assumption of a point source, it is reasonable to interpret as the X-ray emission comes from the pulsar PSR J1856+0245. However, Src1 could be an X-ray PWN created by PSR J1856+0245. The luminosity of Src1 is $1.2\ d_9 \times 10^{33}$ erg s^{-1} in the 2–10 keV band, where d_9 is the distance scaled to 9 kpc. This is consistent with the X-ray luminosity of the associated PWN expected from the spin-down luminosity of the pulsar (Mattana et al., 2009). Since the size of the X-ray emission is almost consistent with the Suzaku PSF of $1'.8$, it is possible that the source is extended within this value. If we assume the size of the X-ray emission of $\sim 1'$, the physical size becomes ~ 3.3 pc, which is consistent with the expected value based on the PWN size-age relation (Bamba et al., 2010).

Above two unidentified VHE γ-ray sources could be linked to a PWN. However, it is clear that the extensions of the VHE γ-ray emission regions are larger than those of the X-ray emission regions. These differences can be explained by the difference of the cooling time of the electrons which emit VHE γ rays and X-rays. According to the quantitative evaluation in §2.3.4, if we assume the target photon as CMBR and the magnetic field of $B_{\rm ISM} \sim 3$ μG for synchrotron and IC processes, the typical lifetimes $\tau \sim 5$ kyr for the electrons with the energy of $E_e^{\rm sync} \sim 130$ TeV, and $\tau \sim 30$ kyr for the electrons with the energy of $E_e^{\rm IC} \sim 20$ TeV are obtained. This means that it is possible the extension of the VHE γ-ray emission could be larger than that of the X-ray emission by a factor of ~ 6 in this case.

5.9.3 Flux ratio of the VHE γ-ray and X-ray bands

Figure 5.26 shows VHE γ-ray fluxes vs. X-ray fluxes for the possible counterparts of the unidentified VHE γ-ray sources. We also plotted those for the PWNe detected by H.E.S.S. Here fluxes are absorption collected. The figure shows most of the possible counterparts of the unidentified VHE γ-ray sources are more luminous in VHE γ rays than in X-rays.

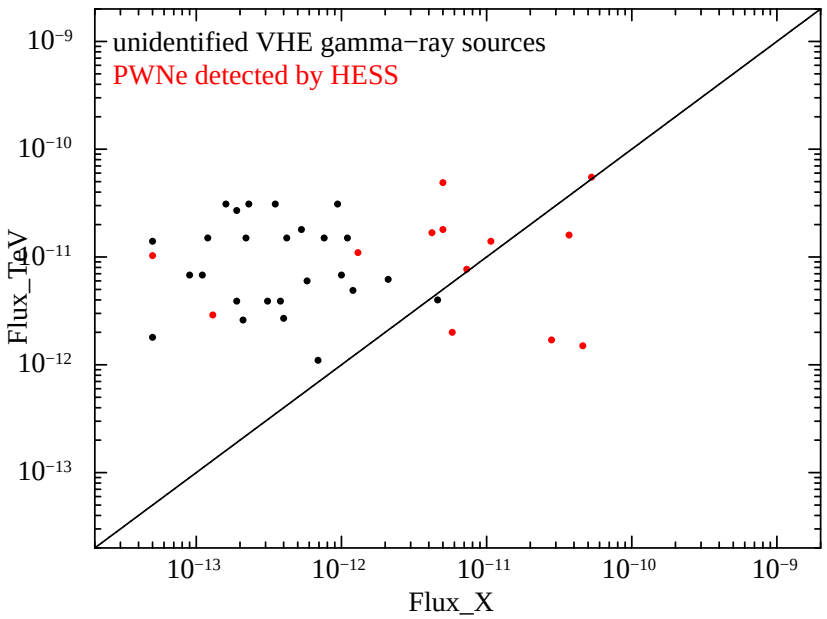

Figure 5.26: VHE γ-ray fluxes vs. X-ray fluxes for the possible counterparts of the unidentified VHE γ-ray sources (black) and the PWNe detected by H.E.S.S. (red).

We also evaluated the flux ratio $f_{\rm TeV}/f_{\rm X}$ in table 5.29. If we assumed that the VHE γ-ray emission is powered through 1-zone Inverse Compton (IC) scattering of the cosmic

microwave background off the accelerated electrons, and the electrons emit synchrotron radiation in the X-ray band, the typical energies E_γ and $E_{\rm X}$ of the IC and synchrotron photons produced by an electron are related as (see e.g. Aharonian et al., 1997)

$$E_\gamma \simeq 1.5(E_{\rm X}/0.1\ {\rm keV})(B/10\ \mu{\rm G})^{-1}\ {\rm TeV}, \tag{5.1}$$

where B is the magnetic field. The flux ratio of synchrotron flux ($f_{\rm sync}$) and inverse Compton flux ($f_{\rm IC}$) at these energies strongly depends on the magnetic field strength as (Aharonian & Atoyan, 1999)

$$\frac{f_{\rm (IC)}}{f_{\rm (sync)}} \simeq 0.1(B/10\ \mu{\rm G})^{-2}. \tag{5.2}$$

Thus, if we assume typical interstellar magnetic filed of a few microgauss, and the VHE γ rays are produced by electrons, the ratio becomes ~ 1. This means that electron accelerators should be bright in both X-rays and VHE γ rays. However, as can be seen in table 5.29 and figure 5.26, the unidentified VHE γ-ray sources have a flux ratio of larger than 1. This suggest that the magnetic fields in the unidentified VHE γ-ray sources are weaker than the typical interstellar magnetic field, or inverse Compton origin is unlikely. Thus, they are strong candidates for proton accelerators.

5.9.4 Photon indices in the VHE γ-ray and X-ray bands

Figure 5.27 (left) compares the distributions of the photon indices of the unidentified sources in the VHE γ-ray and X-ray bands. Mean photon index of the VHE γ-ray band is 2.53 with the standard deviation of 0.22, while that of the X-ray band is 1.51 with the standard deviation of 0.82. According to de Jager & Djannati-Ataï (2008), the required electron energy in a magnetic field of strength B, to radiate synchrotron photons of mean energy $E_{\rm keV}$ (in units of keV) is given by

$$E_e = (70\ {\rm TeV})(B/10\ \mu{\rm G})^{-1/2}E_{\rm keV}^{1/2}. \tag{5.3}$$

Similarly, the mean electron energy required to inverse Compton scatter the cosmic microwave background seed photons to energies $E_{\rm TeV}$ (in units of TeV) is typically lower at

$$E_e = (18\ {\rm TeV})E_{\rm TeV}^{1/2}. \tag{5.4}$$

Thus, electrons responsible for X-rays have larger energies than those for VHE γ rays. Here, the former has much shorter synchrotron life timescales than the latter (Mattana et al., 2009). Then, it is strange that the X-ray photon indices are harder than those of VHE γ ray. The harder spectrum in the X-ray band compared to the VHE γ-ray band do not allow the observed X-ray and VHE γ-ray spectra to be produced with synchrotron and inverse Compton emission, respectively, by a single power law distribution of electrons.

Figure 5.27 (right) compares the distributions of the X-ray photon indices of the unidentified VHE γ-ray sources and the PWNe detected by H.E.S.S. Mean X-ray photon

index of the unidentified VHE γ-ray sources is 1.51 with the standard deviation of 0.82, while that of the PWNe is 1.80 with the standard deviation of 0.32. The Kolmogorov-Smirnov (K-S) test shows the probability that the two samples are from the same photon index distribution is 0.60. There is no difference between the unidentified VHE γ-ray sources and the PWNe detected by H.E.S.S. with respect to a photon index.

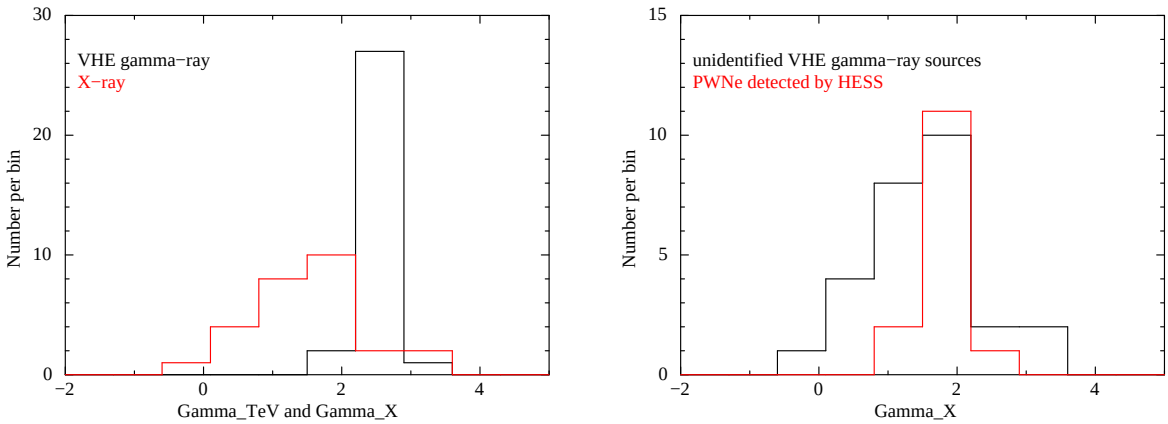

Figure 5.27: Left: Distribution of the photon indices of the unidentified VHE γ-ray sources in the VHE γ-ray (black) and X-ray (red) bands. Right: Distribution of the X-ray photon indices of the unidentified VHE γ-ray sources (black) and the PWNe detected by H.E.S.S. (red).

Chapter 6

Conclusions

In this thesis, we mainly analyzed X-ray data of the two unidentified VHE γ-ray sources, HESS J1614−518 and HESS J1646−458, in order to study the nature of unidentified VHE γ-ray sources. Our main results on the two unidentified VHE γ-ray sources are outlined below.

HESS J1614−518 We revealed that there was no evidence for the X-ray emission at the position of the 2nd brightest peak of the VHE γ-ray emission (Sakai et al., 2011). As a result, we confirmed the X-ray counterpart to the VHE γ-ray emission is just Suzaku J1614−5141 (Suzaku src A), which is the hard extended emission found at the position of the 1st brightest peak of the VHE γ-ray emission, as the best candidate for the X-ray counterpart of HESS J1614−518 (Matsumoto et al., 2008). Therefore, it was ensured that HESS J1614−518 has the high value of $f_{\rm TeV}/f_{\rm X} \sim 34$. This may suggest a proton accelerator. We also detected the soft X-ray source, XMMU J161406.0−515225, at the middle of HESS J1614−518 (Sakai et al., 2011). This source might be an AXP. If that so, HESS J1614−518 may be an SNR associated with an AXP. In that case, the Suzaku src A can be considered to be a shock region in the SNR. We then estimated an age of $\sim 10^5$ yr from the approximate radius of HESS J1614 ($r \sim 10' = 30$ pc @ 10 kpc). This means that HESS J1614−518 is an old SNR.

HESS J1646−458 We discovered the diffuse hard X-ray emission, Suzaku J1648−4610, around PSR J1648−4611 located within the emission region of HESS J1646−458 and associated with the Fermi-LAT source 2FGL J1648.4−4612. The spatial distribution and the photon index of the diffuse emission suggest a PWN. However, the luminosity of the diffuse emission is much larger than that expected from the spin-down luminosity of the pulsar. On the other hand, the spin-down luminosity would imply an unreasonably high efficiency for production of VHE γ-ray flux of HESS J1646−458. Thus, HESS J1646−458 seems unlikely to be explained only as a PWN powered by PSR J1648−4611. However, it is conceivable that parts of the VHE γ-ray emission of HESS J1646−458 could be caused by this peculiar PWN.

Additionally, through the study of the other 8 unidentified VHE γ-ray sources, we obtained following results.

- From the two unidentified VHE γ-ray sources, HESS J1507−622 and HESS J1857+026, we found possible X-ray counterparts in the hard-energy band.
- As for HESS J1507−622, we found the X-ray source located outside of the 3σ significance contour of HESS J1507−622 and is extended or unresolved multiple sources. The X-ray spectrum implies emission from PWN, but there is no pulsar emission detected so far. If we assume the interstellar gas density of $n_{\rm H} = 1$ cm^{-3}, the distance to the source can be estimated to be 1 kpc. If that so, the offset is not so large compared to that of the identified PWNe which emit VHE γ rays.
- As for HESS J1857+026, we found the X-ray emission at the position of PSR J1856+0245. The X-ray spectrum is similar to that of PWNe and their parent pulsars. Although the size of the X-ray emission is almost consistent with the Suzaku PSF of $1'.8$, this source could be an X-ray PWN created by PSR J1856+0245. In that case, it is conceivable that HESS J1857+026 is a possible PWN candidate powered by PSR J1856+0245.
- There is no strong conclusion that can be made, but these could be linked to a relatively old PWN still visible at VHE γ rays. Some of unidentified VHE γ-ray sources may be this kind of sources.
- For the other 6 unidentified VHE γ-ray sources, we were not able to obtain a conclusive result to identify the sources.

Through the study of the 10 unidentified VHE γ-ray sources, we revealed that some of unidentified VHE γ-ray sources may be peculiar SNRs or PWNe like HESS J1614−518 and HESS J1646−458. Whether still unidentified VHE γ-ray sources are also some type of these sources, more detailed multiwavelength observations are required. Such as more sensitive search for molecular cloud and non-detected energetic pulsar and/or PWN.

Bibliography

Abdo, A. A., et al. 2010, ApJ, 711, 64

Abramowski, A., et al. 2012, A&A, 537, A114

Aharonian, F. A., & Atoyan, A. M. 1996, A&A, 309, 917

Aharonian, F. A., Atoyan, A. M., & Kifune, T. 1997, MNRAS, 291, 162

Aharonian, F. A,, & Atoyan, A. M. 1999, A&A, 351, 330

Aharonian, F., et al. 2002, A&A, 393, L37

Aharonian, F., et al. 2004, Nature, 432, 75

Aharonian, F., et al. 2005a, Science, 307, 1938

Aharonian, F., et al. 2005b, A&A, 442, 1

Aharonian, F., et al. 2005c, A&A, 431, 197

Aharonian, F., et al. 2005d, A&A, 442, L25

Aharonian, F., et al. 2005e, A&A, 435, L17

Aharonian, F., et al. 2005f, A&A, 437, L7

Aharonian, F., et al. 2005g, Science, 309, 746

Aharonian, F., et al. 2006a, ApJ, 636, 777

Aharonian, F., et al. 2006b, ApJ, 460, 365

Aharonian, F., et al. 2006c, A&A, 449, 223

Aharonian, F., et al. 2006d, ApJ, 460, 743

Aharonian, F., et al. 2007a, ApJ, 467, 1075

Aharonian, F., et al. 2007b, ApJ, 661, 236

Aharonian, F., et al. 2007c, A&A, 464, 235

Aharonian, F., et al. 2008a, A&A, 490, 685

Aharonian, F., et al. 2008b, A&A, 477, 353

Aharonian, F., et al. 2009, A&A, 499, 723

Albacete Colombo, J. F., Flaccomio, E., Micela, G., Sciortino, S., & Damiani. F. 2007, A&A, 464, 211

Albert, J., et al. 2006a, ApJ, 643, L53

Albert, J., et al. 2006b, Science, 312, 1771

Albert, J., et al. 2007a, ApJ, 664, L87

Albert, J., et al. 2007b, ApJ, 665, L51

Anada, T., Ebisawa, K., Dotani, T., & Bamba, A. 2009, PASJ, 61, S183

Aschenbach, B., Citterio, O., Ellwood, J., Jensen, P., de Korte, P., Peacock, A., & Willingale, R. 1987, The High-Throughput Spectroscopic Mission, Report of the Telescope Working Group, Proc. ESA SP-1084

Bamba, A., et al. 2007, PASJ, 59, S209

Bamba, A., Anada, T., Dotani, T., Mori, K., Yamazaki, R., Ebisawa, K., & Vink, J. 2010, ApJL, 719, L116

Bautz, M. W., et al. 1998, Proc. SPIE, 3444, 210

Becker, W., & Trümper, J. 1997, A&A, 326, 682

Bell, A. R. 1978, MNRAS, 182, 147

Boldt, E. 1987, in IAU symp. 124, Observational Cosmology, ed. A. Hewitt, G. Burbidge, & L. Z. Fang (Dordrecht: Reidel), 611

Burke, B. E., et al. 1994, IEEE Trans., Nucl. Sci., 41, 375

Chaves, R. C. G., Renaud, M., Lemoine-Goumard, M., & Goret, P. 2008, AIP Conf. Series, 1085, 372

Chaves, R. C. G., for the H.E.S.S. Collaboration. 2009, astro-ph/0907.0768

Combi, J. A., Benaglia, P., Romero, G. E., & Sugizaki, M. 2005, A&A, 431, L9

Combi, J. A., Albacete Colombo, J. F., Romero, G. E., & Benaglia, P. 2006, ApJ, 653, L41

Cronin, J., Gaisser, T. K., & Swordy, S. P. 1997, Sci. Amer., 276, 44

de Jager, O. C., & Djannati-Ataï, A. 2008, astro-ph/0803.0116

den Herder, J. W., et al. 2001, A&A, 365, L7

Dickey, J. M., & Lockman, F. J. 1990, ARA&A, 28, 215

Dyer, K. K., Reynolds, S. P., & Borkowski, K. J. 2004, ApJ, 600, 752

Eger, P., Rowell, G., Kawamura, A., Fukui, Y., Rolland, L., & Stegmann, C. 2011, A&A, 526, A82

Fermi, E. 1949, Phys. Rev., 75, 1169

Fleishman, G. D., & Bietenholz, M. F. 2007, MNRAS, 376, 625

Freeman, P. E., Kashyap, V., Rosner, R., & Lamb, D. Q. 2002, ApJS, 138, 185

Fujinaga, T., et al. 2010, in Proceedings 25th Texas Symposium on Relativistic Astrophysics

Fujinaga, T., et al. 2011, PASJ, 63, S857

Fujita, Y., Hayashida, K., Takahashi, H., & Takahara, F. 2009, PASJ, 61, 1229

Fukazawa, Y., et al. 2009, PASJ, 61, S17

Funk, S., Hinton, J. A., Pühlhofer, G., Aharonian, F. A., Hofmann, W., Reimer, O., & Wagner, S. 2007, ApJ, 662, 517

Gallant, Y., et al. 2008, 40 Years of Pulsars: Millisecond Pulsars, Magnetars and More, 983, 195

Garmire, G. P., et al. 1992, in AIAA, Space Programs and Technologies Conference (Paper 9201473) (New York: AIAA)

Gondoin, P., et al. 1996, Proc. SPIE, 2808, 390

Gondoin, P., van Katwijk, K., Aschenbach, B., Schulz, N., Boerret, R., Glatzel, H., & Citterio, O. 1994, Proc. SPIE, 2209, 438

Gondoin, P., Aschenbach, B. R., Beijersbergen, M. W., Egger, R., Jansen, F. A., Stockman, Y., Tock, J. 1998a, Proc. SPIE, 3444, 278

Gondoin, P., Aschenbach, B. R., Beijersbergen, M. W., Egger, R., Jansen, F. A., Stockman, Y., Tock, J. 1998b, Proc. SPIE, 3444, 290

Gondoin, P., Aschenbach, B., Erd, C., Lumb, D. H., Majerowicz, S., Neumann, D., Sauvageot, J. L. 2000, Proc. SPIE, 4140, 1

Green, A. J., Cram, L. E., Large, M. I., & Ye, Taisheng 1999, ApJS, 122, 207

Halpern, J. P., & Gotthelf, E. V. 2010, ApJ, 710, 941

Harris, D. E., Silverman, J. D., Hasinger, G., & Lehmann, I. 1998, A&AS, 133, 431

H.E.S.S. Collaboration., et al. 2011a, A&A, 525, A45

H.E.S.S. Collaboration., et al. 2011b, A&A, 531, A81

H.E.S.S. Collaboration., et al. 2012, astro-ph/1203.3215

Hessels, J. W. T., et al. 2008, A&A, 682, L41

Higashi, Y., et al. 2008, ApJ, 683, 957

Hoppe, S., for the H.E.S.S. Collaboration. 2008, Proc. 30th Int. Cosmic Ray Conf., 2, 579

Horns, D., Hoffmann, A. I. D., Santangelo, A., Aharonian, F. A., & Rowell, G. P. 2007, A&A, 469, L17

Ishisaki, Y., et al. 2007, PASJ, 59, S113

Jansen, F., et al. 2001, A&A, 365, L1

Jones, F. C. 1968, Phys. Rev., 167, 1159

Kang, J. -H., & Koo, B. -C. 2007, ApJS, 173, 85

Kargaltsev, O., Pavlov, G. G., & Garmire, G. P. 2007, ApJ, 660, 1413

Kargaltsev, O., & Pavlov, G. G. 2008, astro-ph/0801.2602

Kargaltsev, O., Pavlov, G. G., & Wong, J. A. 2009, ApJ, 690, 891

Kargaltsev, O., Durant, M., Pavlov, G. G., & Garmire, G. 2012, ApJS, 201, 37

Kawabata, K., Nobukawa, M., Tsuru, T. G., & Koyama, K. 2012, PASJ, 64, 99

Kokubun, M., et al. 2007, PASJ, 59, S53

Koyama, K., et al. 2007, PASJ, 59, S23

Koyama, K., Petre, R., Gotthelf, E. V., Hwang, U., Matsuura, M., Ozaki, M., & Holt, S. S. 1995, Nature, 378, 255

Kramer, M., et al. 2003, MNRAS, 342, 1299

Manchester, R. N., & Taylor, J. H. 1977, *Pulsars.* San Francisco: Freeman

Manchester, R. N., Hobbs, G. B., Teoh, A., & Hobbs, M. 2005, AJ, 129, 1993

Mason, K. O., et al. 2001, A&A, 365, L36

Matsumoto, H., et al. 2007, PASJ, 59, S199

Matsumoto, H., et al. 2008, PASJ, 60, S163

Matsumoto, H., Uchiyama, H., Tsuru, T. G., Koyama, K., & Tibolla, O. 2009, in Proc. The Energetic Cosmos: from Suzaaku to Astro-H, 154

Mattana, F., et al. 2009, ApJ, 694, 12

Mereghetti, S. 2008, A&A Rev., 15, 225

Mewe, R., Gronenschild, E. H. B. M., & van den Oord, G. H. J. 1985, A&AS, 62, 197

Misanovic, Z., Kargaltsev, O., & Pavlov, G. G. 2011, ApJ, 735, 33

Mitsuda, K., et al. 2007, PASJ, 59, 1

Mizukami, T., et al. 2011, ApJ, 740, 78

Morrison, R., & McCammon, D. 1983, ApJ, 270, 119

Murakami, H., Kitamoto, S., Kawachi, A., & Nakamori, T. 2011, PASJ, 63, S873

Nakamura, R., Bamba, A., & Ishida, M. 2009, PASJ, 61, S197

Nolan, P. L., et al. 2012, ApJS, 199, 31

Padmanabhan, P. 2001, Theoretical astrophysics. Vol. II: Stars and Stellar Systems. Cambridge University Press, Cambridge, MA

Piatti, A. E., Claria, J. J., & Bica, E. 2000, A&A, 360, 529

Renaud, M., Goret, P., & Chaves, R. C. G. 2008a, AIP Conf. Series, 1085, 281

Renaud, M., Hoppe, S., Komin, N., Moulin, E., Marandon, V., & Clapson, A. -C. 2008b, AIP Conf. Series, 1085, 285

Revnivtsev, M., Tuerler, M., Del Santo, M., Westergaard, N. J., Gehrels, N., & Winkler, C. 2003, IAU Circ., 8097, 2

Rowell, G., Horns, D., Fukui, Y., & Moriguchi, Y. 2008, AIP Conf. Series, 1085, 241

Rybicki, G. B., & Lightman, A. P. 2004, Radiative Processes in Astrophysics (Weinheim: WILEY-VCH Verlag GmbH & Co. KGaA), ch. 6

Sakai, M., Yajima, Y., & Matsumoto, H. 2011, PASJ, 63, S879

Sato, T., Bamba, A., Nakamura, R., & Ishida, M. 2010, PASJ, 62, L33

Serlemitsos, P. J., et al. 2007, PASJ, 59, S9

Smith, R. K., Brickhouse, N. S., Liedahl, D. A., & Raymond, J. C. 2001, ApJ, 556, L91

Strüder, L., et al. 2001, A&A, 365, L18

Sugizaki, M., Mitsuda, K., Kaneda, H., Matsuzaki, K., Yamauchi, S., & Koyama, K. 2001, ApJS, 134, 77

Takahashi, T., et al. 2007, PASJ, 59, S35

Tawa, N., et al. 2008, PASJ, 60, S11

Taylor, J. H., & Cordes, J. M. 1993, ApJ, 411, 674

Tibolla, O., Chaves, R. C. G., de Jager, O., Domainko, W., Fiasson, A., Komin, N,, Kosack, K. 2009, astro-ph/0907.0574

Tomsick, J. A., Lingenfelter, R., Walter, R., Rodriguez, J., Goldwurm, A., Corbel, S., & Kaaret, P. 2003, IAU Circ., 8076, 1

Turner, M. J. L., et al. 2001, A&A, 365, L27

Uchiyama, H., Matsumoto, H., Tsuru, T. T., Koyama, K., & Bamba, A. 2009a, PASJ, 61, S189

Uchiyama, H., et al. 2009b, PASJ, 61, S9

Van Etten, A., Funk, S., & Hinton, J. 2009, ApJ, 707, 1717

Voges, W., et al. 2000, IAU Circ., 7432, 1

Weisskopf, M. C., Brinkman, B., Canizares, C., Garmire, G., Murray, S., & Van Speybroeck, L. P. 2002, PASP, 114, 1

Westerlund, B. 1961, AJ, 66, 57

Whiteoak, J. B. Z., & Green, A. J. 1996, A&AS, 118, 329

Yamashita, A., et al. 1997, IEEE Trans., Nucl. Sci., 44, 847

Yamazaki, R., Kohri, K., Bamba, A., Yoshida, T., Tsuribe, T., & Takahara, F. 2006, MNRAS, 371, 1975

Zwiebel, E., & Heiles, C. 1997, Nature, 385, 131

Acknowledgments

I would like to express my gratitude to Associate Professor Hironori Matsumoto in Nagoya University, who gave me a first motivation to study unidentified VHE γ-ray sources. He gave me a lot of advice and comments and taught me how to analyze the data. I was relieved by his encouragement many times. I could not have finished my thesis without his great assist and encouragement. I am deeply grateful to Professor Hideyo Kunieda in Nagoya University, who lead me to a graduate school. I learned an attitude toward study and had a fruitful five years at Nagoya University. I would like to thank Associate Professor Yoshito Haba in Nagoya University, who was collaborator of this thesis, for discussing the interpretation of the results. I would like to thank Dr. Hideyuki Mori in ISAS/JAXA. He also gave me a lot of advice and comments and taught me how to analyze the data concretely.

I wish to thank all the members of astrophysical group in Nagoya University, especially those of X-ray astrophysical group. I had a wonderful time as a graduate student with them for five years. I do hope that an X-ray astrophysics will continue to be successful in the future. Finally, I would like to thank my family for their supports, encouragements, and understandings.